

University of Kentucky

UKnowledge

Theses and Dissertations--Chemistry

Chemistry


2023

Exploring the Role of Ring Annulation in Polycyclic Aromatic Hydrocarbons for Organic Electronic Applications

Tanner Smith

University of Kentucky, tanlsmith53@gmail.com

Author ORCID Identifier:

 <https://orcid.org/0009-0005-9410-2765>

Digital Object Identifier: <https://doi.org/10.13023/etd.2023.418>

[Right click to open a feedback form in a new tab to let us know how this document benefits you.](#)

Recommended Citation

Smith, Tanner, "Exploring the Role of Ring Annulation in Polycyclic Aromatic Hydrocarbons for Organic Electronic Applications" (2023). *Theses and Dissertations--Chemistry*. 182.
https://uknowledge.uky.edu/chemistry_etds/182

This Doctoral Dissertation is brought to you for free and open access by the Chemistry at UKnowledge. It has been accepted for inclusion in Theses and Dissertations--Chemistry by an authorized administrator of UKnowledge. For more information, please contact UKnowledge@lsv.uky.edu.

STUDENT AGREEMENT:

I represent that my thesis or dissertation and abstract are my original work. Proper attribution has been given to all outside sources. I understand that I am solely responsible for obtaining any needed copyright permissions. I have obtained needed written permission statement(s) from the owner(s) of each third-party copyrighted matter to be included in my work, allowing electronic distribution (if such use is not permitted by the fair use doctrine) which will be submitted to UKnowledge as Additional File.

I hereby grant to The University of Kentucky and its agents the irrevocable, non-exclusive, and royalty-free license to archive and make accessible my work in whole or in part in all forms of media, now or hereafter known. I agree that the document mentioned above may be made available immediately for worldwide access unless an embargo applies.

I retain all other ownership rights to the copyright of my work. I also retain the right to use in future works (such as articles or books) all or part of my work. I understand that I am free to register the copyright to my work.

REVIEW, APPROVAL AND ACCEPTANCE

The document mentioned above has been reviewed and accepted by the student's advisor, on behalf of the advisory committee, and by the Director of Graduate Studies (DGS), on behalf of the program; we verify that this is the final, approved version of the student's thesis including all changes required by the advisory committee. The undersigned agree to abide by the statements above.

Tanner Smith, Student

Dr. John E. Anthony, Major Professor

Dr. Kenneth Graham, Director of Graduate Studies

EXPLORING THE ROLE OF RING ANNULATION IN POLYCYCLIC AROMATIC
HYDROCARBONS FOR ORGANIC ELECTRONIC APPLICATIONS

DISSERTATION

A dissertation submitted in partial fulfillment of the
requirements for the degree of Doctor of Philosophy in the
College of Arts and Sciences
at the University of Kentucky

By
Tanner Lanier Smith
Lexington, Kentucky
Director: Dr. John E. Anthony, Professor of Chemistry
Lexington, Kentucky
2023

Copyright © Tanner Lanier Smith 2023
<https://orcid.org/0009-0005-9410-2765>

ABSTRACT OF DISSERTATION

EXPLORING THE ROLE OF RING-ANNULATION IN POLYCYCLIC AROMATIC HYDROCARBONS FOR ORGANIC ELECTRONIC APPLICATIONS

Organic materials offer promising potential for the next generation of electronic devices, as their tunability, processability, and low-temperature manufacturing make them a cheap and versatile alternative to traditional silicon-based electronics. The ability to systematically alter the electronic properties of organic materials is vital for their incorporation into device applications. Polycyclic aromatic hydrocarbons (PAHs) are of significant interest for organic electronic applications, as relevant properties are highly dependent on their size, structure, and functionalities, and thus can be tuned to fit a wide variety of applications. Due to the enormous number of structural isomers available in larger PAHs, the development of design protocols is necessary to efficiently develop high-performing materials. Linear extension of the aromatic core, such as that seen in the acene series, is an efficient yet underexplored method for tuning the electronic properties of larger PAHs.

The role of ring annulation is explored in Chapter 2 and Chapter 3, which will detail the synthesis and properties of PAHs of similar size but significantly different electronic structures. The role of linear ring extension in 2-D PAHs is also explored, demonstrating that the electronic structure of larger PAHs can be systematically tuned with significant implications for their applications and stability. The role of ring annulation is explored further in Chapter 4, in which a similar class of materials to that explored in Chapter 3 is examined to further elucidate how subtle changes in the PAH backbone can impact electronic properties. Chapter 5 details the tuning of a series of dyes through functionalization, with the goal of altering their optical properties for implementation into radiation sensors. The development of novel synthetic procedures is described, which allows for systematic tuning of electronic properties in each class of aromatic compounds.

KEYWORDS: Organic electronics, synthesis, acenes, nanographenes

Tanner Lanier Smith

7/31/2023

EXPLORING THE ROLE OF RING-ANNULATION IN POLYCYCLIC AROMATIC
HYDROCARBONS FOR ORGANIC ELECTRONIC APPLICATIONS

By
Tanner Lanier Smith

Dr. John E. Anthony

Director of Dissertation

Dr. Kenneth Graham

Director of Graduate Studies

07/31/2023

Date

ACKNOWLEDGEMENTS

The journey to this point in my academic and professional career would not have been possible without the countless people who have helped and supported me along the way. I am eternally grateful for the love and support of my parents and family, who have supported me every step of the way through my academic journey. I would not be where I am today without them. Prof. John Anthony has been a great advisor and mentor, and has been instrumental in my development as a scientist. Profs. Chad Risko, Ken Graham, and Matthew Beck have been extremely helpful as members of my committee, and have provided me thought-provoking feedback that has greatly helped in my graduate work. I am greatly appreciative of the work of collaborators, including Liang-chun Lin and advisors Prof. Niels Damrauer (University of Colorado) and Dr. Justin Johnson (National Renewable Energy Laboratory), as well as Dr. Alex Ai (University of Kentucky). Prof. Sean Parkin solved a number of crystal structures that were greatly beneficial to my graduate work. Dr. Karl Thorley provided important theoretical calculations for my work, and has been a valuable source of guidance over the years. I would also like to thank group members past and present, including Dr. Emma Holland, Garrett Fregoso, Dean Windemuller, Barron Cox, Eve Aldridge, and Andrew Sturgis, for their help and friendship over the years.

TABLE OF CONTENTS

ACKNOWLEDGEMENTS.....	iii
TABLE OF CONTENTS	iv
LIST OF TABLES	vi
LIST OF FIGURES	vii
Chapter 1: Introduction	1
1.1: Preface	1
1.2: Organic Field-Effect Transistors: Device Structure and Charge Transport	2
1.3: Introduction to Nanographenes.....	4
1.4: Solid-state Ordering in Organic Semiconductors	7
1.5: Disorder in Organic Semiconductors	8
1.6: Photophysical Processes and Introduction to Singlet Fission	10
1.7: Acenes for Singlet Fission	13
1.8: Stability of Acenes and Nanographenes	16
1.9: Introduction to Radiochromic Leuco Dyes	18
1.10: Summary	21
Chapter 2: Synthesis and Photophysical Applications of Vertical Pyrenes.....	23
2.1: Introduction to Vertical Pyrenes	23
2.2: Synthesis of TIPS-APA and TIPS-AP	25
2.3: Vertical Pyrene Properties	27
2.4: Vertical Pyrenes for Photophysical Studies	29
2.5: Synthesis of Vertical Pyrenes for Photophysical Applications.....	30
2.6: NODIPS-TPT: Photophysical Properties and SF	33
2.7: Vertical Pyrene Conclusions	35
2.8: Experimental.....	35
Chapter 3: Synthesis and Properties of Extended Acenoacenes	53
3.1: Introduction to Oblique Pyrenes.....	53
3.2: Synthesis of Oblique Pyrenes.....	54
3.3: Properties of Acenoacenes.....	57
3.4: Stability in Acenoacenes.....	61
3.5: Tuning Solid-State Packing Through Alkylsilylethyne Substituents ..	65

3.6: The Role of Bisacene Functionalization in Preventing Dynamic Disorder	66
3.7: Summary	66
3.8: Experimental	67
Chapter 4: Towards a Functionalized, Stable Cata-Pentacenopentacene	79
4.1: Introduction to Cata-annulated Acenoacenes	79
4.2: Synthesis of TIPS-c-PP	80
4.3: Absorption Properties and Stability of TIPS-c-PP	83
4.4: Crystal Packing in TIPS-c-PP	84
4.5: Conclusion	85
4.6: Experimental	85
Chapter 5: Functionalized Leuco Dyes for Radiochromic Dosimeters.....	90
5.1: Introduction to Triphenylmethane dyes for Radiochromic Dosimeters	90
5.2: Synthesis of Leuco Dyes	92
5.3: Incorporation of Leuco Dyes into Polymer Composites	95
5.4: Conclusion	98
5.5: Experimental	99
Chapter 6: Summary	106
Appendix	110
References	112
Vita	123

LIST OF TABLES

Table 3.1: Calculated S_1 and T_1 energies for acenoacenes and **TIPS-Pen**. 64

LIST OF FIGURES

Figure 1:1: Device structure of a bottom-contact OFET.	3
Figure 1:2: Nanographenes of varying size and number of Clar sextets (red), including (a) acenes, (b) acenoacenes, and (c) pyrene-fused acenes.	6
Figure 1:3: Examples of (a) herringbone, (b) 2-D brickwork, and (c) 1-D slipstack packing motifs.....	8
Figure 1:4: Long-axis displacements in a TIPS-Pentacene dimeric pair.....	9
Figure 1:5: Scenarios in the absorption of a photon by a Si solar cell in which (a) the photon has less energy than E_g , (b) the photon has exactly the energy of E_g , and (c) the photon is greater in energy than E_g	11
Figure 1:6: Jablonski diagram featuring photophysical processes such as a) absorbance, b) vibrational relaxation, c) fluorescence, d) internal conversion, e) intersystem crossing, and f) phosphorescence.....	12
Figure 1:7: Energy level diagram of the SF process.....	12
Figure 1:8: Examples of a) functionalized acenes and b) acene dimers that have demonstrated SF.....	14
Figure 1:9: Two decomposition pathways commonly observed in acenes.	16
Figure 1:10: Energy level diagram of Type I and Type II photodecomposition pathways.	17
Figure 1:11: a) pentacene and b) an example of a “bispentacene.”	18
Figure 1:12: The colorless (leuco), radical, and colored forms of malachite green.	20
Figure 2:1: a) K-region and non-K-region positions of pyrene and b) vertical pyrene vs. oblique pyrene.	24
Figure 2:2: Synthetic route to TIPS-APA.	26
Figure 2:3: Synthetic route to AP derivatives.....	27
Figure 2:4: a) Extinction coefficient and b) CV spectra for TIPS-AP and TIPS-APA.	28
Figure 2:5: a) FMO and b) NICS scans for TIPS-AP and TIPS-APA.....	29
Figure 2:6: Synthetic routes to NODIPS-TPT and NODIPS-TP.....	31
Figure 2:7: Synthetic routes to TNPS-PE-APA and TNPS-PE-AP.....	32
Figure 2:8: UV-Vis absorbance spectrum of vertical pyrenes.....	33
Figure 2:9: a) Extinction coefficient and b) CV spectra for NODIPS-TP and NODIPS-TPT.....	34
Figure 3:1: 2-D acenoacenes of varying size and annulation mode.	54
Figure 3:2: Synthetic route to acenoacene quinones.....	55
Figure 3:3: Synthesis of NODIPS-BP and NODIPS-BH.	56

Figure 3:4: Attempted synthesis of NODIPS-BHep.	57
Figure 3:5: UV-Vis absorption spectrum of NODIPS-BP and NODIPS-BH as a function of (a) wavelength and b) eV.	58
Figure 3:6: Frontier molecular orbitals of acenoacenes.	58
Figure 3:7: CV spectra of (a) NODIPS-BP and (b) NODIPS-BH.	59
Figure 3:8: Stability studies displaying the max onset absorbance as a function of time under white light exposure.	60
Figure 3:9: (a) absorbance and PL spectra for TNPS-BH and (b) absorbance spectra of TNPS-BH (blue) and decomposed TNPS-BH.	61
Figure 3:10: (a) Activation energy for the reaction of acenoacenes and TIPS-Pentacene with $^1\text{O}_2$ on each ring, (b) Reaction energies for acenoacenes with $^1\text{O}_2$ to form the endoperoxide on each ring.	62
Figure 3:11: UV-Vis spectra of (a) NODIPS-BP and (B) NODIPS-BH under exposure to ambient laboratory light over 1 month, as well as energy levels of EPO products.	63
Figure 3:12: NICS values for bispentacene and bishexacene. Error! Bookmark not defined.	
Figure 3:13: Crystal packing structures of a) NODIPS-BP, b) NODIPS-BH, and c) TNPS-BH.	66
Figure 4:1: Cata-annulated (a) TIPS-substituted N-PP, (b) non-functionalized PP, and (c) TIPS-substituted PP.	80
Figure 4:2: Synthetic route to TIPS-c-PP.	81
Figure 4:3: ^1H NMR spectrum of TIPS-c-PP.	82
Figure 4:4: (a) UV-Vis spectrum of TIPS-c-PP, NODIPS-BP, and TIPS-Pen, (b) stability studies for TIPS-c-PP and NODIPS-BP in chloroform under white light exposure.	83
Figure 4:5: Crystal structure of TIPS-c-PP.	85
Figure 5:1: Proposed diagram of a TATTOO dosimeter. ¹	91
Figure 5:2: Examples of DMA-substituted dyes with various functionalities synthesized in this project.	93
Figure 5:3: Color change of Leuco dyes dissolved in DCM under ambient laboratory conditions.	94
Figure 5:4: UV-Vis spectra for DMA-substituted dyes in chloroform.	95
Figure 5:5: Examples of (a) activators and (b) polymers and resins used in the formulations of composites.	96
Figure 5:6: (a) DMA-TM-LD in epoxy with TCE as activator, (b) DMA-PM-LD in epoxy resin with diiodomethane activator, (c) DMA-PM-LD in PDMS with CCl_4 activator.	97

Figure 5:7: (a) structures of dyes with extended alkyl chains, (b) Free-standing epoxy composites utilizing DEA-TM-LD. 98

Chapter 1: Introduction

1.1: Preface

The accelerating demand for consumer electronics requires innovation not only in traditional devices, but new types of materials that can meet the need for an increased variety of applications. Inorganic semiconductors, such as silicon, have traditionally been considered the backbone of modern electronics.¹ However, crystalline silicon requires intensive, high-temperature manufacturing processes that ultimately diminish the cost-efficiency of device production.² Organic electronic materials are a versatile alternative to their silicon-based counterparts. While they cannot match the performance of crystalline silicon, organic semiconductors (OSC) offer the advantage of low-temperature manufacturing processes and scalable on-demand printing.³ The shape adaptability and interface softness displayed by organic electronics are ideal for use in advanced healthcare, bioelectronics, and the Internet-of-Things (IoT).^{4,5} Additionally, organic and inorganic materials may be used in tandem to further optimize electronic properties and provide rather unique device architectures.⁶ The goal of organic electronics research is not to replace crystalline silicon, but to supplement existing silicon-based technologies by enabling applications inaccessible to rigid electronics.⁷ For these reasons, the market share for organic/printed electronics is projected to more than double over the next decade.³

The efficiency of organic electronic devices has improved dramatically over the last three decades, and benchmark OSC materials are now capable of outperforming amorphous silicon.⁸ This can generally be attributed to better understanding of materials design as well as improvements in device fabrication. Many of the parameters that govern OSC performance can be altered at the molecular level, giving researchers remarkable control over materials design.⁹ Properties, such as solubility in organic solvents, the color of light emission, and solid-state ordering can be finely tuned via chemical synthesis.¹⁰ The versatile

chemical modifications offered by organic compounds gives rise to a seemingly infinite number of molecular building blocks. Therefore, the development of molecular design principles that can allow for more efficient materials development is critical. Tunability is an important aspect of organic electronics, and thus the design of organic building blocks whose properties can be systematically altered via straightforward chemical modification are desirable. Commercially viable materials and devices should not only perform well in laboratory environments, but also display long-term stability under standard operating conditions. The design of materials that fit all these criteria will require multidisciplinary collaboration amongst synthetic chemists, device physicists and engineers, and computational scientists. The following sections will provide a brief introduction into the devices, applications, and materials relevant to the materials discussed in this dissertation.

1.2: Organic Field-Effect Transistors: Device Structure and Charge Transport

Many of the materials in this dissertation are ultimately designed for transistor applications, and thus a brief overview of the working principles of such devices is necessary. The organic field-effect transistor (OFET) is the most common device for studying the charge transport abilities of OSCs. A typical OFET is composed of a gate electrode, a gate dielectric layer, an OSC, and source–drain electrodes. Two common device configurations are top contact, when the source and drain electrodes are evaporated on the top of the organic material, and bottom contact, when they are evaporated on the dielectric before depositing the organic semiconductor.¹¹ Bottom contact configurations allow for quick examination of new semiconductor materials, while top contact configurations can help reduce environmental degradation of the organic material. The device is turned on when an applied gate-source voltage (V_{GS}) polarizes the dielectric causing the accumulation of charge carriers at the semiconductor-dielectric interface, while an applied source-drain voltage (V_{DS}) forces charge carriers from the source to the drain electrode.⁷ A small V_{GS} , known as a threshold voltage (V_{Th}) is typically required to first fill charge traps at

the semiconductor-dielectric interface before free charge carriers can flow.⁷ The primary figure of merit is the field effect mobility (μ), which has units of $\text{cm}^2 \text{V}^{-1} \text{s}^{-1}$, and corresponds to the velocity of the charge carriers against the electric field.¹²

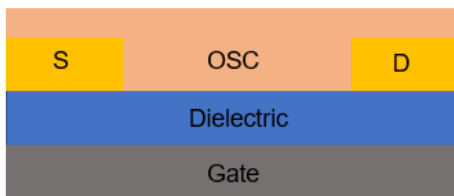


Figure 1:1: Device structure of a bottom-contact OFET.

In contrast to inorganic semiconductors, in which the crystal acts as a single molecule, OSCs are typically composed of individual molecules. Therefore, the arrangement of the molecules in the solid-state is critical to its charge transport properties. The electronic structure of the molecules, the relative positions of the molecules in the solid-state, and the morphology variations generated from static or dynamic disorder are all factors that will influence molecular packing.¹³ Charge transport at room temperature typically operates by a thermally activated hopping mechanism.¹⁴ The primary factors which govern charge transport are incorporated into the Marcus equation:^{15,16}

$$k_{ET} = \frac{4\pi^2}{h} \frac{1}{\sqrt{4\pi k_B T}} t^2 e^{\frac{-\lambda}{4\lambda RT}}$$

where k_{ET} is the rate of electron transfer, T is the temperature, λ is the reorganization energy, t is the transfer integral, G° is the Gibbs free energy, and h and k_B are the Planck and Boltzmann constants. Generally, the reorganization energy should be small, and the transfer integral should be large in order to achieve high charge mobilities. The transfer integral is defined as the splitting of the frontier molecular orbital between adjacent molecules,¹³ and is highly dependent on the molecular packing. This is because the electronic coupling is dependent on the intermolecular overlap of the frontier molecular orbitals

(FMOs), which decrease with increasing distance between molecules.¹² It is important to note that electronic coupling is dependent not just on spatial overlap between molecular orbitals, but on wavefunction overlap. Thus, small displacements can result in large changes in transfer integrals and significantly impact charge transport.

OSCs can transport electrons (n-type transport) or holes (p-type) depending on the accumulation of charges when a gate voltage (positive or negative) is applied.¹⁷ While most OSCs are inherently ambipolar, i.e. capable of both p-type and n-type transport, in practice the alignment of the FMOs of organic molecules with the work function of the electrode determines whether the transistor operates as p-type, n-type, or ambipolar.⁷ P-type involves the injection of holes into the highest occupied molecular orbital (HOMO) of the semiconductor, and is most commonly observed because the HOMO level of many OSCs aligns well with the work function of gold (4.8-5.1 eV).¹⁸ N-type transport occurs via electron injection into the lowest unoccupied molecular orbital (LUMO) of the molecules. Optimizing organic materials for n-type transport typically requires careful molecular design in order to lower the LUMO to align with the work function of environmentally stable electrodes such as gold, which typically requires electron affinity (EA) > 3 eV.¹⁸ Thus, the ability to systematically tune FMOs of organic materials is crucial to their implementation in transistors.

1.3: Introduction to Nanographenes

Many organic electronic materials belong to the class of organic molecules known as polycyclic aromatic hydrocarbons (PAHs), which are compounds with two or more fused benzene rings. One of the most fundamental PAH derivatives is graphene, which can be thought of as an indefinitely extended 2-D network of fused benzene rings. While graphene displays remarkably high charge mobilities, its lack of bandgap hinders its straightforward application into transistors, which require controllable device turn-off. A bandgap can be introduced into graphene through the fabrication of smaller graphene segments, i.e. nanographenes,

whose properties are determined by their size and edge configuration.¹⁹ While “top-down” methods, such as hydrothermal or lithographic “cutting” of graphene, offer poor control over size and structure, “bottom-up” chemical synthesis allows for precise control over nanographene structure and electronic properties.^{19,20} The structural diversity in PAHs is enormous, and the possible number of PAH structures accelerates rapidly with each additional fused ring. For example, PAHs containing 10 fused rings can potentially form over 16,000 structural isomers by changing only the mode of ring annulation.²¹ The investigation of all possible PAH structures through trial and error alone is not feasible, and therefore improvements in both molecular design and chemical synthesis are required in order to take full advantage of the electronic and structural potential available in nanographenes.

For several decades, Clar’s sextet theory has been widely used as a model to describe the reactivity of polycyclic compounds. Clar’s model essentially states that the Kekule’ resonance structure with the largest number of aromatic sextets most accurately describes the properties of PAHs.²² In general, a PAH with a given number of aromatic π -sextets is kinetically more stable than its isomers with less aromatic π -sextets.^{23,24} This has generally been corroborated through experimental studies, as systematically increasing the number of sextets in structural isomers increases the HOMO-LUMO gap as well as absorption energy.²⁵ The aromatic character of specific rings with a PAH structure can be estimated experimentally through analysis of C-C bond lengths measured by X-ray crystallography, and typically correspond well with the structure predicted by the Clar model.²⁶ A number of aromatic indices, such as those incorporating Nucleus Independent Chemical Shifts (NICS), have also corroborated Clar’s theory in a number of PAH systems.^{27,28} However, the qualitative nature of the Clar model limits its ability to accurately predict certain properties, such as stability, in a number of systems.

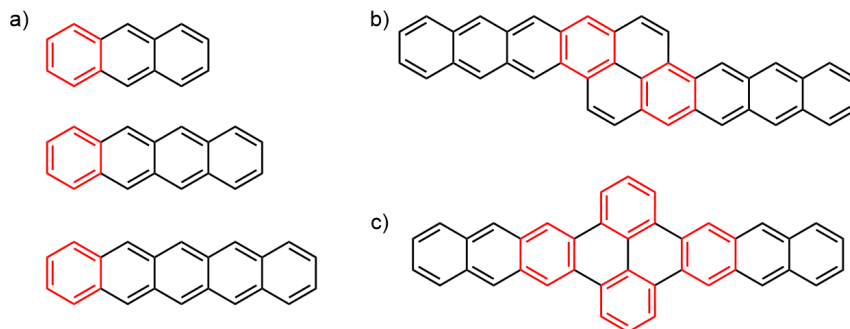


Figure 1:2: Nanographenes of varying size and number of Clar sextets (red), including (a) acenes, (b) acenoacenes, and (c) pyrene-fused acenes.

Acenes are the only class of PAHs that feature one aromatic sextet regardless of length, and as such display rapid acceleration of electronic properties and chemical reactivity with each additional fused ring.²⁹ Acenes show decreasing HOMO-LUMO gaps with increasing length of the acene, i.e. going from anthracene to tetracene to pentacene, allowing for facile control over electronic structure.³⁰ The FMOs of acenes can also be easily tuned through functionalization, providing further control over electronic structure, carrier type, and stability.³¹ Reorganization energies also decrease with increasing size of the acene, which has been suggested to explain high charge carrier mobilities in the longer acenes³² – although this phenomenon could also be explained through improved overlap in these larger π -systems. Unfortunately, acenes become increasingly prone to decomposition with each linearly fused ring, and derivatives longer than pentacene are typically too unstable for implementation into device applications. Acene stability will be explored in more detail in chapter 1.8.

Because of the efficient tuning available in acene derivatives, the incorporation of acene moieties into larger nanographene molecules has become an increasingly popular method to tune their properties.^{33,34,35} The fusion of linear acenes into 2-D “acenoacenes” results in nanographenes with unique electronic properties. While not considered traditional acenes due to the presence of multiple Clar sextets, these fully conjugated molecules show acene-like absorption and redox properties that can be readily tuned in a manner similar to their 1-D counterparts.³⁴ The fusion of acenes onto other polycyclic aromatic

moieties, such as pyrene or corannulene, is another method to tune the properties of nanographenes. The nature of ring annulation in such systems can alter the number Clar sextets and subsequently impact the structure of the FMOs, resulting in nanographenes with rather unique electronic properties. The impact of ring annulation on the electronic structures of acene-fused nanographenes will be an important theme throughout this dissertation.

1.4: Solid-state Ordering in Organic Semiconductors

Because of the importance of intermolecular interactions in the performance of OSC materials, a brief overview of the kinds of solid-state ordering is necessary. Three common types of packing that are commonly encountered in OSC materials include herringbone, 1-D slipped stacking, and 2-D brickwork packing (Figure 1.3). Herringbone motifs are typically dominated by C-H- π interactions, which are essentially a weak form of hydrogen bonding where the C-H moiety is directed towards the phenyl ring of adjacent molecules.³⁶ An example of a high performance material with herringbone packing is C8-BTBT, which features reported mobilities $>15 \text{ cm}^2\text{V}^{-1}\text{s}^{-1}$ depending on fabrication conditions.^{8,37} Both 1-D and 2-D packing structures feature extensive π - π interactions, often termed “ π -stacking”, which generally refers to attractions/repulsions between the faces of aromatic compounds. Molecules that display 2-D brickwork packing motifs are likely to have large, multi-directional transfer integrals that are conducive to 2-D charge transport. TIPS-Pentacene is perhaps the most well-known OSC that displays 2-D brickwork packing, with optimized thin-films displaying charge mobilities as high as $12 \text{ cm}^2 \text{V}^{-1}\text{s}^{-1}$.³⁸ 1-D slipped stacked motifs often display 1-D charge transport, and thus mobilities in these materials are often lower than their 2-D counterparts.

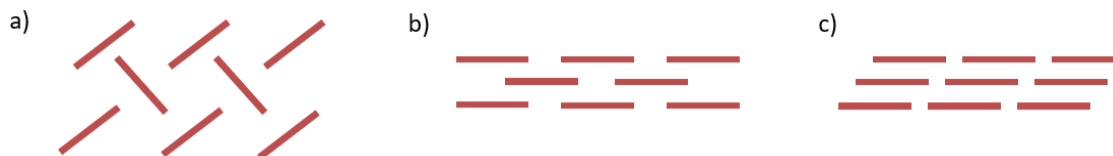


Figure 1:3: Examples of (a) herringbone, (b) 2-D brickwork, and (c) 1-D slipstack packing motifs.

Tuning solid-state ordering through molecular design requires an understanding of the intermolecular forces that drive certain packing motifs. Exchange interactions act as the main repulsive force between compounds, which physically limits molecular proximity so that electrons avoid significant overlap.³⁹ The primary attractive force that can counteract the exchange energy is dispersion forces, which results from instantaneous changes in electron density.³⁹ A common method to control the crystal packing of organic semiconductors is by functionalizing the aromatic backbone with trialkylsilyl (TAS) ethynyl groups. The introduction of bulky alkylated substituents enhances the dispersion force that work to balance out the exchange interactions and can improve π -stacking.³⁹ This is borne out in the case of TIPS-Pentacene, in which the addition of the addition of triisopropylsilylethyne (TIPS) groups to the pentacene backbone changes the packing structure from herringbone to 2-D brickwork, resulting in significantly enhanced π -stacking.⁴⁰ The substituents on the silane can be altered in order to tune crystal packing, however, the nature of the size and structure of TAS groups required to induce π -stacking interactions differs depending on the size of the system. Additionally, the incorporation of longer alkyl chains onto the silane is an efficient method to improve solubility of a PAH in common organic solvents.

1.5: Disorder in Organic Semiconductors

The capability of charge carriers to form delocalized electronic states is crucial to achieving organic semiconductors with high carrier mobilities $>10 \text{ cm}^2 \text{ V}^{-1} \text{ s}^{-1}$.^{41,42} In addition to large transfer integrals, charge delocalization is favored by small electron-phonon coupling and the absence of energetic disorder.⁴¹

Static disorder consists of crystal defects or chemical impurities, which results in deep trap states that can be detrimental to charge transport. The impact of static disorder can be minimized through device optimization, which has been achieved to a large extent in the highest mobility systems.⁴¹ A greater hinderance to charge transport is dynamic disorder, which refers to fluctuations in the transfer integrals caused by thermally induced molecular vibrations in the molecular lattice. Due to the relatively weak van der Waals interactions in organic semiconductors, the phonon modes in molecular crystals often exhibit large vibration amplitudes on the order of 0.1 Å, which ultimately limits the ability of charge carriers to form fully delocalized electronic states.^{42,43} A number of high-performance organic semiconductors have been reported to exhibit band-like temperature dependent mobility near room temperature, with increased temperature resulting in decreased carrier mobility.^{41,43} This would strongly suggest that mitigating dynamic disorder could result in significant gains in semiconductor performance for a number of materials.

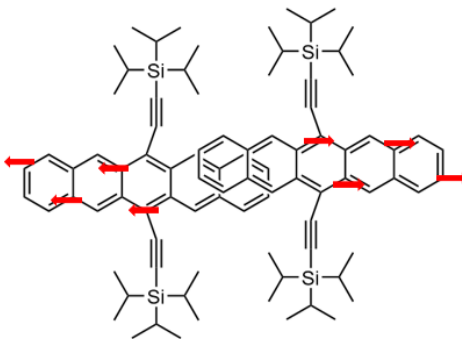


Figure 1:4: Long-axis displacements in a TIPS-Pentacene dimeric pair.

The most common source of dynamic disorder in oligoacenes is considered to be low-frequency, large amplitude vibrations along the long-axis of the molecule.^{41,42} Generally speaking, large-amplitude thermal vibrations can be reduced by increasing the force constant between molecules.⁴⁴ Minimizing these vibrations through functionalization of high-performance OSC materials has been of growing interest. The electron-phonon coupling, or the sensitivity of transfer

integrals to slight intermolecular shifts, is also a critical aspect in mitigating dynamic disorder. Rubrene is perhaps the best example of a high-performing OSC that displays minimal dynamic disorder, with mobilities $>10 \text{ cm}^2 \text{ V}^{-1} \text{ s}^{-1}$.⁴⁵ In addition to large transfer integrals, rubrene displays exceptionally weak electron-phonon coupling.⁴⁵ Furthermore, the phenyl rings orthogonal to the backbone work to inhibit the long-axis sliding motion.⁴² Based on these observations, it is likely that future OSC materials that display a combination of large transfer integrals, weak electron-phonon coupling, and suppressed molecular vibration are more likely to display exceptional charge transport properties.

1.6: Photophysical Processes and Introduction to Singlet Fission

The current market for photovoltaic (PV) devices is dominated by silicon-based cells. In these types of cells, absorption of a photon promotes an electron from the valence band (VB) of silicon to the conduction band (CB) and, in the presence of an electric field, produces a photocurrent.⁴⁶ The best single-junction silicon-based PV devices made in the laboratory have PCEs of $\sim 27\%$, with commercially available modules not far behind.⁴⁷ However, these devices are quickly approaching the theoretical efficiency limit, as single-junction solar cells suffer from fundamental loss mechanisms that prevent them from converting all incident radiation into power. Photons with energy less than the bandgap (E_g) of the semiconductor will not be absorbed and will thus not generate an electron-hole pair (figure 1.5a). Photons with energy equal to E_g will be absorbed (1.5b), while those with energy greater than E_g will be absorbed, but any energy in excess of E_g will be lost via thermalization (1.5c).⁴⁸ This latter process is the main contributor to the so-called Shockley–Queisser limit on efficiency, which is $\sim 30\%$ for an ideal single-junction silicon cell.⁴⁷ While multi-junction PVs are capable of overcoming this limit, with reported efficiencies greater than 45% , the cost and complexity of these devices has limited their widespread use.⁴⁸

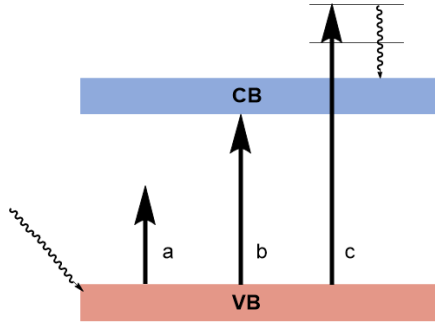


Figure 1:5: Scenarios in the absorption of a photon by a Si solar cell in which (a) the photon has less energy than E_g , (b) the photon has exactly the energy of E_g , and (c) the photon is greater in energy than E_g .

Singlet Fission (SF) is a carrier multiplication process that holds great potential to improve the efficiency of single junction solar cells. The SF process can ultimately produce two triplet excitons (T_1) for each singlet (S_1) generated by absorption of a photon by the chromophore. The overall SF process can be described by the equation:



Photophysical processes relevant to the SF process can be seen in Figure 1.6. In the first step of SF, a molecule in its electronic ground state (S_0) absorbs a photon of sufficient energy to undergo a $S_1 \leftarrow S_0$ transition (Figure 1.6a). If the energy of the photon is in excess of S_1 , vibrational relaxation to S_1 will occur (Figure 1.6b), at which point the molecule can either undergo fluorescence back to S_0 (1.6c), or form a triplet state (T_1). The $T_1 \leftarrow S_1$ transition is an example of intersystem crossing (1.6e), and is typically slow and unfavorable as the transition requires a change in spin. In the case of SF however, the molecule in its S_1 state can then interact with a nearby molecule in its S_0 state to form a correlated triplet pair (1TT), which can then decouple into two separate T_1 states.⁴⁹ Because the two triplets that comprise 1TT are coupled as an overall singlet, SF is considered to be a spin allowed process and can proceed on ultrafast time scales.⁴⁹

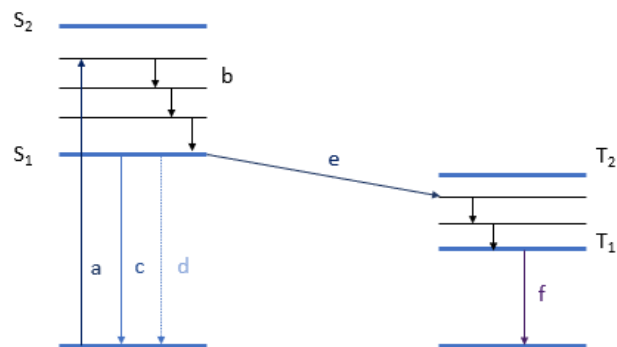


Figure 1:6: Jablonski diagram featuring photophysical processes such as a) absorbance, b) vibrational relaxation, c) fluorescence, d) internal conversion, e) intersystem crossing, and f) phosphorescence.

The speed and efficiency of the SF process is also largely dependent on the energy levels of the chromophore, particularly S_1 and T_1 . For SF to proceed efficiently, the process should be either exothermic or only slightly endothermic (Figure 1.7). Exothermic SF occurs when $ES_1 > 2ET_1$, and proceeds rapidly since the reaction is both energetically and entropically favorable.⁵⁰ In the reverse case, when $ES_1 < 2ET_1$, endothermic SF can occur if ES_1 is within 200-300 meV of $2ET_1$. Endothermic SF may still proceed efficiently, albeit more slowly, due to the inherent entropy gain in generating two triplet excitons from one singlet exciton. SF must also outcompete deactivation pathways such as triplet-triplet annihilation (TTA), in which two T_1 states combine to form a higher triplet excited state such as T_2 . This can be prevented if the chromophore meets the energetic requirement $ET_2 > 2ET_1$.⁴⁹

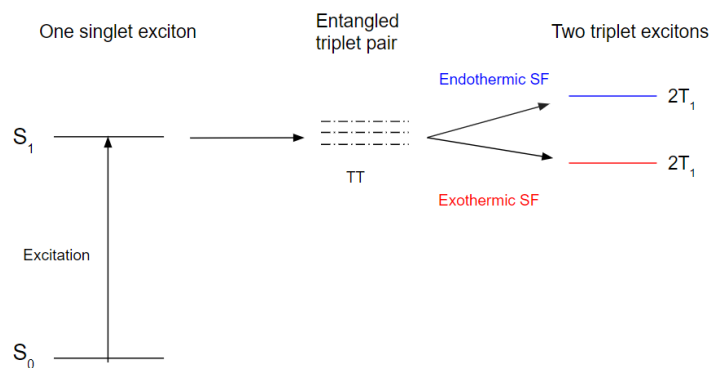


Figure 1:7: Energy level diagram of the SF process.

The triplet excitons produced by SF have roughly half the energy of the initial singlet. As such, a PV module with only a SF material will produce double the photocurrent but also cut the voltage by half, leading to no net benefit in the power conversion efficiency.⁵¹ In order to boost the PCE, the SF material must be paired with a low-gap semiconductor (LGS) such as silicon. The LGS absorbs low-energy photons and sets the V_{oc} , while the SF material produces two excitons per absorbed photon, enabling twice the photocurrent to be generated and an overall increase in PCE.⁴⁸ The triplet level of the SF material must roughly match the bandgap of the LGS ($E_g = 1.1\text{eV}$ for silicon) in order for triplet transfer to be efficient.⁴⁸ SF materials should also display long triplet lifetimes, high absorption coefficients, and long term stability in order for their incorporation into cost efficient devices.⁴⁸

A less explored application for SF involves the design of molecular spin qubits for quantum information science (QIS). The ^5TT state, which can be generated via SF, is useful in quantum technologies as its four entangled spins can be initialized into a pure, well-defined quantum state.^{52,53,54} While the role of ^5TT has been studied as a SF intermediate in a number of systems,^{55,56,57} reports of the selective generation of ^5TT as the main product of the SF process are sparse. Theoretical work has suggested that ^5TT can be selectively populated through careful control of chromophore orientation. The JDE model proposes that ^5TT can be selectively generated from ^1TT if the SF chromophores 1) share common molecular axis, 2) display large chromophore exchange energies (J), 3) are spatially ordered, and 4) are dilute.⁵³ The design of systems that meet all of these requirements is still a major challenge.

1.7: Acenes for Singlet Fission

A number of chromophores have been shown to perform SF, including acenes, rylenes, carotenoids, diketopyrrolopyrroles, and benzofurans.^{50,49} Acenes are perhaps the most heavily studied SF materials, and will be the focus

of this section as they are the most relevant. As closed-shell alternant hydrocarbons, the S_1 - T_1 gap in acenes is equal to twice the transfer integral and does not change much with system size.⁵⁸ Because the exchange integral is large in acenes, the energetic requirement $ES_1 > 2ET_1$ can be met by increasing the length of the acene, which in turn decreases S_1 and T_1 . Thus, SF occurs exothermically in pentacene and is slightly endothermic in tetracene. Functionalized pentacenes and tetracenes in particular have been of significant research interest. The benchmark SF compound TIPS-Pentacene undergoes near-quantitative SF (triplet yield $\approx 200\%$) both in solution and in the solid-state.^{59,60} TIPS-tetracene also shows efficient SF in solution as well as in thin-films,^{61,62} and has also been used in the synthesis of quantum dot systems with triplet yields approaching unity.⁶³ It is important to note that intermolecular SF in the solid-state is highly morphology dependent, as polymorphism in pentacenes and tetracenes has been shown to significantly affect the rate and yield of triplet formation. Anthracenes, and their silylethyne-substituted derivatives, are not known to undergo SF efficiently due to the large endothermicity of the process in these systems. However, SF in thin-films of bisphenylethyne anthracenes (BPEAs) proceeds in high yields, as the phenylethyne substituents perturb the S_1 and T_1 levels so that SF is nearly isoergic in the solid-state.^{64,65} The triplet yields in BPEA are highly polymorph-dependent, and tuning the solid-state ordering through functionalization can drastically alter the SF rate and yield.^{65,66}

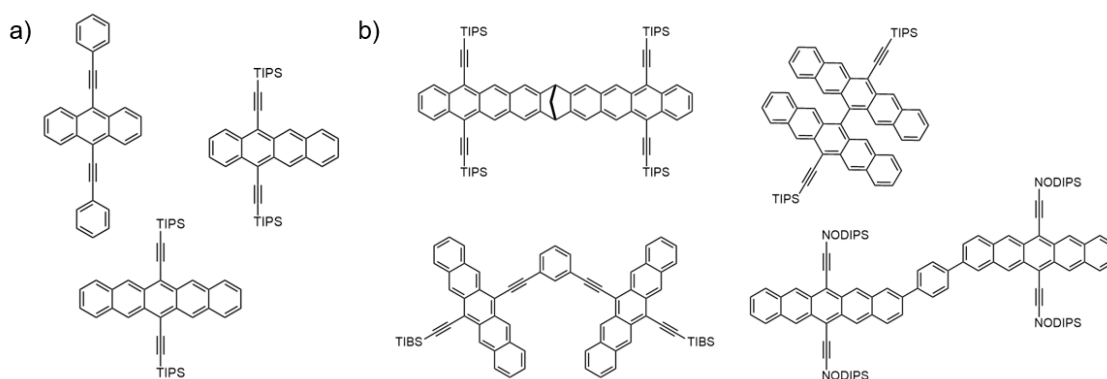


Figure 1:8: Examples of a) functionalized acenes and b) acene dimers that have demonstrated SF.

The morphology dependence can complicate the study of many aspects of the SF process, as it may not be immediately obvious which chromophore pair or pairs are most conducive for SF. Additionally, poor intermolecular interactions may inhibit the process in chromophores that are otherwise prime SF candidates. These issues may at least be partly circumvented through the study of covalently bonded dimers, in which the SF dynamics may be altered by tuning the through-bond interactions between chromophores. This is commonly done by changing the linker connecting the two chromophores, altering the degree of electronic coupling and thus the efficiency of SF. There have been many reported examples of conjugated, homoconjugated, and nonconjugated pentacene and tetracene dimers,^{67,68} with the degree of through-bond and through-space interactions critical to the SF process.⁶⁹ If the goal is to maximize the production of non-correlated T_1 states through SF, then the electronic coupling should be just strong enough to facilitate efficient formation of 1TT yet weak enough to allow for decoherence of 1TT into $T_1 + T_1$.⁶⁹

The presence of rotatable bonds between chromophores can complicate the SF picture in such dimers, as rotation of the chromophores can alter the electronic coupling and thus cause variations in SF dynamics. This issue can be overcome through the study of rigid dimers, which feature linkers that prevent rotation and thus provide certainty in the position of the chromophores. While less common than rotatable dimers, a number of structurally rigid acene dimers have been investigated.^{70,71,72} Many of these dimers show efficient SF despite containing linkers that limit or break conjugation between chromophores, and in some cases display slower triplet recombination compared to similar conjugated dimers.⁷¹ As discussed in Section 1.6, the JDE model proposes that rigid, planar molecular dimers are optimal for the selective production of higher spin-polarized quantum states such as 5TT through SF.⁷³ While no dimers that simultaneously meet all of the requirements laid out in the JDE model are believed to have been reported, the study of rigid dimers in which the chromophores share a molecular axis prove that 5TT can be selectively populated through SF.⁷⁴

1.8: Stability of Acenes and Nanographenes

As noted in Section 1.3, the rapid evolution of electronic properties in the acene series also leads to increased chemical reactivity with increasing length, resulting in poor stability of the larger acenes. In the context of Clar's theory, the presence of only one stabilizing aromatic sextet spread across an increasing number of rings means a greater tendency for larger acenes to break into two separate acenes, each with their own sextet. Decomposition of acenes generally occurs either through reaction with molecular oxygen to generate an endoperoxide, or through dimerization with another acene (Figure 1.9). Non-substituted acenes larger than pentacene are difficult to synthesize due to their poor stability, and generally cannot be isolated under ambient conditions.⁷⁵ The stability of acenes can be enhanced through functionalization, which can slow the rate of photooxidation by perturbing their FMOs and block dimerization through steric effects.²⁹ In this manner, heavily functionalized acenes as large as nonacene (9 rings) can be characterized under ambient conditions.²⁹

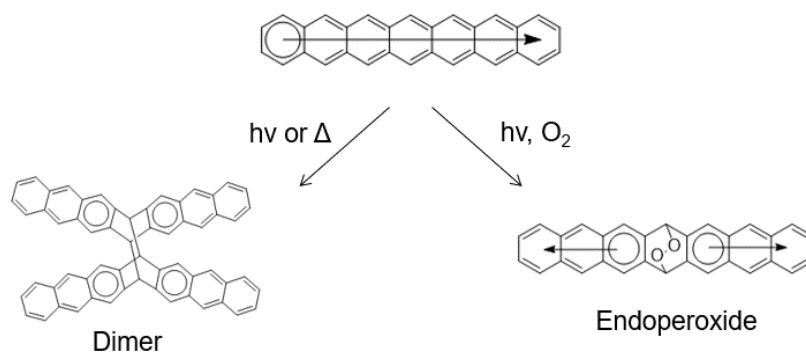


Figure 1:9: Two decomposition pathways commonly observed in acenes.

While Clar's theory provides a simple, qualitative description for the stability of PAHs, the role of aromatic stability can be misleading. The structure of linear acenes allows for the position of the sextet on any one of the rings, which gives rise to the 'migrating' sextet, in which the aromatic contribution should be equally weighted across each ring in the molecule.⁷⁶ However, NICS calculations show that aromaticity increases from the outer to inner rings in acenes, and that the aromaticity of the center ring actually grows stronger with increasing length of

the acene.⁷⁷ This appears counterintuitive to the numerous experimental observations that show the center rings to be the most reactive in the longer acenes.^{29,78} Calculations show that the stabilization energy actually remains essentially the same with increasing length of the acene, and that the reactivity of the center ring corresponds to smaller activation barriers to electrocyclic reactions.⁷⁷ This can be attributed in part to similar increases in the HOMO coefficients from the outer to the inner rings, which are consistent with the preferential reactivity of the middle rings.^{79,80,81} Thus, the reaction pathways of possible decomposition reactions must be carefully considered when addressing the stability of PAH derivatives.

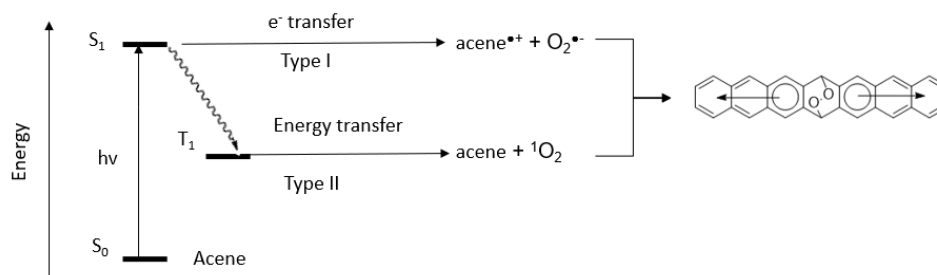


Figure 1:10: Energy level diagram of Type I and Type II photodecomposition pathways.

Two photooxidation pathways are typically operative in acene derivatives (Figure 1.10). In an electron transfer mechanism (type I), an acene is excited by light and subsequently transfers an electron to molecular oxygen to form a radical $\cdot\text{O}_2$ anion and an acene radical cation. These two species may then react to form the endoperoxide. If the T_1 level of the acene is greater than the S_1 - T_1 gap in triplet oxygen ($^3\text{O}_2$), then photodecomposition may occur via an energy transfer mechanism (type II). In this case, an acene in its S_1 excited state forms its T_1 state, which then transfers energy to $^3\text{O}_2$ to form singlet oxygen ($^1\text{O}_2$), which can then react to form the endoperoxide. Acenes functionalized with silylethyne substituents are more resistant to photooxidation than their unsubstituted counterparts. This has been attributed to lowering of the LUMO and T_1 energy levels of the acene, which slows photooxidation via type I and type II pathways, respectively.^{82,83} The addition of O_2 is also directed towards the ring containing

the alkyne substituents, which promotes reconversion of the endoperoxide back to the parent acenes, thus slowing the rate of decomposition.⁸⁴

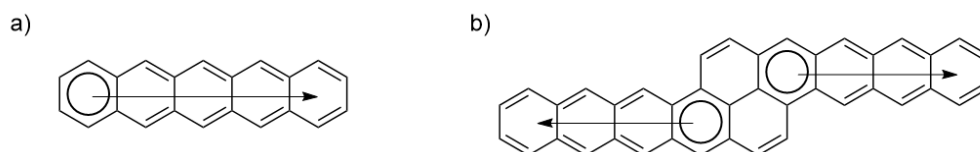


Figure 1:11: a) pentacene and b) an example of a “bispentacene.”

Perhaps the most interesting characteristic of acenoacenes is their remarkable stability, with substituted bistetracenes and bispentacenes (eight and ten consecutively fused rings, respectively) showing considerably enhanced photostability compared to TIPS-pentacene.^{85,86,87} While this enhanced stability may intuitively be attributed to the presence of an additional aromatic sextet, this again has proven to be an oversimplification. Bredas and coworkers found that the remarkable stability of a silylethyne-substituted bistetracene was actually linked to a large distortion energy which resulted in a higher free energy barrier to oxidation.⁸⁸ The abnormally large distortion energy compared to linear acenes was the result of switching from a 1-D to a 2-D aromatic framework. It was also found that photooxidation primarily occurs via a type II mechanism, in which a bistetracene in its excited T_1 state reacts with 3O_2 to generate 1O_2 , which then reacts with the bistetracene to form the endoperoxide.⁸⁸ This underscores the importance of lowering the triplet level of the PAH to less than that of the singlet-triplet gap of O_2 to minimize the generation of 1O_2 and ultimately improve stabilities. It is worth noting that functionalized acenoacenes longer than bispentacene have not yet been reported, and thus it is not clear how these molecular design guidelines would impact the stability of the larger derivatives.

1.9: Introduction to Radiochromic Leuco Dyes

Radiochromic dosimeters have been of research interest since the 1960s, and have shown great potential for use in a number of radiation-based applications such as medical dosimetry.⁸⁹ These dosimeters offer advantages

over traditional radiographic dosimeters in that they color directly upon exposure to radiation without the need for chemical processing, allowing for quick and simple interpretation.⁹⁰ The qualitative changes in color can also be measured quantitatively through changes in optical density (ΔOD). When radiochromic leuco dyes are exposed to radiation, a chemical change occurs which results in conversion from the colorless (leuco) form to the colored form. In the case of triphenylmethane leuco dyes, abstraction of the functional group from the central carbon yields the cation form of the dye, often through a radical intermediate, and the resulting color change in the material.⁹¹ Because of their known ability to undergo reversible photochromism, malachite green derivatives have been heavily studied as potential radiation sensors over the past several decades. McLaughlin and coworkers performed several studies on the incorporation of triphenylmethane dyes into plastic-based radiochromic dosimeters, and found that the sensitivity and accuracy of such devices depends on factors such as the nature of the dye, host material, and film composition and thickness.^{92,93,94} Such studies underscored the importance of optimizing all aspects of the dosimeter in order to achieve ideal sensitivity for a desired application.

Leuco-Malachite Green (LMG), which features hydrogen on the central carbon, has received increased attention as a potential active component in dosimeters. One reason for this is its cheap and straightforward synthesis. LMG can be prepared in a one-step condensation reaction between N,N-dimethylaniline, benzaldehyde, and an acid catalyst. A number of derivatives can be prepared in this manner simply by changing the N,N-alkyl substituents or by the addition of functional groups to benzaldehyde. The color change mechanism in LMG-based dyes involves homolytic bond cleavage of the central hydrogen, which can be catalyzed by a radical initiator such as a halogen.⁹⁵ The addition of electron-donating or electron-withdrawing functional groups has been shown to alter the reactivity of the dyes. However, the exact manner in which these substituents impact reactivity is still unclear, as only a few functionalized LMG derivatives have been studied. The addition of electron-donating methoxy substituents increases the reactivity of the dyes relative to non-functionalized

LMG, while substitution of halogens onto LMG results in even faster activation compared to dyes featuring methoxy groups.^{95,96} While the substituted halogens may participate in the homolytic bond cleavage of the central C-H bond, radiation of these dyes without an added activator did not result in activation, suggesting that aryl-substituted halogens do not take direct part in the activation process.⁹⁵ It is clear that a more diverse set of functionalized LMG dyes are needed in order to better understand the impact of substitution on their optical properties.

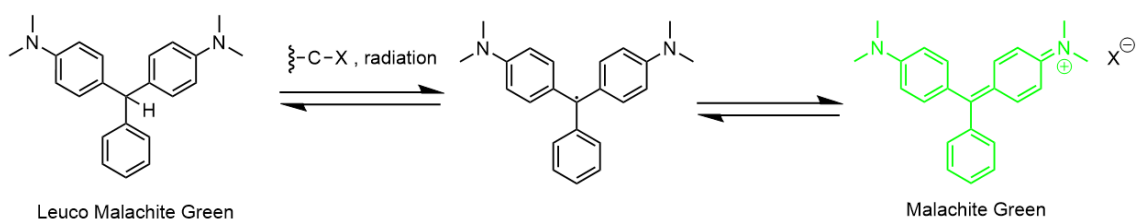


Figure 1:12: The colorless (leuco), radical, and colored forms of malachite green.

While earlier radiochromic films utilized triphenylmethane leucocyanides, more recent films, such as the GAFCHROMIC MD-55-2 make use of polydiacetylene as the active component due to its range of sensitivity (3-100 Gy).⁸⁹ The advent of Presage dosimeters, which primarily utilize LMG as the active component, has generated significant research interest in the use of LMG in radiochromic applications.⁹⁷ These dosimeters consist of a leuco dye (LMG) and a radical initiator, typically a halocarbon, enclosed within a polymer composite such as polyurethane. Upon radiation exposure, radiolysis of the halocarbon initiator results in the abstraction of hydrogen from the central carbon via homolytic bond cleavage. The radical dye may then convert to the MG cation, resulting in color change (Figure 1.12).⁹⁵ Dosimeters with this structure typically show linear optical responses as a function of applied radiation, and sensitivity can be tuned by changing functionalities on the dye,⁹⁵ initiator,⁹⁸ composite thickness,⁹⁹ and wt% of the components.⁹⁶ Additionally, such dosimeters may be robust and flexible,⁹⁶ improving the diversity of potential applications outside of clinical use.

1.10: Summary

Organic electronic materials offer a versatile alternative to traditional silicon-based devices, as their structure and properties can be tuned through organic synthesis to fit a wide variety of applications. The molecular structure of aromatic compounds determines a number of important parameters relevant to their implementation into electronic devices, such as energy levels, solid-state morphology, and processability. The charge transport characteristics of OSCs depend largely on their solid-state ordering, and thus the ability to optimize packing and minimize disorder are crucial to their implementation into devices. The unique optical properties of the acene series make them prime candidates for SF, displaying potential in applications such as photovoltaics and QIS. The instability in the larger acenes can be addressed by their incorporation into 2-D polyaromatic frameworks, whose electronic properties can be tuned in a similar manner to the linear acenes while displaying enhanced photooxidative resistance. Because improvements in molecular design cannot be accomplished without a solid understanding of their applications, this introduction aims to provide relevant context to the studies that will be discussed throughout this dissertation.

The following chapters detail the application-guided design and synthesis of different classes of aromatic compounds, with each study meant to improve upon one or multiple aspects of materials design. The synthetic protocols should not only allow for access to the compounds in question but should also be as efficient and scalable as possible. Efficient synthesis is ultimately necessary for materials to be commercially viable, as simple and cheap manufacturing conditions are vital for the success of organic electronics. Additionally, such protocols will ideally allow for straightforward alteration of molecular size and functionalities in order to systematically investigate structure-function relationships. Tunability is a key aspect of organic electronics and will thus be a common theme in the following chapters.

Due to the enormous degree of structural diversity available in PAHs, studies that systematically explore how the mode of ring annulation impacts the

properties of PAHs are invaluable in the design of organic electronics for specific applications. The first example of such a study is presented in chapter 2, which details the synthesis, photophysical properties, and applications of a series of pyrene-fused acenes. Chapter 3 discusses the synthesis of 2-D acenoacenes as well as their unique electronic properties, and continued efforts to optimize this class of materials for transistor applications. The comparison between this series of acenoacenes and the pyrene-fused acenes in Chapter 2 provides an interesting perspective on how the mode of ring annulation in large polycyclic aromatic systems impacts electronic properties. The role of ring annulation is explored further in chapter 4, which describes the synthetic route to extended 1,2-fused pentacenopentacene, an example of an acenoacene whose mode of ring-fusion differs from the similar systems described in chapter 3. Chapter 5 describes the design of a radiochromic dosimeter consisting of functionalized triphenylmethane leuco dyes incorporated into polymer composites. While these leuco dyes differ from the materials discussed in previous chapters in that they are not 2-D acene derivatives, chapter 5 firmly fits within the theme of this dissertation in that the optical properties of these polycyclic aromatic dyes can be tuned through functionalization. Additionally, the work presented in chapter 5 exemplifies another important theme, which is that the molecular properties of the active material must be optimized alongside the other components of a device to maximize performance.

Chapter 2: Synthesis and Photophysical Applications of Vertical Pyrenes

2.1: Introduction to Vertical Pyrenes

Vertical pyrene-fused acenes (vertical pyrenes), consist of acene moieties fused at the K-region of pyrene. Several examples of such pyrene-fused acenes and azaacenes have been reported in the literature,^{100,33} including extended nanoribbons with dozens of repeating pyrene-azaacene units. These studies have drawn into question the nature of the pyrene-acene interactions, as experimental data appears to suggest that such systems are not fully conjugated. For example, reports of extended pyrene-azaacene systems show that the optical and electrochemical gaps do not shift with the further addition of pyrene-azaacene units.^{101,102} While computational studies on these systems are more rare, a study published by the Risko group found that the orientation of a central pyrene “delimiter” alters the degree of communication between two acene units.¹⁰³ In the case of “vertical” pyrenes, which feature acene-like segments fused to the K-region of pyrene, the electronic communication between the two acenes is expected to be disrupted by the central delimiter. In contrast, “oblique” pyrenes were suggested to maintain full conjugation throughout the molecule. It is worth noting that DFT calculations carried out on some extended vertical pyrene systems appear to show frontier molecular orbitals that extend across large portions of the system and appear to change with molecular length.¹⁰¹ However, more detailed calculations are needed to reconcile this apparent delocalization with the experimental results as well as Risko’s report of broken conjugation.

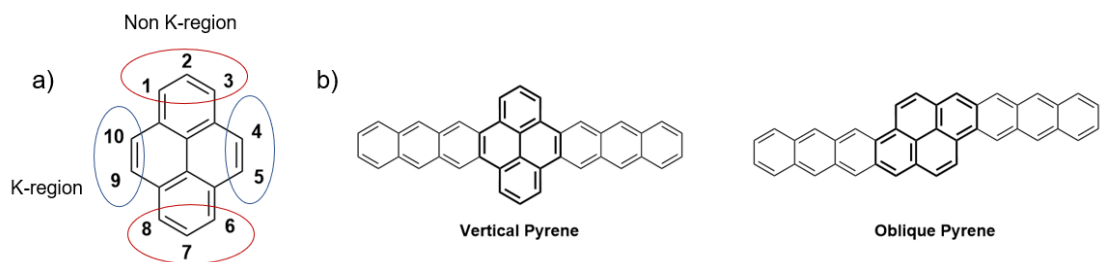


Figure 2:1: a) K-region and non-K-region positions of pyrene and b) vertical pyrene vs. oblique pyrene.

Despite the evidence for broken conjugation in vertical pyrenes, an in-depth study on the nature of the pyrene-acene interactions had not been reported until recently.¹⁰⁴ One reason has been a lack of diversity in synthetic protocols, which has hindered the development of pyrene-fused acenes with more diverse functionalities. This has largely prevented the comparison of pyrene-fused acenes to their respective acene counterparts. This chapter will explore the synthesis and characterization of a new series of vertical pyrenes, with the goal of investigating the impact of a pyrene delimiter on the electronic structure of acenes. The synthetic route employed allows for straightforward tuning of molecular length and for the addition of alkylsilylethyne groups, which makes possible a systematic investigation into the optoelectronic properties of vertical pyrenes compared to their acene counterparts. It was hypothesized that TIPS-Anthracene-Pyrene-Anthracene (**TIPS-APA**) will display electrochemical properties consistent with two separate TIPS-Anthracene chromophores separated by a central pyrene. TIPS-Pyrene-Anthracene (**TIPS-AP**), which features a single TIPS-Anthracene group fused to pyrene, should display electronic properties consistent with only a single acene-like chromophore. The optical gap and redox behaviors of these vertical pyrenes were analyzed experimentally through UV-Vis absorbance spectroscopy and cyclic voltammetry (CV), respectively. The solubility of these compounds was tuned by changing the nature of the alkylsilylethyne groups. Attention was then turned to the synthesis of vertical pyrenes featuring other acene chromophores, with the goal of optimizing this class of compounds for photophysical applications. As discussed in Chapter 1.7, acene dimers have proven useful in the study of photophysical

processes such as SF, and vertical pyrenes should present a rather unique case of a dimer with weak electronic communication between chromophores. The rigid structure of vertical pyrenes is rather unique in that the acene moieties reside in the same plane, and thus should fit the criteria for selective generation of ^5TT as predicted by the JDE model.⁵³ By tuning the length of the acene moieties, known SF chromophores can be incorporated into the vertical pyrene backbone, allowing for in-depth studies on the role of the pyrene linker in the SF capabilities in these systems.

2.2: Synthesis of TIPS-APA and TIPS-AP

The synthetic routes to AP and APA derivatives are shown in Figure 2.2 and Figure 2.3. The addition of *tert*-butyl groups to the 2,7 positions of pyrene, which occurs via Friedel-Crafts alkylation, increases the solubility of the ensuing intermediates and the final products. The oxidation of **1** was performed by way of a modified literature procedure.¹⁰⁵ By controlling the equivalents of the oxidizing reagent, either the 4,5,9,10-tetraone (**2**) or 4,5-dione (**2'**) can be achieved on large scales in acceptable yields. The addition of methyl Grignard to tetraone **2** followed by deoxygenation with hydriodic acid yields the tetramethylpyrene derivative **3**. Radical bromination of **3** using N-bromosuccinimide yields the precursor for a Cava reaction,¹⁰⁶ which can yield acene-quinones of varying length depending on the choice of starting material. The Cava reaction of **4** with 1,4-naphthoquinone gives **APA-Q**, which consists of two anthraquinone moieties fused to the central pyrene. The addition of TIPS-acetylide to **APA-Q** followed by deoxygenation with SnCl_2 and aqueous HCl yields **TIPS-APA**. Similarly, the lithiation of *n*-octyldiisopropylsilyl (NODIPS) acetylene followed by addition to **APA-Q** and subsequent deoxygenation provides **NODIPS-APA**.

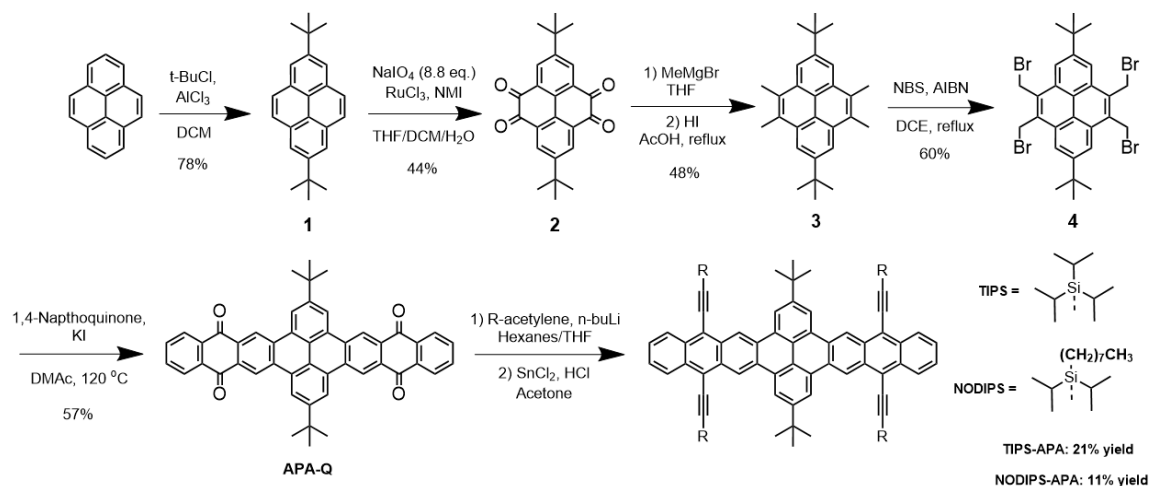


Figure 2:2: Synthetic route to **TIPS-APA**.

The synthetic routes to **TIPS-AP** and **NODIPS-AP** proceed via a similar route via functionalization of **2'**. However, the bromination of **3'** could not be achieved selectively, which resulted in substitution of bromine on the pyrene backbone. The excess bromine could not be removed selectively from the aromatic position of **4'**, but could be removed in the later stages of the reaction sequence. The addition of TIPS-acetylide to **Br-AP-Q** followed by deoxygenation gave **Br-TIPS-AP**. At this stage, the excess bromine was removed via an efficient palladium catalyzed debromination reaction¹⁰⁷ to give **TIPS-AP**. In the case of **NODIPS-AP**, bromine was removed by metal-halogen exchange performed on the diol intermediate, while subsequent deoxygenation yielded the final product.

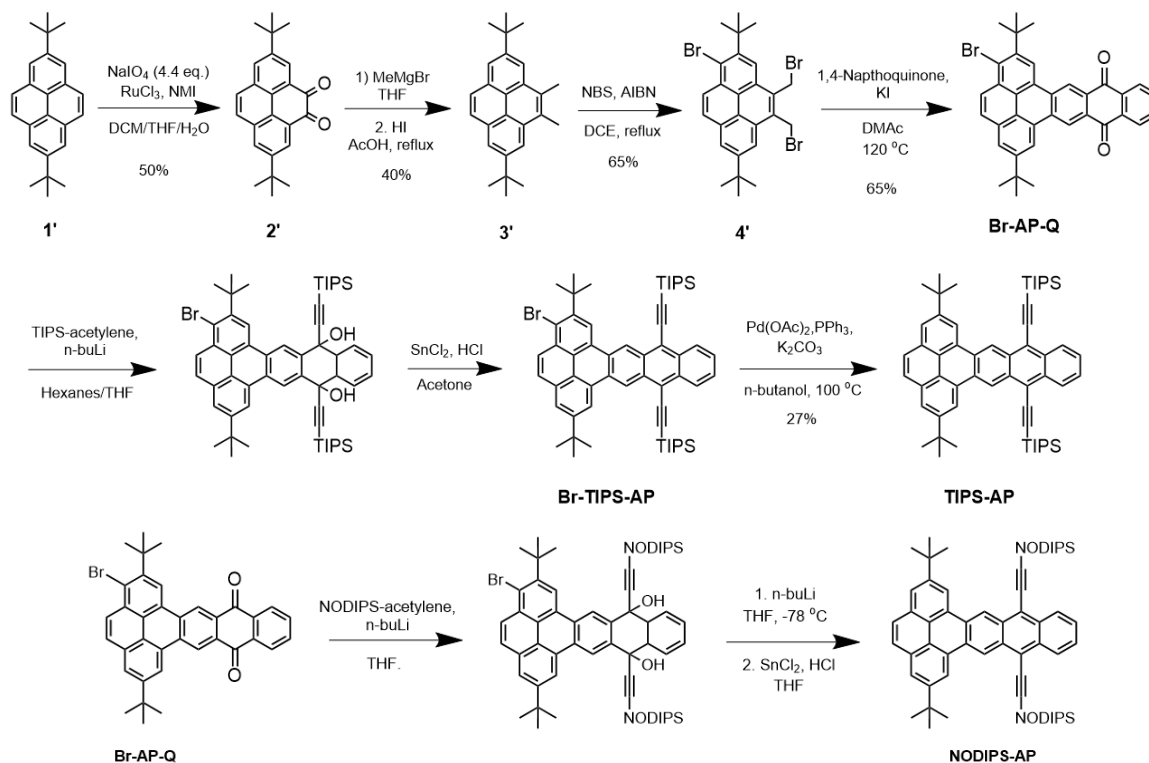


Figure 2:3: Synthetic route to **AP** derivatives.

2.3: Vertical Pyrene Properties

UV-Vis absorbance spectroscopy was employed to investigate the absorbance properties of the vertical pyrenes (Figure 2.4a). **TIPS-AP** and **TIPS-APA** both display an onset absorbance peak at 505 nm corresponding to a $S_0 \rightarrow S_1$ transition. The vibronic progression observed from 505 nm to 445 nm is characteristic of acenes,^{108,109} and is indicative of the acene-like character of the electronic structure in AP and APA. **TIPS-APA** shows an extinction coefficient twice that of **TIPS-AP** at 505 nm, which suggests that **TIPS-APA** contains two separate anthracene-like chromophores that undergo a $S_0 \rightarrow S_1$ transition. The redox properties of **TIPS-APA** and **TIPS-AP** were analyzed using CV (Figure 2.4b). Both compounds feature similar onset oxidation (1.1 V) and reduction (-1.4 V) potentials, while **TIPS-APA** shows an apparent 2nd oxidation peak at 1.2 V. Considering that the onset oxidation and reduction potentials loosely correlate with the energies of the HOMO and LUMO, respectively, such redox properties

indicate similar FMOs in **TIPS-AP** and **TIPS-APA**. The presence of two oxidation peaks could indicate some overlap between the acene-like HOMOs, resulting in a slight amount of HOMO delocalization and perturbation of the oxidation potential. However, the small degree of separation between the two peaks indicates that the two radical cations are localized primarily on the acene moieties. Thus, the experimental results from UV-Vis and CV support the hypothesis that pyrene disrupts conjugation in vertical pyrenes, yielding two acene moieties with nearly identical electronic structures.

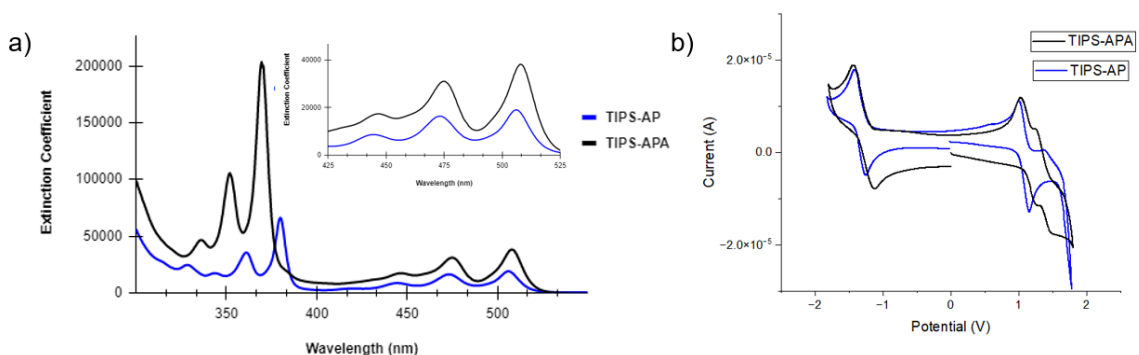


Figure 2:4: a) Extinction coefficient and b) CV spectra for **TIPS-AP** and **TIPS-APA**.

To determine the origin of these electronic properties, the Risko group investigated the electronic structure of AP and APA through DFT calculations. Figure 2.5a shows the effect of pyrene insertion on the FMOs of AP and APA.¹⁰⁴ The orbital geometries of the HOMO and LUMO in AP are more reminiscent of a tetracene than anthracene, and are localized primarily on the acene segment with some delocalization onto the central pyrene moiety. This is reflected in the absorbance spectra, as AP and APA both demonstrate an onset absorbance peak that is redshifted by ~ 70 nm from TIPS-Anthracene and is blue-shifted ~ 30 nm from TIPS-Tetracene.¹¹⁰ The HOMO of APA appears to be delocalized across the entire molecule, which would be consistent with the multiple oxidation peaks observed in the CV spectrum. However, the acene-like HOMOs are in fact arranged tail-to-tail with minimal interaction, just as the tetracene-like LUMOs appear completely isolated from each other. The relatively small energy splitting

(35 meV) between the HOMO and HOMO-1, which is isolated on the anthracene segments, implies limited interaction between the acene and pyrene moieties.¹⁰⁴ NICS values were calculated for AP and APA to examine the aromaticity of the pyrene-acenes relative to anthracene. The NICS spectra in Figure 2.5b show a clear resemblance between anthracene and the anthracene segments of AP and APA, providing further evidence of the acene-like character in these vertical pyrenes.

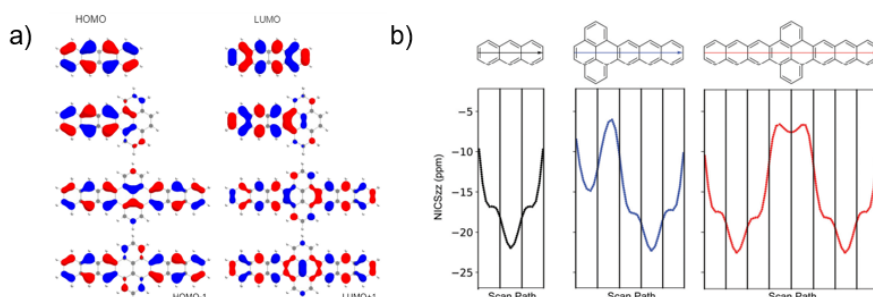


Figure 2:5: a) FMO and b) NICS scans for **TIPS-AP** and **TIPS-APA**.

2.4: Vertical Pyrenes for Photophysical Studies

Due to the disrupted conjugation observed in APA and confirmed through calculations, vertical Pyrenes can be thought of as dimer systems consisting of two separate acene chromophores separated by a pyrene linker. As discussed in Section 1.7, acene dimers have proven useful in the study of photophysical processes such as SF, and our vertical pyrene systems present a rather unique case of a rigid, planar dimer with extremely weak electronic communication between chromophores. In the case of **TIPS-APA**, the chromophores are TIPS-anthracene, which traditionally does not meet the energetic requirements to efficiently undergo SF.¹¹¹ While the $S_0 \rightarrow S_1$ gap for **TIPS-APA** (2.46 eV) is smaller than that of TIPS-Anthracene (2.83 eV), $2T_1$ is still greater than twice the S_1 energy in **TIPS-APA** ($T_1 = 1.5$ eV).¹⁰⁴ SF in **TIPS-APA** is thus expected to be endothermic by ~ 0.5 eV. However, TIPS-anthracene has received attention as an annihilator in triplet-triplet annihilation (TTA), the process by which two lower energy triplets combine to form a higher energy singlet.¹¹² Dimers capable of

performing intramolecular TTA are of growing interest for PV applications in order to offset the losses associated with insufficient photon energy.¹¹³ Given that $2T_1 > S_1$ in APA, such a system could meet the energetic requirements for TTA.¹¹⁴ Investigations into the efficiency and mechanisms of TTA in APA derivatives are currently ongoing with the help of collaborators. **NODIPS-APA** and **NODIPS-AP** were selected for these studies, as their enhanced solubilities compared to their TIPS-substituted counterparts make them more conducive for in-depth solution-based studies.

Silylethyne-substituted tetracenes and bis(phenylethynyl)anthracenes (BPEA) are systems whose SF properties have been well documented, and were discussed in Section 1.7. As shown in Section 2.2, the synthetic route to **TIPS-APA** utilizes a Cava reaction which can be used to tune the length of the aromatic backbone as well as the nature of the alkylsilylethyne groups. The following section details the synthesis of a NODIPS-substituted tetracene-pyrene-tetracene (**NODIPS-TPT**) and phenylethynyl-substituted APA (**TNPS-PE-APA**), as well as their corresponding monomers (**NODIPS-TP**, **TNPS-PE-AP**). The absorbance and electrochemical properties of these vertical pyrenes were evaluated and compared to those of **TIPS-AP** and **TIPS-APA** to determine the effect of pyrene fusion on acenes of varying length. Then, in-depth photophysical studies were performed by collaborators to determine if a pyrene-fused dimer motif is conducive for SF.

2.5: Synthesis of Vertical Pyrenes for Photophysical Applications

Figure 2.6 shows the synthesis of **NODIPS-TPT** and **NODIPS-TP**. The key step in both routes involves the Cava reaction of **4** and **4'** with 1,4-anthraquinone, which provides **TPT-Q** and **Br-TP-Q** respectively. Addition of NODIPS-acetylide to **TPT-Q** followed by deoxygenation with SnCl_2 yields the fully aromatized **NODIPS-TPT**, whose structure was confirmed by X-ray crystallography. Like the synthetic route to **TIPS-AP**, an additional debromination step is required to yield **NODIPS-TP**. Due to the instability of **Br-NODIPS-TP** at high temperature, the palladium-catalyzed debromination used in the synthesis of AP derivatives

resulted in complete degradation of starting material, with no recovery of the desired product. Therefore, excess bromine was removed by metal-halogen exchange, while subsequent deoxygenation provided **NODIPS-TP**.

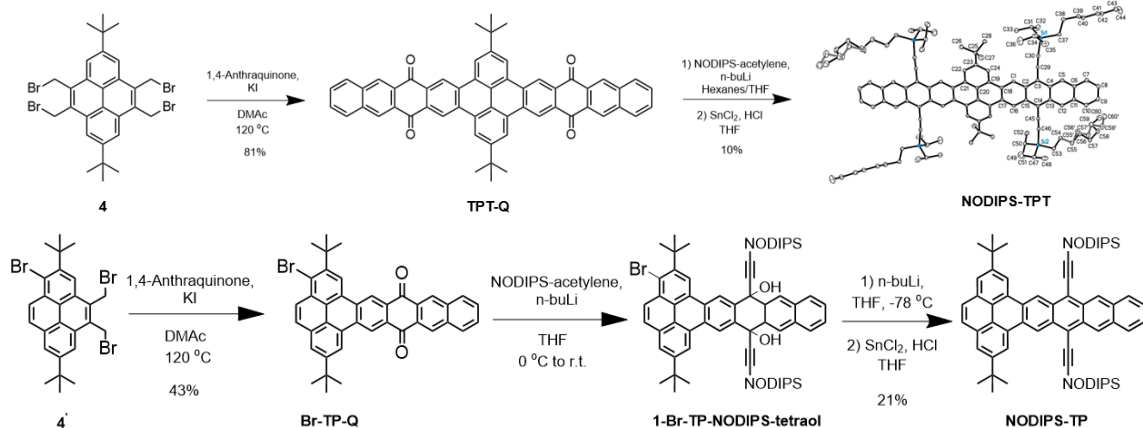


Figure 2:6: Synthetic routes to **NODIPS-TPT** and **NODIPS-TP**.

The synthesis of phenylethynyl-substituted AP and APA derivatives utilized quinone intermediates **APA-Q** and **Br-AP-Q**. To induce solubility in the final products, it was necessary to synthesize phenylacetylenes featuring silyl groups. This was done via metal-halogen exchange on 1,4-dibromobenzene to allow addition of the appropriate tri-*n*-propylsilylchloride, followed by sonogashira coupling with TMS acetylene and deprotection to give the substituted phenyl acetylene (see experimental). Lithiation of the phenylacetylenes and addition to **APA-Q** followed by deoxygenation with SnCl₂ provided **TNPS-PE-APA**, whose structure was confirmed by X-ray crystallography. **Br-TNPS-PE-AP** was obtained in a similar manner, and was stable enough to undergo Pd-catalyzed debromination at high temperature. However, the poor solubility of the starting material necessitated the use of dioxane as a solvent, with just enough *n*-butanol to act as a hydrogen source.

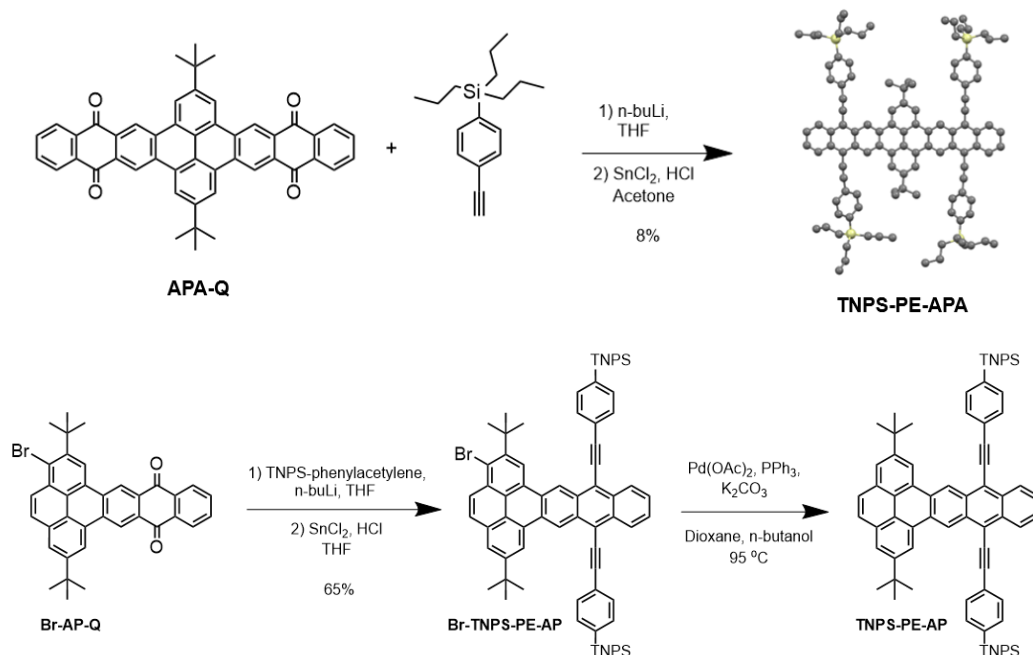


Figure 2:7: Synthetic routes to **TNPS-PE-APA** and **TNPS-PE-AP**.

The UV-Vis absorption spectra in Figure 2.8 shows the effect of pyrene-fusion on acene moieties of varying length and functionality. As noted previously, the onset absorbance for **TIPS-AP** is redshifted by ~70 nm compared to TIPS-Anthracene. This trend holds for **NODIPS-TP**, whose onset absorbance band at 603 nm is redshifted by ~70 nm compared to ethynyl-substituted tetracenes.¹¹⁰ Additionally, **NODIPS-TP** is redshifted by ~100 nm relative to **TIPS-AP**, which is consistent with the 100 nm redshift in absorbance observed in the linear acene series.³⁰ In **TNPS-PE-AP**, the extended conjugation induced by the phenylethynyl substituents results in a redshift in absorbance of 30 nm relative to **TIPS-AP**, consistent with a similar shift in BPEA compared to TIPS-anthracene.¹¹⁵ These trends are significant in that they provide evidence that the electronic properties of acene moieties can be tuned in a manner similar to that seen in their linear acene counterparts.

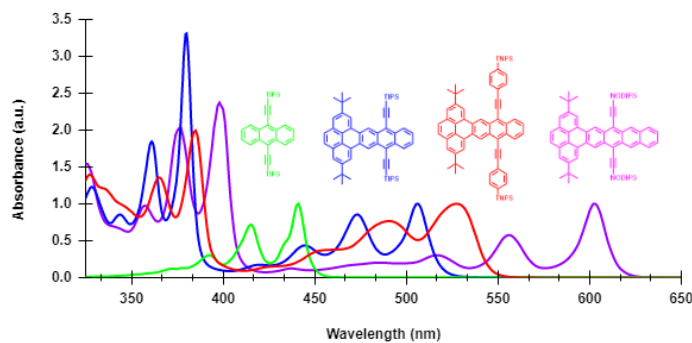


Figure 2:8: UV-Vis absorbance spectrum of vertical pyrenes.

2.6: NODIPS-TPT: Photophysical Properties and SF

Figure 2.9a shows the UV-Vis absorbance data for **NODIPS-TPT** and **NODIPS-TP**. Both compounds feature an acene-like vibronic progression of the $S_1 \leftarrow S_0$ transition from 625 nm to 500 nm, with the 0-0 peak centered at 603 nm. The molar extinction coefficient for **NODIPS-TPT** is twice that of **NODIPS-TP** at the initial onset absorbance peak, suggesting that the tetracene moieties in TPT are only weakly coupled similar to **APA**. This weak coupling is further evidenced by cyclic voltammograms of **NODIPS-TPT** and **NODIPS-TP** (Figure 2.9b), in which both compounds feature similar onset oxidation (~ 0.45 V) and reduction (~ -1.5 V) potentials. **NODIPS-TPT** also features a second oxidation peak, similar to that seen in the CV of **TIPS-APA**, suggesting a slight degree of overlap between the acene-like HOMOs. These results confirm that the TPT framework functions as a weakly-coupled dimer consisting of two tetracene chromophores bridged by a pyrene moiety, and that pyrene-fusion impacts the FMOs of vertical pyrene derivatives in a consistent manner.

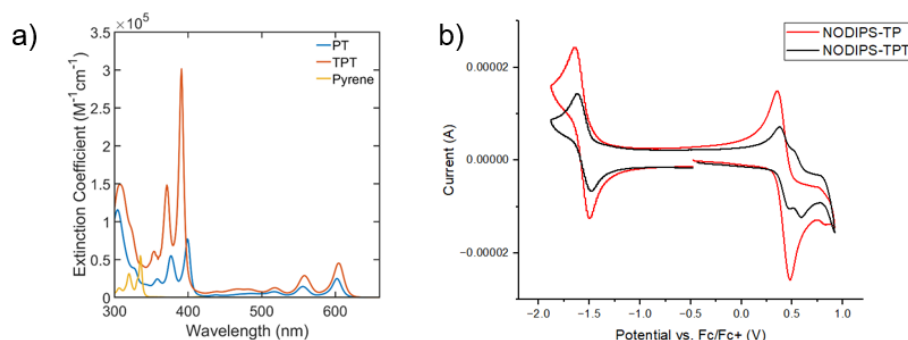


Figure 2:9: a) Extinction coefficient and b) CV spectra for **NODIPS-TP** and **NODIPS-TPT**.

The SF capabilities of TPT were investigated by the Johnson group at NREL and the Damrauer group at the University of Colorado.¹¹⁶ The emission quantum yield drops from 100% in **NODIPS-TP** to 6% in **NODIPS-TPT**. Transient absorption spectroscopy shows that the initial S_1 formed upon excitation of the **TPT** decays almost entirely to the 1TT state. The equilibrium between S_1 and 1TT strongly favors the latter, with an estimated singlet fission yield of 94%, considerably higher than previously reported rigid tetracene dimers. This can be rationalized by considering that the acene moieties in **TPT** energetically resemble pentacenes more so than tetracenes, as evidenced by the $S_1 \leftarrow S_0$ absorption energy. The SF rate for **NODIPS-TPT** at room temperature (4.5 ps) is approximately twice as fast as the rate at 77 K (9.3 ps), which indicates temperature dependence on the rate of SF. While this temperature dependence may suggest a slightly endothermic SF process (i.e. $^1TT > S_1$) for TPT, the highly favorable formation of 1TT is more in line with exothermic SF observed in many pentacene dimers.

The 1TT state was found to decay via one of two pathways, with the dominant route decay to the ground state S_0 . The other pathway appears to consist of conversion to the 5TT state. While 5TT has been observed as an intermediate in the formation of T_1 in some SF systems, **TPT** appears rather unique in that the population is trapped in 5TT with no observed formation of T_1 . The favorable formation of 5TT can be attributed to a large exchange energy (J) between the chromophores, which in turn is due to **TPT** maintaining a rigid, co-

planar structure. DFT calculations showed that J was significantly larger in **TPT** compared to other dimers such as norbornyl-linked tetracenes. ^5TT was also found to be lower in energy than ^1TT , which would offer a plausible explanation as to the favorable rate of $^5\text{TT} \leftarrow ^1\text{TT}$. Such a large exchange energy between the tetracene chromophores could make formation of the two uncorrelated T_1 states, each of which maintain the same spin, from forming on the same molecule.

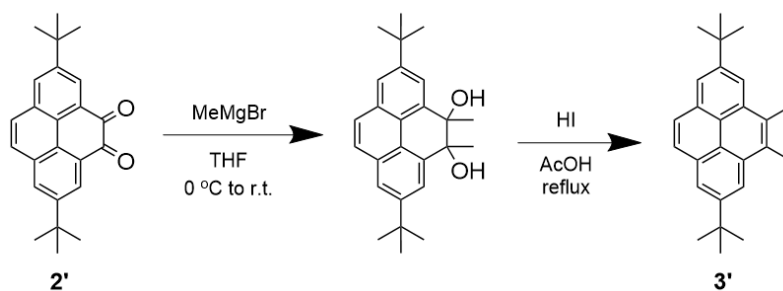
2.7: Vertical Pyrene Conclusions

A series of vertical pyrene derivatives were synthesized to determine the effect of pyrene-fusion on functionalized acenes. Absorbance and electrochemical data suggest that the acene moieties in APA derivatives are separated by the central pyrene, consistent with computational evidence. Tuning the length and functional groups on the acenes groups alters the electronic properties in a similar manner to traditional acenes. By lengthening the acene from an anthracene to a tetracene, a tetracene-pyrene-tetracene “dimer” was synthesized and studied for its singlet fission capabilities. **NODIPS-TPT** demonstrated formation of a long-lasting ^5TT state, with no observation of the uncorrelated T_1 state typically expected in SF dimers. While SF is typically studied with the goal of enhancing PV efficiency, the unique SF characteristics observed in **NODIPS-TPT** suggest that this system may be more suited for quantum computing applications. The unique SF process was attributed to the rigid, planar framework of the TPT dimer. It is currently unclear how the incorporation of a different SF chromophore, namely BPEA, into the vertical pyrene manifold will affect the mechanism of SF. These studies are currently underway in **TNPS-PE-APA**.

2.8: Experimental

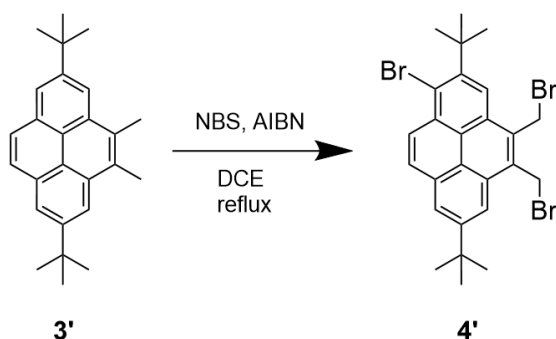
All reagents and solvents were obtained from Sigma Aldrich, Oakwood Chemicals, Gelest, or VWR and used without further purification. ^1H and ^{13}C NMR spectra were measured on a 400 MHz Bruker NMR spectrometer in CDCl_3

(7.26 ppm for ^1H NMR, 77.16 ppm for ^{13}C NMR) or 1,2-dichlorobenzene- d_4 (7.17 ppm and 7.40 ppm for ^1H NMR). MALDI TOF MS was analyzed on a Bruker Microflex LRF with no matrix. Solution UV-vis was recorded on an Agilent Carey 60 UV-Vis spectrophotometer. Cyclic voltammetry (CV) measurements were performed in either DCM or a DCM/dichlorobenzene mixture on a BASi Epsilon Potentiostat with a three-electrode cell, using 0.1 M $n\text{-Bu}_4\text{NPF}_6$ as supporting electrolyte, AgCl/Ag^+ as reference electrode, glassy carbon as working electrode, Pt wire as counter electrode, with scan rate at 100 mV/s. High resolution mass spectra (HRMS) were recorded using ESI as the ionization method. 2,7-di-*t*-butyl-pyrene, 2,7-di-*t*-butyl-4,5-pyrenedione, and 2,7-di-*t*-butyl-4,5,9,10-pyrenetetraone were prepared according to literature procedures.¹⁰⁵

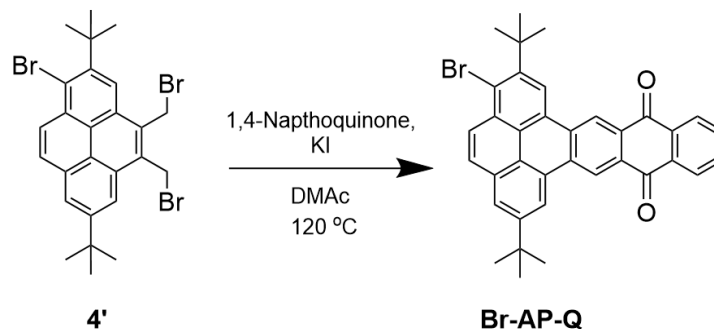


2,7-di-*t*-butyl-4,5-dimethylpyrene (3'): A 500 ml flame-dried round bottom (RB) flask cooled under N_2 atmosphere was charged with anhydrous THF (250 ml), and **2'** (8.00 g, 23.3 mmol) was dissolved and the solution cooled to $0\text{ }^\circ\text{C}$. A 3M Methylmagnesium bromide solution in THF (31.1 ml, 93.2 mmol, 4 eq.) was added slowly, and the reaction mixture was stirred for 14 hours at room temperature. The reaction was quenched carefully with water (50 ml) followed by 10% HCl (50 ml), the organic layer was extracted into ethyl acetate (100 ml) and washed with water (100 ml). The organic layer was dried with magnesium sulfate, and the solvent was removed. The crude product was purified via a silica plug in 3:1 hexanes:ethyl acetate. The recovered red solid was then dissolved in glacial acetic acid (250 ml) with hydriodic acid (4.00 ml) and was heated at reflux for 3 hours. The reaction mixture was allowed to cool to room temperature,

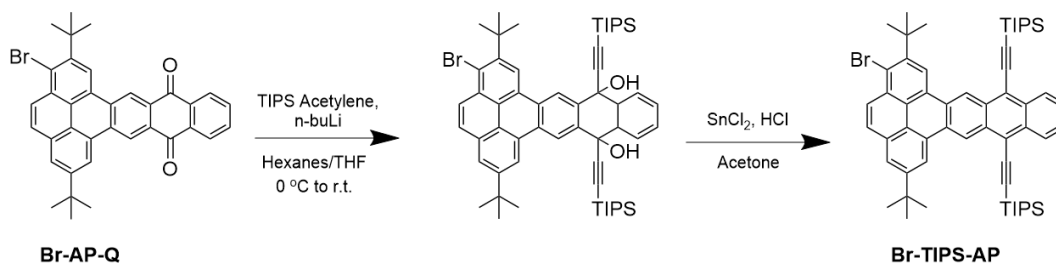
quenched with saturated aqueous sodium thiosulfate (100 ml), extracted into DCM (150 ml), and washed with water (100 ml). The organic layer was dried with magnesium sulfate, the solvent was removed, and the crude product purified by silica plug in 8:1 hexanes:DCM to give a white solid. GC-MS $m/z = 342.3$ (M^+). Yield for 2 steps: 3.21 g, 40%. $^1\text{H NMR}$ (400 MHz, CDCl_3): δ 8.45 (dd, $J_{\text{HH}} = 2.4$ Hz 2H), 8.22 (s, 2H), 8.07 (s, 2H), 2.97 (s, 6H), 1.67 (s, 18H). HRMS Calculated for $\text{C}_{26}\text{H}_{30}$: 342.2348. Found: 342.2383.



Bromo-2,7-di-*t*-butyl-4,5-dibromomethylpyrene (4'): In a 250 ml RB flask, **3'** (2.00 g, 5.84 mmol), N-bromosuccinimide (4.17 g, 23.4 mmol), and AIBN (50 mg) were dissolved in DCE (125 ml), and the solution was heated at reflux for 15 hours. The solution was allowed to cool to room temperature, at which point water (50 ml) was added. The mixture was extracted into DCM (100 ml) and washed with water (100 ml), the organic layer was dried with magnesium sulfate. After removal of the solvent, the crude solid was purified via silica plug in 7:1 hexanes:DCM to give **4'** as a yellow powder. Yield: 2.18 g, 65%

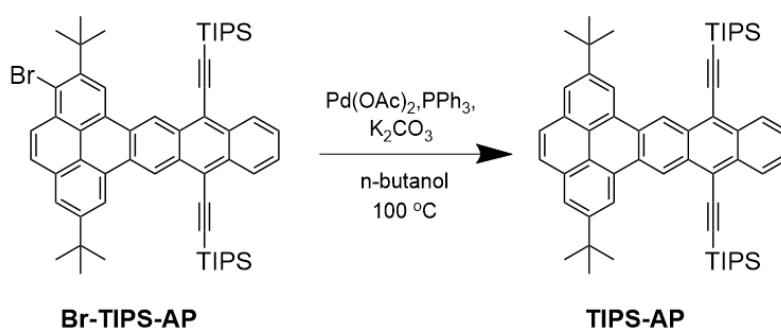


1-bromo-2,7-di-*t*-butyl-4,5-pyrene-anthraquinone (Br-AP-Q): A 150 ml sealed-tube reactor was charged with N,N-dimethylacetamide (50 ml), **4'** (2.00 g, 3.45 mmol), 1,4-naphthoquinone (2.14 g, 13.8 mmol, 4 eq.), and KI (5.73 g, 34.5 mmol, 10 eq.). The tube was sealed, and the reaction mixture was stirred at 120 °C for two days. The mixture was allowed to cool to room temperature, the lid was then removed, and the mixture was stirred open to air for 1 hour. The mixture was poured into 200 ml of water, then filtered. The recovered solid was added to 250 ml of acetone, sonicated for 10 minutes, and then filtered. The solid was then added to 250 ml THF, sonicated for 10 minutes, and filtered. **Br-AP-Q** was recovered as a yellow solid, and carried directly to the next step without further purification. Yield: 1.31 g, 65%.

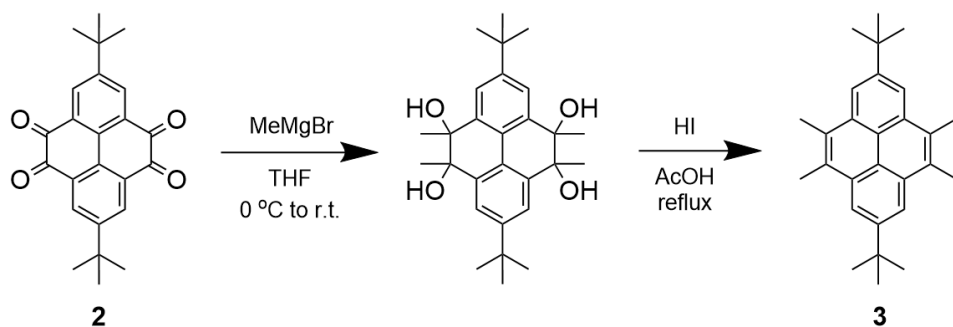


1-Bromo-TIPS-AP: A flame-dried 100 ml RB flask, cooled under N₂, was charged with 20 ml of hexanes and 5 ml of anhydrous THF. TIPS-acetylene (1.62 g, 8.88 mmol, 6 eq.) was added and the solution was cooled to 0 °C. 2.5 M *n*-butyllithium in hexanes (2.91 ml, 8.14 mmol, 5.5 eq.) was added slowly, and the solution was stirred for 30 minutes. **Br-AP-Q** (0.850 g, 1.48 mmol) was added,

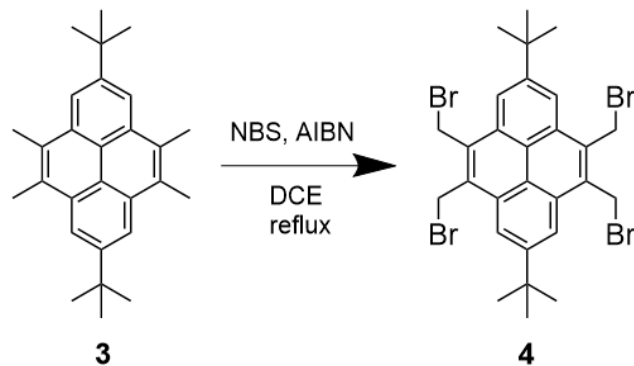
and the reaction mixture was stirred for 16 hours at room temperature. The reaction was quenched with water (20 ml) and 10% aqueous HCl (5 ml), and the organic layer was washed with water (50 ml). The organic layer was dried with magnesium sulfate, and the solvent removed. The crude product was dissolved in acetone (20 ml), and 0.500 g tin (II) chloride hydrate dissolved in 2 ml of 10% aqueous HCl was added slowly, and the mixture was stirred for 1 hour. The precipitated product was recovered via vacuum filtration, and then purified via column chromatography in 5:1 hexanes:DCM. Yield: 0.40 g, 30%.



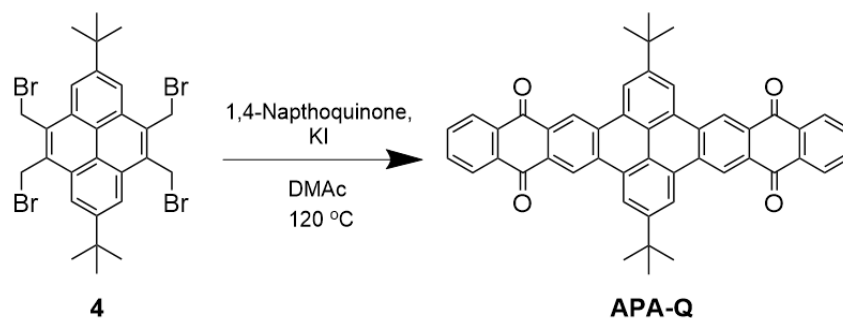
TIPS-AP: 20 ml of n-butanol was added to a 100 ml RB flask under N₂. Then **Br-TIPS-AP** (0.400 g, 0.442 mmol), Pd (II) acetate (19.8 mg, 88.4 μmol, 0.2 eq.), triphenylphosphine (23.2 mg, 88.4 μmol, 0.2 eq.), and potassium carbonate (0.122 g, 0.884 mmol, 2 eq.) were all added. The mixture was stirred at 100 °C under N₂ for 16 hours. The mixture was allowed to cool to room temperature and quenched with water (50 ml), extracted into ether (50 ml), washed with water (100), dried with magnesium sulfate, and the solvent was removed. The product was purified by silica plug in 9:1 hexanes:DCM then recrystallized from chlorobenzene. Yield: 0.10 g, 27%. ¹H NMR (500 MHz, 1,2-dichlorobenzene-d₄): δ 10.26 (s, 2H), 9.28 (s, 2H), 8.97 (dd, J_{HH} = 6.6 Hz, 2H), 8.1 (s, 2H), 7.42 (dd, J_{HH} = 6.8 Hz, 2H), 1.76 (s, 18H), 1.43 (m, 42H). HRMS (APCI with direct probe injection) for [M+1]⁺: calc. For C₅₈H₇₂Si₂: 824.5173, found: 824.5176.



2,7-di-*t*-butyl-4,5,9,10-tetramethylpyrene (3): A flame-dried RB flask under N₂ atmosphere was charged with anhydrous THF (250 ml) and **2** (5.00 g, 13.4 mmol), and the solution was cooled to 0 °C. A 3M methylmagnesium bromide solution in THF (26.8 ml, 80.4 mmol, 6 eq.) was added slowly, and the reaction mixture was stirred for 14 hours at room temperature. The reaction was quenched carefully with water (50 ml) and 10% HCl (50 ml), and the organic layer was extracted into ethyl acetate (100 ml) and washed with water (100 ml). The organic layer was dried with magnesium sulfate, and the solvent was removed. The crude product was purified via a silica plug in 3:1 hexanes:ethyl acetate. The recovered red solid was then dissolved in glacial acetic acid (250 ml) with hydriodic acid (8 ml) and heated at reflux for 3 hours. The mixture was allowed to cool to room temperature, quenched with saturated aqueous sodium thiosulfate (100 ml) and was then extracted into DCM (100 ml), and washed with water (100 ml). The organic layer was dried with magnesium sulfate, the solvent was removed, and the crude product was purified by silica plug in 8:1 hexanes:DCM to give **3** as a white powder. Yield for 2 steps: 2.38 g, 48%. ¹H NMR (400 MHz, CDCl₃): δ 8.42 (s, 4H), 2.96 (s, 12H), 1.67 (s, 18H). ¹³C NMR (101 MHz, CDCl₃): δ 147.59, 131.09, 129.68, 120.89, 117.99, 35.69, 32.26, 16.20. HRMS Calculated for C₂₈H₃₄: 370.2661. Found: 370.2697.

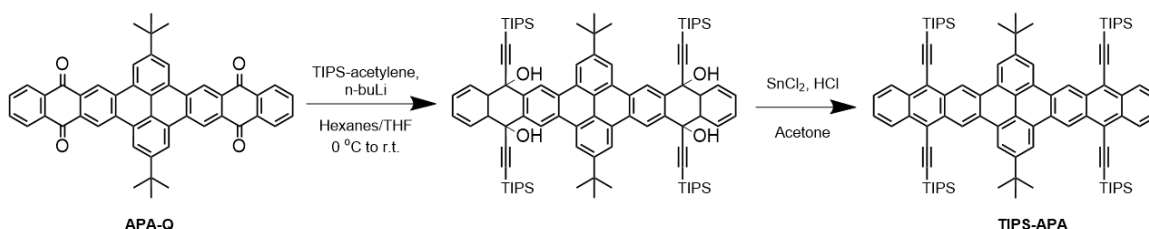


2,7-di-*t*-butyl-4,5,9,10-tetrabromomethylpyrene (4): In a 250 ml RB flask, **3** (2.00 g, 5.39 mmol), N-bromosuccinimide (5.76 g, 32.3 mmol, 6 eq.), and AIBN (50 mg) were dissolved in DCE (125 ml), and the solution was stirred at reflux for 18 hrs. The solution was allowed to cool to room temperature, at which point 100 ml water was added. The mixture was extracted into DCM and washed with water, dried with magnesium sulfate, and the solvent removed. The crude solid was purified via silica plug in 7:1 hexanes:DCM to give **4** as a yellow solid. Yield: 2.28 g, 60%.

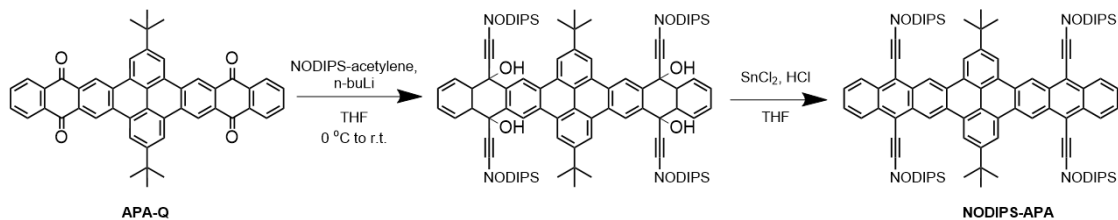


2,7-di-*t*-butyl-4,5,9,10-pyrenedianthraquinone (APA-Q): A 150 ml sealed-tube reactor was charged with 50 ml of DMAC, **4** (0.700 g, 1.02 mmol), 1,4-naphthoquinone (1.26 g, 8.16 mmol, 8 eq.), and KI (1.69 g, 10.2 mmol, 10 eq.) were added, the tube was sealed, and the mixture was stirred at 120 °C for two days. The mixture was allowed to cool to room temperature, the lid was removed, and the mixture was stirred for 1 hour open to air. The mixture was poured into 200 ml of water, then filtered. The recovered solid was added to 250 ml of

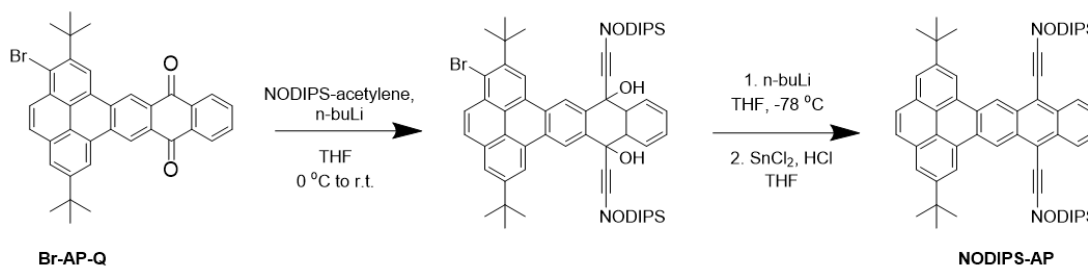
acetone, sonicated for 10 minutes, and then filtered. The solid was then added to 250 ml THF, sonicated for 10 minutes, and filtered. **APA-Q** was recovered as a yellow solid. Yield: 0.44 g, 65%. The insoluble quinone was carried directly to the next step.



TIPS-APA: A flame-dried 100 ml RB flask under N₂ atmosphere was charged with 20 ml of hexanes and 4 ml of anhydrous THF. TIPS-acetylene (0.728 g, 4.00 mmol, 9 eq.) was added and the solution was cooled to 0 °C. 2.5 M n-butyllithium in hexanes (1.51 ml, 3.77 mmol, 8.5 eq.) was added slowly, and the solution was stirred for 1 hour. **APA-Q** (0.300 g, 0.44 mmol) was added, and the mixture was stirred for 15 hours at room temperature. The reaction was carefully quenched with water (20 ml) and 10% HCl (5 ml), the mixture was extracted into diethyl ether (50 ml), and the organic layer was washed with water (50 ml). The organic layer was dried with magnesium sulfate, the solvent was removed, and the crude product was purified by silica plug in 6:1 hexanes:ethyl acetate. The resulting red oil was dissolved in acetone (20 ml) in a 100 ml round-bottom flask, and 0.600 g tin (II) chloride hydrate dissolved in 2 ml of 10% aqueous HCl was added slowly, and the mixture was stirred for 1 hour. The precipitated product was recovered via vacuum filtration, purified via column chromatography in 6:1 hexanes:DCM, and finally recrystallized from chlorobenzene. Yield: 0.12 g, 28%. ¹H NMR (500 MHz, 1,2-dichlorobenzene-d₄): δ 9.99 (s, 4H), 9.11 (s, 4H), 8.78 (dd, J_{HH} = 6.4 Hz, 4H), 7.65 (dd, J_{HH} = 6.8 Hz, 4H), 1.78 (s, 18 H), 1.48 (m, 84H). HRMS (APCI with direct probe injection) for [M+1]⁺: calc. For C₉₂H₁₁₈Si₄: 1334.8411, found: 1334.8409.

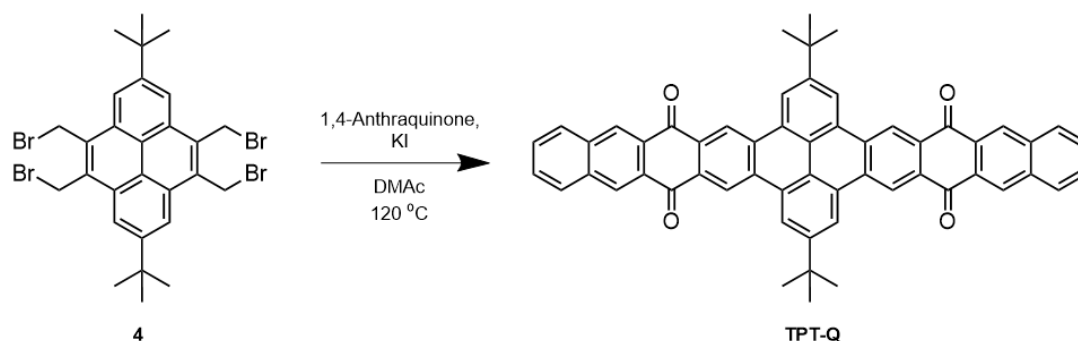


NODIPS-APA: A flame-dried 100 ml RB flask under N₂ atmosphere was charged with 20 ml anhydrous THF. NODIPS-acetylene (1.55 g, 6.16 mmol, 14 eq.) was added and the solution was cooled to 0 °C. 2.5 M n-butyllithium in hexanes (2.11 ml, 5.28 mmol, 12 eq.) was added slowly, and the solution was stirred for 1 hour. **APA-Q** (0.300 g, 0.44 mmol) was added, and the mixture was stirred for 15 hours at room temperature. The reaction was carefully quenched with water (20 ml) and 10% HCl (5 ml), the mixture was extracted into diethyl ether (50 ml), and the organic layer was washed water (50 ml). The organic layer was dried with magnesium sulfate, the solvent was removed, and the crude product was purified by silica plug in 8:1 hexanes:ethyl acetate. The resulting red oil was dissolved in THF, and a solution of 0.800 g tin (II) chloride dissolved in 2 ml 10% aqueous HCl was added dropwise. The solution was then stirred for 1 hour, at which point 20 ml water was added and the mixture was extracted into diethyl ether (50 ml) and washed with water (50 ml). The organic layer was dried with magnesium sulfate, the solvent was removed, and the crude product was purified by column chromatography using 19:1 hexanes:DCM. Yield: 0.21 g, 30%. ¹H NMR (400 MHz, CDCl₃): δ 10.03 (s, 4H), 9.15 (s, 4H), 8.77 (dd, *J* = 3.2, 3.6 Hz, 4H), 7.65 (dd, *J* = 3.2, 3.6 Hz, 4H), 1.78 (s, 18H), 1.74 (m, 4H), 1.51 (q, *J* = 7.2 Hz, 8H), 1.34 (m, 64H), 1.25 (m, 48H), 1.03 (t, *J* = 8.4 Hz, 8H), 0.82 (t, *J* = 6.8 Hz, 8H). ¹³C NMR (101 MHz, CDCl₃): 149.40, 133.17, 131.00, 130.36, 129.66, 127.48, 126.81, 123.45, 121.84, 120.71, 118.59, 106.16, 103.60, 35.49, 34.02, 31.95, 29.35, 24.80, 22.67, 18.82, 18.53, 14.10, 12.17, 10.55.

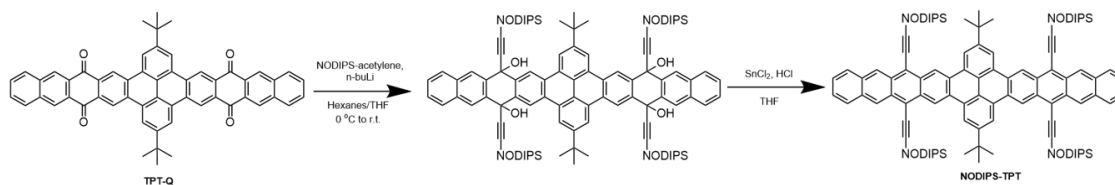


NODIPS-AP: A flame-dried 100 ml round-bottom flask under N₂ atmosphere was charged with 15 ml anhydrous THF. NODIPS-acetylene (1.22 g, 4.84 mmol, 7 eq.) was added and the solution was cooled to 0 °C. 2.5 M n-butyllithium in hexanes (1.66 ml, 4.14 mmol, 6 eq.) was added slowly, and the solution was stirred for 30 minutes. **Br-AP-Q** (0.400 g, 0.693 mmol) was added, and the reaction mixture was stirred for 16 hours at room temperature. The reaction was quenched with water (20 ml) 10% HCl (5 ml), the mixture was extracted into diethyl ether (20 ml), and the organic layer was washed with water (50 ml). The organic layer was dried with magnesium sulfate, and the solvent removed. The crude product was purified on a silica plug (8:1 hexanes:ethyl acetate) to give a dark red oil. The oil was then added to a flame-dried 100 ml round bottom flask under N₂ atmosphere along with 40 ml anhydrous THF. The solution was cooled to -78 °C, at which point 2.5 M n-butyllithium in hexanes (3.4 ml, 8.3 mmol) was added slowly. After stirring for 5 minutes, the reaction was slowly quenched with 5 ml MeOH and allowed to warm to room temperature. Then, 0.500 g tin (II) chloride hydrate dissolved in 2 ml of 10% aqueous HCl was added dropwise, and the mixture was stirred for 1 hour. The mixture was poured into water (50 ml) and extracted into diethyl ether (50 ml). The organic layer was dried with magnesium sulfate and, after removal of the solvent, was purified by column chromatography in hexanes to give the product as a yellow powder. Yield: 62 mg, 9.3%. ¹H NMR (400 MHz, CDCl₃): δ 10.08 (s, 2H), 9.16 (s, 2H), 8.77 (dd, *J* = 3.2, 3.6 Hz, 2H), 8.17 (s, 2H), 8.00 (s, 2H), 7.65 (dd, *J* = 3.2, 3.2 Hz, 2H), 1.72 (m, 4H), 1.69 (s, 18H), 1.45 (q, *J* = 7.6 Hz, 8H), 1.38 (m, 64H), 1.23 (m, 48H), 1.02 (t, *J* = 8.4 Hz, 8H), 0.82 (t, *J* = 6.8 Hz, 8H). ¹³C NMR (101 MHz, CDCl₃): 148.81, 133.13, 131.45, 130.99, 130.62, 129.02, 127.45, 126.75, 123.89, 123.19, 121.74, 119.09,

118.54, 106.07, 103.61, 35.33, 33.98, 31.92, 29.31, 24.77, 22.63, 18.52, 14.05, 12.17, 10.54.

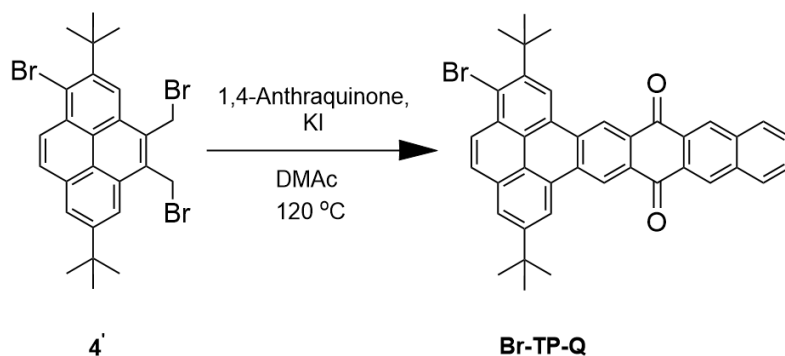


2,7-di-*t*-butyl-4,5,9,10-pyrenebis(tetracenequinone) (TPT-Q): A 150 ml sealed-tube reactor was charged with N,N-dimethylacetamide (50 ml), **4** (1.20 g, 1.75 mmol), 1,4-anthraquinone (1.46 g, 7.00 mmol, 4 eq.), and potassium iodide (2.91 g, 17.5 mmol, 10 eq.). The tube was sealed, and the mixture was stirred at 120 °C for two days. The mixture was allowed to cool to room temperature, the lid was removed, and the mixture was stirred open to air for 1 hour. The mixture was poured into 200 ml of water, then filtered. The recovered solid was added to 250 ml of acetone, sonicated for 10 minutes, and then filtered. The solid was then added to 250 ml THF, sonicated for 10 minutes, and filtered. The final crude product was recovered as a light brown solid. Yield: 1.1 g, 81%. The insoluble quinone was carried directly to the next step.



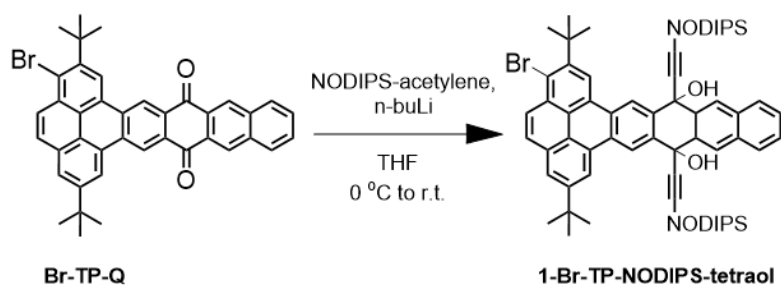
NODIPS-TPT: A flame-dried 100 ml RB flask under N₂ atmosphere was charged with 18 ml of hexanes and 9 ml of anhydrous THF. NODIPS-acetylene (2.05 g, 8.12 mmol) was added and the solution was cooled to 0 °C. 2.5 M *n*-butyllithium in hexanes (3.09 ml, 7.72 mmol) was added slowly, and the solution was stirred

for 1 hour. **TPT-Q** (0.300 g, 0.387 mmol) was added, and the mixture was stirred for 16 hours at room temperature. The mixture was quenched with water (20 ml) and 10% HCl (5 ml), and the organic layer was extracted into diethyl ether and washed with water (50 ml). The organic layer was dried with magnesium sulfate, the solvent removed, and the organic layer was purified via silica plug in 5:1 hexanes:ethyl acetate. After the solvent was removed, the dark red oil was dissolved in THF (20 ml), and tin (II) chloride hydrate (0.400 g, 1.77 mmol) dissolved in 2 ml 10% HCl was added dropwise, and the solution was stirred for 1 hr. The mixture was quenched with water (20 ml), extracted into diethyl ether (50 ml) and washed with water (50 ml), and the organic layer was dried with magnesium sulfate and the solvent removed. The product was then purified by column chromatography in 10:1 Hexanes:DCM to give **NODIPS-TPT** as a purple solid. Crystals were obtained from a 2:1 ethyl acetate:toluene solution. Yield: 71 mg, 11%. ¹H NMR (400 MHz, CDCl₃): δ 10.02 (s, 4H), 9.46 (s, 4H), 9.13 (s, 4H), 8.07 (dd, *J* = 7.2, 3.2 Hz, 4H), 7.51 (dd, *J* = 6.8, 3.0 Hz, 4H), 1.80 (s, 18H), 1.77 (m, 8H) 1.55 (m, 8H), 1.45 (m, 8H), 1.41 (m, 56H), 1.40 (m, 8H), 1.30 (m, 8H), 1.22 (m, 16H), 1.06 (m, 8H), 0.80 (t, *J* = 6.8 Hz, 12H). HRMS (APCI with direct probe injection) for [M+1]⁺: calc. For C₁₂₀H₁₆₂Si₄: 1715.1754, found: 1715.1798.

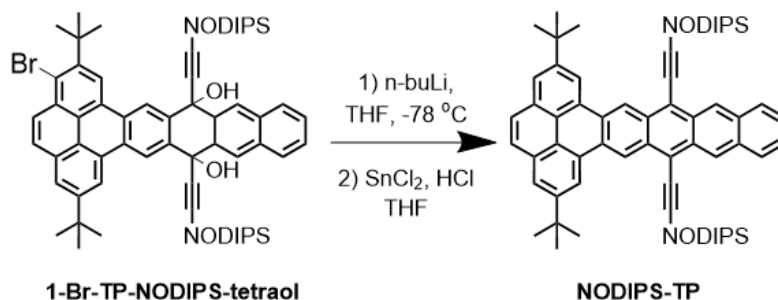


1-bromo-2,7-di-t-butyl-4,5-pyrene-tetracenequinone (Br-TP-Q): A 150 ml sealed-tube reactor was charged with N,N-dimethylacetamide (50 ml), **4'** (1.22 g, 2.10 mmol), 1,4-anthraquinone (1.75 g, 8.40 mmol, 7 eq.), and potassium iodide (2.79 g, 16.8 mmol, 8 eq.) were added, the tube was sealed, and the mixture was

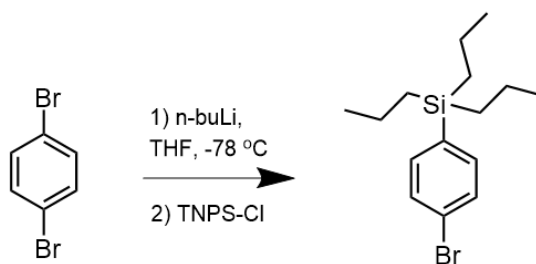
stirred at 120 °C for two days. The mixture was allowed to cool to room temperature, the lid was then removed, and the mixture was stirred open to air for 1 hour. The mixture poured into 200 ml of water, then filtered. The recovered solid was added to 250 ml of acetone, sonicated for 10 minutes, and then filtered. The solid was then added to 250 ml THF, sonicated for 10 minutes, and then filtered. **Br-TP-Q** was recovered as a light brown solid and used in the next step without further purification. Yield: 0.81 g, 62%.



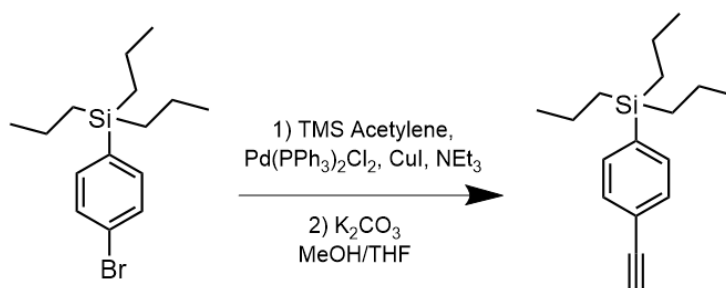
1-bromo-TP-NODIPS-diol: A flame-dried 100 ml RB flask under N₂ atmosphere was charged with 20 ml of anhydrous THF and NODIPS-acetylene (1.21 g, 4.81 mmol, 10 eq.), and the solution was cooled to 0 °C. 2.5 M n-butyllithium in hexanes (1.73 ml, 4.33 mmol, 9 eq.) was added slowly, and the solution was stirred for 30 minutes. **Br-TP-Q** (0.300 g, 0.481 mmol) was added, and the mixture was stirred for 16 hours at room temperature. The reaction was quenched slowly with water (20 ml) and 10% HCl (5 ml), the mixture was extracted into diethyl ether (50 ml), and the organic layer was washed with water (50 ml). The organic layer was dried with magnesium sulfate, and the solvent removed. The product was purified via column chromatography in 6:1 hexanes:ethyl acetate to give a dark red oil, which was carried directly to the next step.



NODIPS-TP: 1-bromo-TP-NODIPS-tetraol (0.37 g, 0.36 mmol) was 100 ml RB flask under N₂. The flask was then charged with 40 ml anhydrous THF and then cooled to -78 °C. 2.5 M n-butyllithium in hexanes (1.73 ml, 4.32 mmol, ~12 eq.) was then added dropwise. After stirring for 5 minutes, the reaction was slowly quenched with 5 ml MeOH and allowed to warm to room temperature. Then, 0.500 g tin (II) chloride hydrate dissolved in 2 ml of 10% aqueous HCl was added dropwise, and the mixture was stirred for 1 hour. The mixture was poured into water (50 ml) and extracted into diethyl ether (50 ml). The organic layer was dried with magnesium sulfate and, after removal of the solvent, was purified by column chromatography in 12:1 hexanes:DCM to give **NODIPS-TP** as a purple solid. Yield: 0.10 g, 21%. ¹H NMR (400 MHz, CDCl₃): δ 10.07 (s, 2H), 9.45 (s, 2H), 9.16 (s, 2H), 8.15 (s, 2H), 8.06 (dd, *J* = 6.6, 3.2 Hz, 2H), 7.99 (s, 2H), 7.50 (dd, *J* = 6.6, 3.2 Hz, 2H), 1.76 (m, 4H), 1.70 (s, 18H), 1.53 (m, 4H), 1.44 (m, 4H), 1.40 (m, 28H), 1.28 (m, 4H), 1.21 (m, 8H), 1.05 (q, *J* = 8.4 Hz, 4H), 0.80 (t, *J* = 6.8 Hz, 6H). HRMS (APCI with direct probe injection) for [M+1]⁺: calc. For C₇₂H₉₄Si₂: 1014.6894, found: 1014.6870.

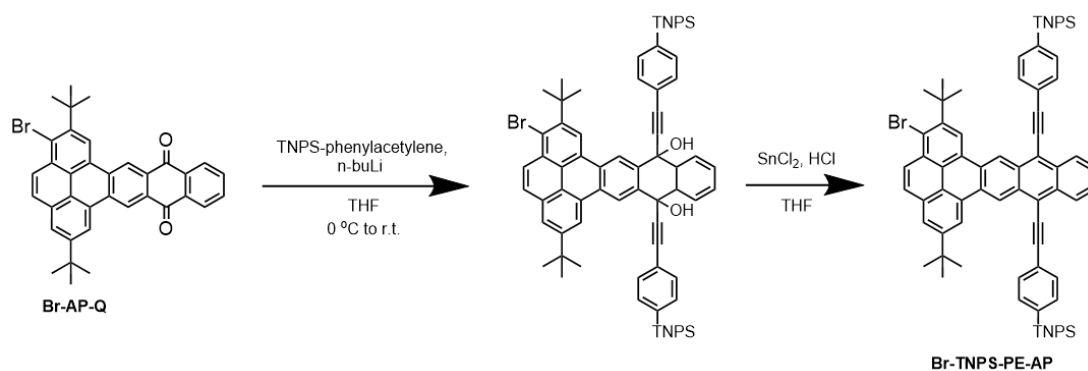


1-bromo-4-(tri-n-propylsilyl)benzene: To a flame-dried 250 ml RB flask under N_2 was added 1,4-dibromobenzene (10.2 g, 43.2 mmol) and 125 ml anhydrous THF. The flask was cooled to $-78\text{ }^\circ\text{C}$, then 2.5 M n-butyl lithium in hexanes (17.3 ml, 43.2 mmol, 1 eq.) was added slowly, and the solution was stirred at $-78\text{ }^\circ\text{C}$ for 1 hr. tri-n-propylsilyl chloride (10 g, 51.8 mmol, 1.2 eq.) was added, and the reaction mixture was allowed to stir at room temperature for 16 hours. The reaction mixture was quenched with water (50 ml) and extracted into hexanes (100 ml), washed with saturated aqueous ammonium chloride (100 ml), and the organic layer was dried with magnesium sulfate and the solvent was removed. The product was purified on a silica plug in hexanes to yield a colorless oil. Yield: 12.7 g, 94%.¹¹⁷



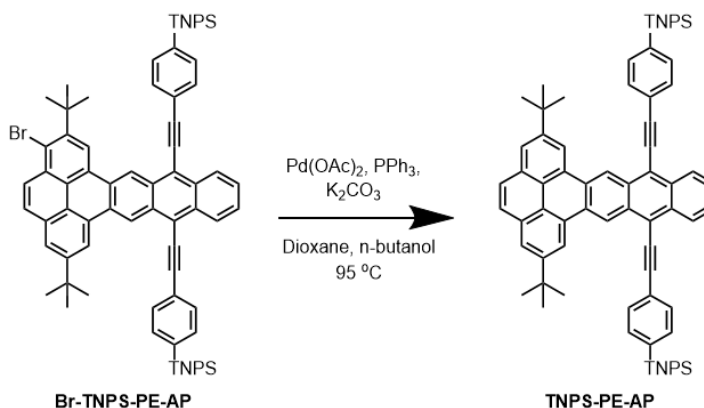
4-(tri-n-propylsilyl)phenylacetylene: 1-bromo-4-(tri-n-propylsilyl)benzene (8.00 g, 25.5 mmol), toluene (70 ml) and NEt_3 (25 ml) were added to a sealed-tube reactor, and the solution was purged with N_2 for 30 min. Then, $PdCl_2(PPh_3)_2$ (0.890 g, 1.27 mmol, 5 mol%), CuI (0.485 g, 2.55 mmol, 10 mol%), and TMS-acetylene (4.72 ml, 38.3 mmol, 1.5 eq.) were added sequentially. The tube was sealed, and the reaction was stirred for 16 hours at $80\text{ }^\circ\text{C}$. The reaction mixture

was allowed to cool to room temperature, poured into 50 ml hexanes, and then flushed through a thin pad of silica in hexanes. The solvent was removed, and the product was purified via a silica plug in hexanes to yield a colorless oil. The oil was then dissolved in 80 ml MeOH and 20 ml THF, and K_2CO_3 (4.1 g, 30 mmol) was added, and the reaction was stirred for 1 hr., at which point the reaction was complete by GC-MS. The reaction was quenched with water (50 ml) and 10% HCl (20 ml), extracted into hexanes (50 ml), washed with water (100 ml) and dried with magnesium sulfate. After removal of the solvent, the crude product was purified by silica plug in hexanes to give the final product as a colorless oil. Yield: 5.7 g, 89%.¹¹⁷

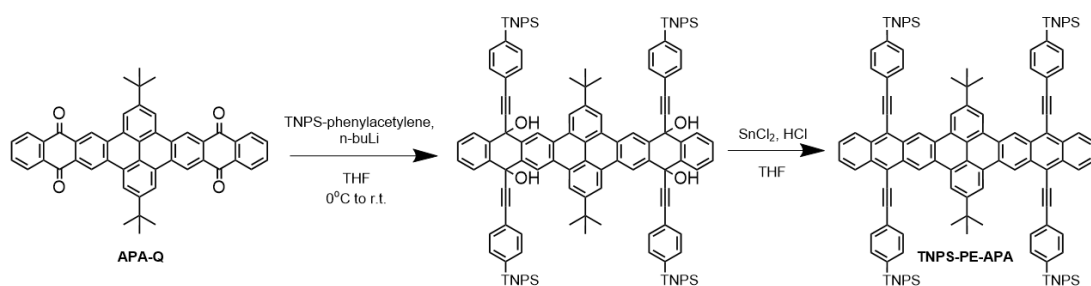


Br-TNPS-PE-AP: A flame-dried 100 ml RB flask under N₂ was charged with 20 ml anhydrous THF. TNPS-phenyl acetylene (0.629 g, 2.43 mmol, 7 eq.) was added, and the solution was cooled to 0 °C. 2.5 M n-butyllithium in hexanes (1.25 ml, 3.12 mmol, 6 eq.) was added slowly, and the reaction mixture was stirred for 30 min. Br-AP-Q (0.300 g, 0.524 mmol) was added, and the solution was stirred overnight at room temperature. The reaction was quenched with water (20 ml) and 10% HCl (5 ml), extracted in diethyl ether (50 ml) and washed with water (50 ml), and the organic layer was dried with magnesium sulfate. After removal of solvent, the product was purified on a silica plug (5:1 hexanes: ethyl acetate) to give the diol as a dark red oil. The oil was then redissolved in THF (20 ml), and tin (II) chloride hydrate (0.55 g, 2.5 mmol) dissolved in 2 ml 10% aq. HCl was added dropwise to the solution, and the reaction mixture was stirred for 1 hr.

The reaction was quenched with water (20 ml), extracted into diethyl ether (50 ml) and washed with water (50 ml), and dried with magnesium sulfate. After removal of solvent, the product was purified via column chromatography in 6:1 hexanes:DCM. Yield: 0.36 g, 65%. This product was carried on to the debromination step without further purification.



TNPS-PE-AP: **Br-TNPS-PE-AP** (0.200 g, 0.189 mmol) was dissolved in 12 ml dioxane and 3 ml of n-butanol in a 100 ml RB flask under N_2 . Pd (II) acetate (9 mg, 0.04 mmol, 20 mol%), triphenylphosphine (10 mg, 0.04 mmol 20 mol%), and potassium carbonate (55 mg, 0.38 mmol, 2 eq.) were all added. The solution was heated at 100 °C under N_2 for 16 hours. The mixture was allowed to cool to room temperature, and was then poured into water (50 ml) and extracted into diethyl ether (50 ml), washed with water (50 ml), and the organic layer was dried with magnesium sulfate. After the solvent was removed, the crude product was purified by silica plug in 6:1 hexanes:DCM to yield **TNPS-PE-AP** as a red powder. Yield: 96 mg, 52%. $^1\text{H NMR}$ (400 MHz, CDCl_3): δ 10.15 (s, 2H), 9.22 (s, 2H), 8.74 (dd, $J = 3.2, 3.6$ Hz, 2H), 8.17 (s, 2H), 7.98 (s, 2H), 7.91 (d, $J = 8.0$ Hz, 4H), 7.65 (m, 6H), 1.71 (s, 18H), 1.47 (sx, $J = 7.2$ Hz, 12H), 1.08 (t, $J = 7.2$ Hz, 18H), 0.93 (m, 12H).



TNPS-PE-APA: A flame-dried 100 ml RB flask under N₂ was charged with 20 ml anhydrous THF. TNPS-phenylacetylene (1.6 g, 6.95 mmol, 13.5 eq.), and the solution was cooled to 0 °C. 2.5 M n-butyllithium in hexanes (2.45 ml, 6.1 mmol, 12 eq.) was added slowly, and the reaction mixture was stirred for 30 min. **APA-Q** (0.35 g, 0.51 mmol) was added, and the solution was stirred overnight at room temperature. The reaction was quenched with water and 10% aq. HCl, extracted in diethyl ether, and the organic layer was dried with magnesium sulfate. After removal of solvent, the product was purified on a silica plug to give the tetraol as a dark red oil. The oil was then redissolved in THF (20 ml), and tin (II) chloride hydrate (0.8 g, 3.6 mmol) dissolved in 2 ml 10% aq. HCl was added dropwise to the solution, and the reaction mixture was stirred for 1 hr. The reaction was quenched with water, extracted into diethyl ether, and dried with magnesium sulfate. After removal of solvent, the crude product was purified via column chromatography in 5:1 hexanes:DCM to give **TNPS-PE-APA** as a red powder. Crystals were obtained from toluene. Yield: 67 mg, 8.1%. ¹H NMR (400 MHz, CDCl₃): δ 9.02 (s, 4H), 8.61 (dd, *J* = 3.6, 3.2 Hz, 4H), 7.93 (d, *J* = 8 Hz, 8H), 7.66 (d, *J* = 8 Hz, 8H), 7.46 (dd, *J* = 3.6, 3.2 Hz, 8H), 1.71 (s, 18H), 1.49 (m, 24H), 1.09 (t, *J* = 7.2 Hz, 36H), 0.94 (t, *J* = 8.4 Hz, 24H).

Chapter 3: Synthesis and Properties of Extended Acenoacenes

3.1: Introduction to Oblique Pyrenes

The electronic properties of pyrene-fused acenes systems are expected to be dependent on the orientation of the central pyrene moiety, as the computational results reported by Risko were largely corroborated in the case of vertical pyrene-delimited acenes.¹⁰⁴ In the case of oblique pyrene-fused acenes, the whole molecule is expected to be fully conjugated, in stark contrast to vertical pyrenes.¹⁰³ An example of such a system is a silylethynyl-substituted “bistetracene” reported by Anthony and Briseño, which can be considered as a pyrene core with naphthalene moieties fused at the 1,2 and 6,7 positions (Figure 3.1a).⁸⁵ This compound also belongs to a family of molecules commonly known as “acenoacenes”, which can be thought of as two acenes fused together at their *peri* positions to create a 2-D nanographene with two aromatic sextets. There have been several literature reports of acenoacenes of varying length and annulation mode, virtually all of which display small optical and electrochemical gaps as well as impressive stability.^{34,85,86,87,118} For example, Frigoli has reported bispentacene derivatives (Figures 3.1b,c) with different annulation modes, both of which feature red-shifted absorption and enhanced stability compared to TIPS-Pentacene. While Frigoli’s bispentacenes displayed hole mobilities on the order of $1 \text{ cm}^2 \text{ V}^{-1} \text{ S}^{-1}$, theoretical mobilities suggest that TIPS-PPP may have semiconducting properties on par with TIPS-pentacene, which may be experimentally accessible through device optimization.^{86,87} The inherent charge transport properties of these bispentacenes can be attributed to their large transfer integrals, as their large polyaromatic structures provide more opportunity for intermolecular overlap. The large rigid structures also result in small reorganization energies, another key factor in achieving efficient charge transport. The bispentacenes reported by Frigoli mark the largest silylethynyl-substituted acenoacenes currently in the literature, while oblique pyrenes larger than bistetracene have not been reported. It is worth noting that the synthetic

routes to previously reported acenoacenes do not allow for straightforward tuning of the length of the aromatic core, which has largely inhibited systematic studies on the evolution of electronic properties and stability within this class of materials.

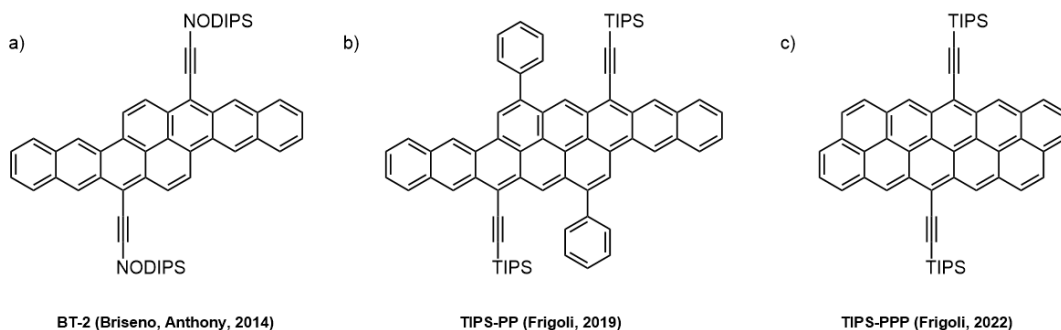


Figure 3:1: 2-D acenoacenes of varying size and annulation mode.

This chapter describes the synthesis and basic electronic characteristics of a series of extended acenoacenes. The synthetic protocol provides access to the longest acenoacenes reported to date, and allows for a systematic study on the effects of linear ring annulation on their electronic structure. While functionalized bispentacenes (BP) observe enhanced stability compared to their linear counterparts, the stability of acenoacenes as large as bishexacene (BH) and bisheptacene (BHep) remains unexplored. The later sections of this chapter describe experimental stability measurements in conjunction with computational studies, with the goal of finding the cause of the remarkable stability in acenoacenes. Also described are attempts to optimize our acenoacenes for application in OFETs by tuning the solid-state ordering and through studies on dynamic disorder in these materials.

3.2: Synthesis of Oblique Pyrenes

The synthetic route to BP involves the pyrene-dianhydride intermediate **3** originally reported by Clar, which can be synthesized on large scales using relatively cheap starting materials. The esterification of **3** provides more soluble intermediate **4**, whose structure was unambiguously confirmed

crystallographically. Reduction of tetraester **4** was initially attempted using DIBAL-H and LAH, however large amounts of aluminum byproducts combined with the poor solubility of **5** made purification difficult. However, reduction with LiBH_4 allowed for high yields of **5** with simple work-up. Bromination of **5** with PBr_3 gave the Cava precursor **6**. The Cava reaction¹⁰⁶ between **6** and 1,4-naphthoquinone provided bispentacenequinone (**BP-Q**), while a similar reaction with 1,4-antraquinone gave bishexacenequinone (**BH-Q**), showing the versatility of o-bromomethyl precursors to afford polyaromatic cores of varying length.

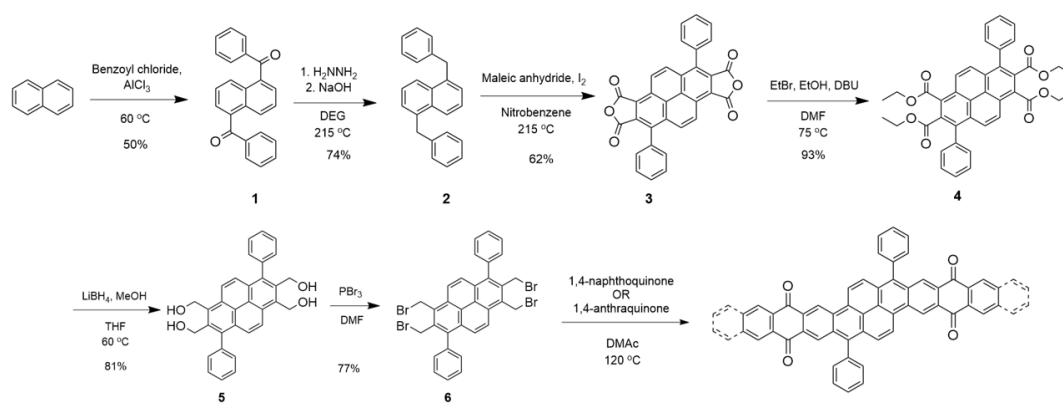


Figure 3:2: Synthetic route to acenoacene quinones.

The formation of the acenoacenes was accomplished with similar silylethynylation chemistry to that demonstrated in Chapter 2, which consists of the addition of a lithiated silylacetylene to the appropriate quinone, followed by reductive deoxygenation with SnCl_2 . The synthesis of initial acenoacenes utilized NODIPS-acetylene to provide **NODIPS-BP** and **NODIPS-BH**. For both compounds, initial deoxygenation conditions using SnCl_2 in 10% aqueous HCl provided only trace amounts of the final products. For **NODIPS-BP**, the yields in the final step were significantly improved by using trifluoroacetic acid (TFA) in place of HCl. A plausible explanation is that use of a strong organic acid resulted in a more homogeneous solution compared to the reaction mixture containing an aqueous acid. In the case of **NODIPS-BH**, the best yields were obtained using SnCl_2 in toluene without the use of an acid catalyst, as such conditions mitigated undesired side product formation. X-ray quality crystals of both **NODIPS-BP** and

NODIPS-BH were obtained from ethyl acetate/toluene mixtures. The long octyl chains on the NODIPS groups provided ample solubility of **NODIPS-BP** and **NODIPS-BH** in most common organic solvents, allowing for straightforward characterization. In order to determine the impact of smaller alkylsilyl substituents on solid-state ordering, derivatives featuring tri-*n*-propylsilyl (TNPS) substituents were synthesized under similar conditions. X-ray quality crystals were obtained of **TNPS-BH** from toluene, which allowed for structure confirmation by x-ray crystallography. The crystal packing for these compounds will be discussed further in Section 3.5.

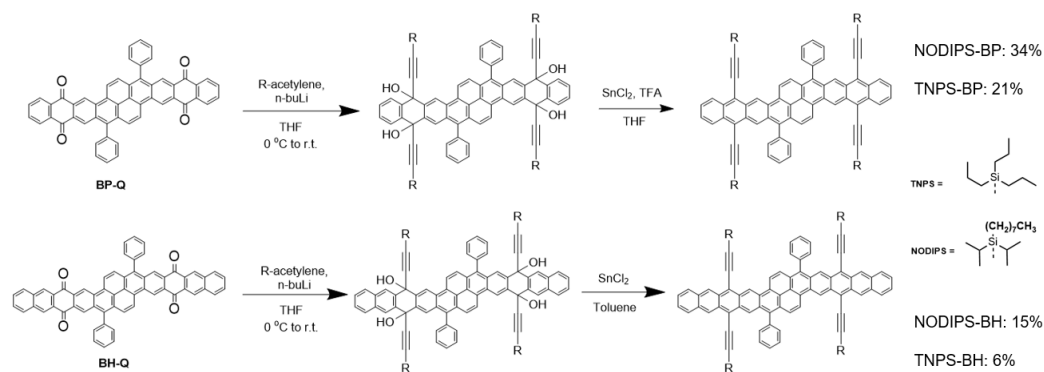


Figure 3:3: Synthesis of NODIPS-BP and NODIPS-BH.

To probe the limits of the stability in our acenoacene series, we turned our attention to the synthesis of a NODIPS-substituted bisheptacene derivative, which features two fused heptacene moieties and 14 consecutively fused rings. After the synthesis of 1,4-tetraquinone according to a literature procedure,¹¹⁹ the Cava reaction with **6** gave **BHep-Q**. It should be noted that due to the extremely poor solubility of **BHep-Q** and the resulting side products, it is likely that **BHep-Q** contained impurities, which resulted in relatively low yields of the **NODIPS-BHep-tetrol** intermediate. Initial attempts at deoxygenation of the tetraol to provide **NODIPS-BHep** did not yield any of the target product. While TLC showed immediate conversion to a product that was potentially **NODIPS-BHep**, this product decomposed before it could be isolated. Such difficulty in characterizing

NODIPS-BHep under ambient conditions indicates that a significant drop-off in stability exists between BH and BHep derivatives.

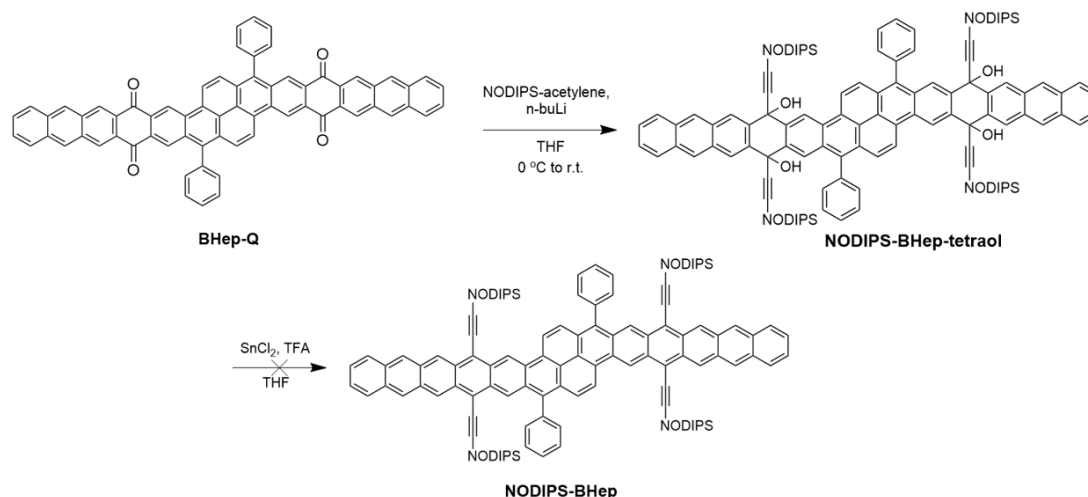


Figure 3:4: Attempted synthesis of **NODIPS-BHep**.

3.3: Properties of Acenoacenes

As shown in the UV-Vis absorbance spectrum in Figure 3.5, **NODIPS-BP** and **NODIPS-BH** feature onset absorbance peaks at 774 nm and 890 nm, respectively. Both compounds feature a vibronic progression characteristic of acenes,^{108,109} stretching from 800 nm to 600 nm for **NODIPS-BP**, and 900 nm to 700 nm for **NODIPS-BH**. Such absorption patterns indicate that, despite their 2-D polyaromatic structure, acenoacenes feature acene-like evolution of optical properties with linear ring fusion. The molar extinction coefficients for **NODIPS-BP** and **NODIPS-BH** were calculated as 38,100 M⁻¹cm⁻¹ (774 nm) and 37,400 M⁻¹cm⁻¹ (890 nm), respectively, both of which are larger than that reported for **TIPS-Pen** (20,000 M⁻¹cm⁻¹).¹²⁰

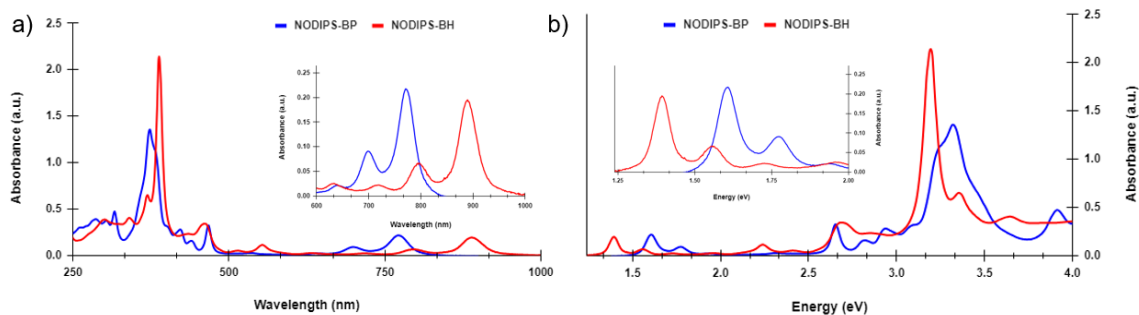


Figure 3:5: UV-Vis absorption spectrum of **NODIPS-BP** and **NODIPS-BH** as a function of (a) wavelength and b) eV.

The redshifted absorption peaks of oblique pyrenes relative to vertical pyrenes of similar size provide evidence of the complete conjugation across the aromatic core expected in oblique pyrenes, in stark contrast to the broken conjugation observed in vertical pyrenes. The origin of the small optical gaps observed in **NODIPS-BP** and **NODIPS-BH** relates to frontier molecular orbitals of BP and BH (Figure 3.6), which are delocalized across the aromatic backbone. For both compounds, the HOMO-1 and LUMO+1 are localized primarily on the acene moieties, and are reminiscent of the HOMOs and LUMOs of linear acenes, i.e. tetracene in the case of BH. However, the energy splitting between the HOMO and HOMO-1 in BP (0.64 eV) and in BH (0.51 eV) are much larger than in APA (0.35 eV),¹⁰⁴ and thus acenoacenes maintain a ground state electronic structure that is consistent with full conjugation.

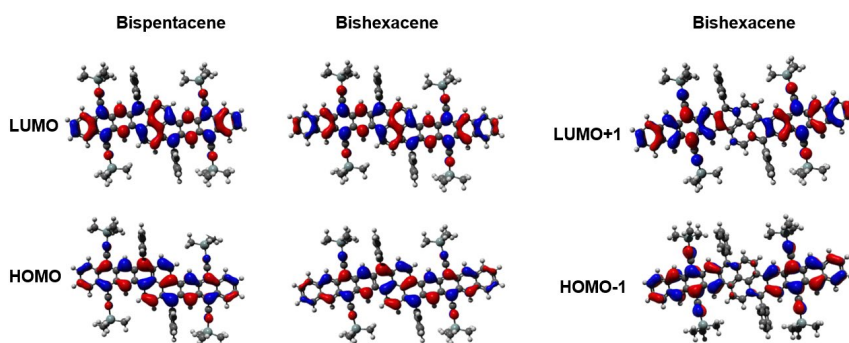


Figure 3:6: Frontier molecular orbitals of acenoacenes.

The redox properties of **NODIPS-BP** and **NODIPS-BH** were probed using CV (Figure 3.7). The onset oxidation/reduction potentials vs. Fc/Fc^+ were 0.14/-1.44 V for **NODIPS-BP**, and 0.037/-1.29 V for **NODIPS-BH**. These oblique pyrenes display smaller electrochemical gaps than vertical pyrenes, such as APA and TPT, as their large, fully conjugated cores help to stabilize the resulting cation or anion upon oxidation or reduction, respectively. Linear fusion of additional benzene rings results in destabilization of the HOMO and stabilization of LUMO, following the trend seen in both the linear acene series and previously reported acenoacenes.³⁴ Both compounds display multiple reversible oxidation and reduction peaks, with smaller separation between the reduction peaks in **NODIPS-BP** (0.18 V) compared to that observed between the oxidation peaks (0.45 V). This separation is further narrowed between the first two reduction peaks in **NODIPS-BH** (0.14 V), compared to a difference of 0.38 V between the first two oxidation potentials. This could suggest that the radical anion is more localized than the radical cation in these acenoacenes, resulting in decreased charge repulsions in the dianion compared to the dication.¹²¹ While previously reported bistetracenes and bispentacenes have shown up to two oxidation and two reduction peaks, the larger BH core can accommodate up to 3 positive or negative charges, as evidenced by the 3 reversible oxidation and reductions peaks in **NODIPS-BH**.¹²²

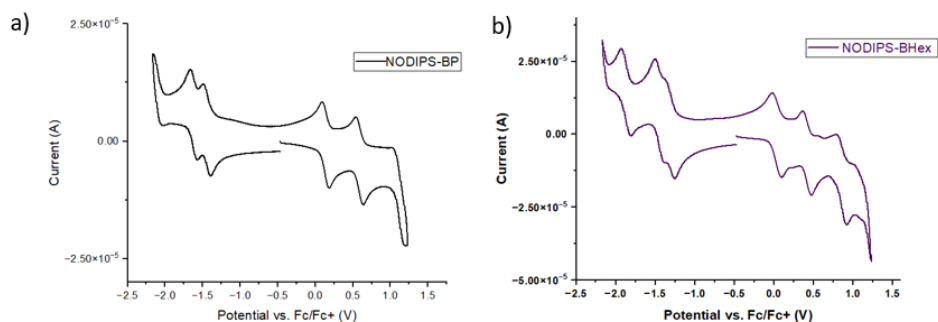


Figure 3:7: CV spectra of (a) **NODIPS-BP** and (b) **NODIPS-BH**.

NODIPS-BP and **NODIPS-BH** display impressive stability under ambient laboratory conditions, and even upon prolonged exposure to an intense white

light source. Much like previously reported acenoacenes, **NODIPS-BP** and **NODIPS-BH** show significantly longer lifetimes compared to **TIPS-Pen** in solution (Figure 3.8). There can be seen an apparent solvent-dependence on the stability of both compounds, consistent with previously reported stability studies on **TIPS-Pen**.¹²³ Surprisingly, **NODIPS-BH** appears more resistant to photooxidation than **NODIPS-BP** in both solvents tested. This is despite the fact that **NODIPS-BH** displays a longer, linearly extended backbone, which has traditionally been associated with decreased stability in acene-derivatives. Also of interest is the rate at which the compounds decompose. **NODIPS-BP** appears to display exponential decay, while **NODIPS-BH** decomposes in a linear manner. While the exact reason for this difference in decomposition rate warrants further study, it is possible that the decomposition product for **NODIPS-BP** catalyzes the further decay of the starting material and thus results in a faster rate of reaction over time.

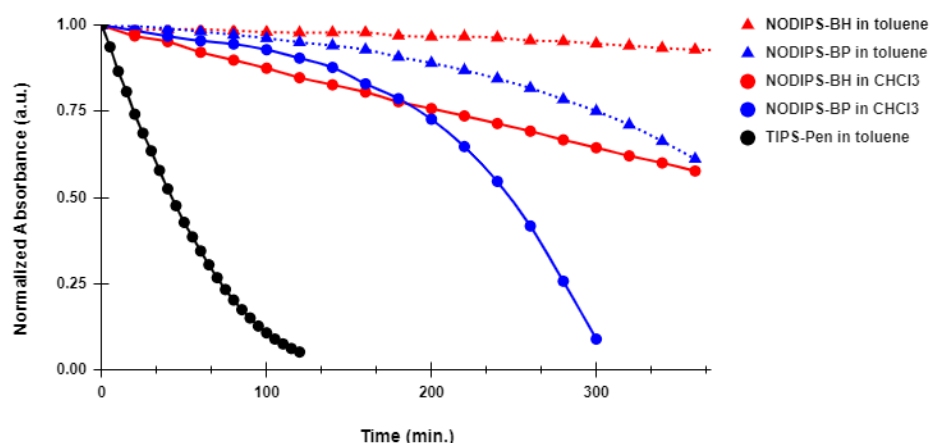


Figure 3:8: Stability studies displaying the max onset absorbance as a function of time under white light exposure.

The photoluminescent (PL) properties of **TNPS-BH** were explored with the help of the Ostroverkhova lab. Figure 3.9a shows the PL spectra, which are dominated by a peak at 710 nm. This result was surprising as emission from acenes typically occurs from S_1 , which in the case of **TNPS-BH** is represented by the lower energy absorption peak at 890 nm. Near-IR PL spectra does in fact

show a small peak centered at 920 nm, consistent with emission from S_1 , but this peak is quite small compared to the feature at 710 nm. The emission peak at 710 nm appears to overlap with the 0-2 absorption peak of the $S_0 \rightarrow S_1$ progression, however emission from this level would violate Kasha's rule and is therefore unlikely. One possibility is that this peak originates from a highly emissive impurity, such as a decomposition product of **TNPS-BH**. This is supported by absorbance spectrum of a partially degraded TNPS-BH solution after 3 months in the dark (Figure 3.9b). The absorption peak at 890 nm diminishes as the peak at 700 nm increases, which is consistent with the formation of decomposition product with broken conjugation along one of the acene moieties. The PL spectra of the degraded **TNPS-BH** solution is still dominated by the emission peak at 710 nm, which seems to suggest that this peak originates from this decomposition product. However, more in-depth PL studies are needed in order to better understand the optoelectronic properties of these acenoacenes.

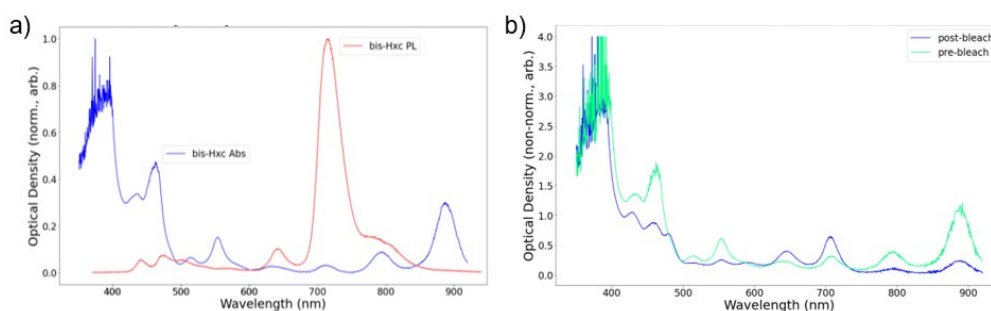


Figure 3:9: (a) absorbance and PL spectra for **TNPS-BH** and (b) absorbance spectra of **TNPS-BH** (blue) and decomposed **TNPS-BH**.

3.4: Stability in Acenoacenes

Computational methods were employed to study the reactivity of a series of extended acenoacenes with singlet oxygen (1O_2) to better understand their impressive stability. Figure 3.10a shows the activation energies for the reaction with 1O_2 on each ring in a series of acenoacenes and **TIPS-Pen**. The line highlighted in red represents the activation energy for the most reactive center ring of **TIPS-Pen**, and thus the ring most likely to undergo photooxidation. The

most reactive ring in BP has a slightly higher activation energy than ring 3 in **TIPS-Pen**, while the activation energies for rings 3 and 4 in BH are significantly lower. Figure 3.10b demonstrates the importance of silylethyne substitution on the reaction energies for the endoperoxide formation on each ring. Endoperoxide formation on ring 4, the ring featuring the silylethyne substituents, becomes much less favorable compared to the same ring on the unsubstituted acenoacenes, an effect that has been well-documented in **TIPS-Pen**.⁸⁴ The reaction energies for silylethyne-substituted BHep suggest that endoperoxide formation is highly favorable on at least three rings, which would offer a plausible explanation for the inability to isolate **NODIPS-BHep** under ambient conditions.

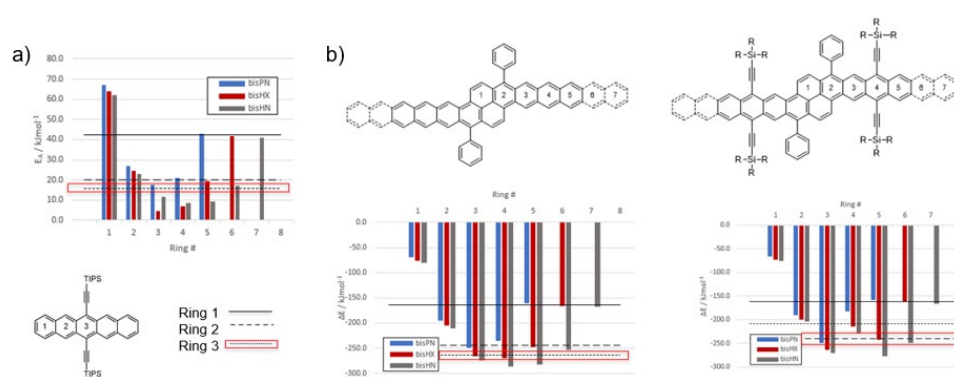


Figure 3:10: (a) Activation energy for the reaction of acenoacenes and TIPS-Pentacene with $^1\text{O}_2$ on each ring, (b) Reaction energies for acenoacenes with $^1\text{O}_2$ to form the endoperoxide on each ring.

The relatively large activation energies and small (less negative) reaction energies calculated for BP suggest that it is both kinetically and thermodynamically less reactive with $^1\text{O}_2$ than **TIPS-Pen**. Such calculations are in good agreement with experimental observations, as **NODIPS-BP** displays much longer solution lifetimes than **TIPS-Pen**. The potent reactivity with $^1\text{O}_2$ predicted for BHep is also supported by the apparent instability of **NODIPS-BHep** under ambient conditions. BH is unusual, as it shows considerably lower activation energies in the reaction with $^1\text{O}_2$ compared to BP, and even the silylethyne-substituted analogue should be more prone to photooxidation than BP. However, **NODIPS-BH** appears more stable than **NODIPS-BP**, even under

prolonged exposure to intense white-light. Table 3.1 shows the calculated S_1 and T_1 energies for silylethyne-substituted bisacenes, in which the diminishing S_0 - S_1 gap with increased length also correlates with lower T_1 energies. Because the triplet energy (0.57 eV) of **NODIPS-BH** is considerably lower than the 3O_2 Δ_{ST} (0.98 eV), it is possible that the photoexcitation of **NODIPS-BH** does not result in the generation of 1O_2 at an appreciable rate. As discussed in Section 1.7, photooxidation of bistetracene has been found to operate primarily by an energy transfer mechanism, meaning that decomposition is correlated with efficient generation of 1O_2 . If longer acenoacenes, such as BH derivatives, undergo photooxidation via an energy transfer mechanism in a similar manner to bistetracenes, then slower generation of 1O_2 could substantially improve stability.

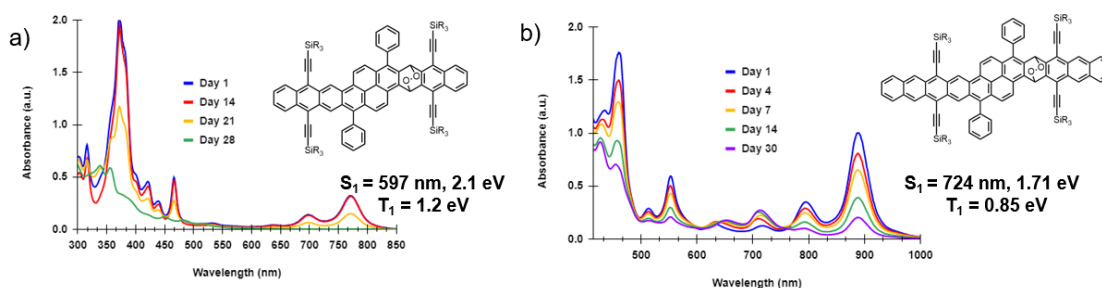


Figure 3:11: UV-Vis spectra of (a) NODIPS-BP and (B) NODIPS-BH under exposure to ambient laboratory light over 1 month, as well as energy levels of EPO products.

Samples of **NODIPS-BP** and **NODIPS-BH** in $CHCl_3$ were left under constant exposure to ambient laboratory light over the course of 1 month, and the decomposition of the samples was monitored by UV-Vis (Figure 3.11). The S_1 and T_1 energy levels were calculated for the EPO on the most reactive ring 3 for both systems, with the goal of identifying such decomposition products in the UV-Vis spectra. Interestingly, **NODIPS-BP** shows little apparent decay after two weeks, followed by rapid decay after 3 weeks and complete decay after 4 weeks. This unique decomposition pattern may be attributed to the initially slow formation of the EPO, which has a larger T_1 energy than **NODIPS-BP** and can thus more efficiently generate 1O_2 and thus accelerate the rate of decomposition via an energy-transfer mechanism. The decomposition of **NODIPS-BH** proceeds

linearly over the course of ~30 days, with the rise of a feature at 715 nm corresponding to the calculated absorbance of the endoperoxide on ring 3. The difference in decomposition rates can potentially be attributed to the T_1 energies of the EPO products: The T_1 energy (0.85 eV) for the identified BH EPO is predicted to be lower than that of the BP EPO and the singlet-triplet gap of O_2 (0.98 eV), and thus may not efficiently generate 1O_2 . More in-depth studies, likely featuring a combination of experimental and computational work, will be needed in order to further explore the role of T_1 in the stability of acenoacenes.

Table 3.1: Calculated S_1 and T_1 energies for acenoacenes and **TIPS-Pen**.

Compound	S_0-S_1 (eV)	T_0-T_1 (eV)
TIPS-Pen	1.88	0.89
SiR₃-BisPen	1.64	0.84
SiR₃-BisHex	1.34	0.57
SiR₃-BisHep	1.12	0.37

In order to investigate the role of aromaticity in acenoacene stability, NICSzz(1) calculations were performed on silylethyne-substituted BP and BH analogues. For both SiR₃-BP and SiR₃-BH, ring 3 displays the most negative chemical shift and thus the strongest aromaticity. In both these compounds, ring 3 also corresponds to the ring most prone to reaction with 1O_2 according to the reaction energies in Figure 3.11. In fact, the 2 most reactive rings (3 and 5) in SiR₃-BH are also the most aromatic according to NICS. This underscores that aromaticity indices such as NICS can prove to be misleading in the study of the stability of acenes and acene derivatives.

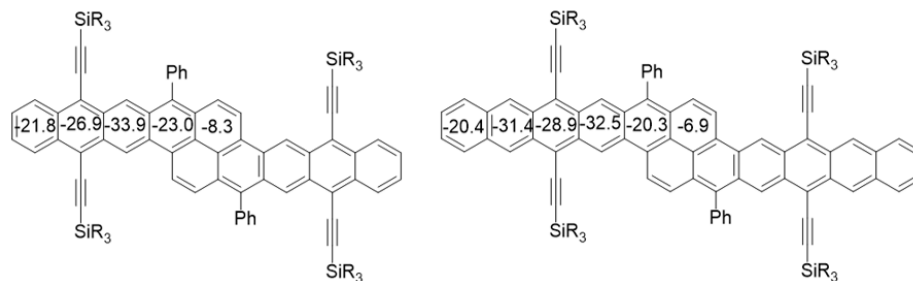


Figure 3:12: NICS values for bispentacene and bishexacene.

3.5: Tuning Solid-State Packing Through Alkylsilylethyne Substituents

For these acenoacenes to find use in OFET applications, their packing motifs should feature ample π -stacking to allow for efficient charge transport. The full packing structures for **NODIPS-BP** and **NODIPS-BH** are shown in Figure 3.12. While the octyl chains on the NODIPS groups enhanced the solubility of the bisacenes to allow for characterization in common organic solvents, these bulky side groups also hindered π -stacking between the aromatic cores. In both cases, the packing is driven primarily by C-H- π interactions between the long alkyl chains and the aromatic backbones, resulting in herringbone-like motifs. One possible way to diminish such extensive C-H- π interactions is to substitute smaller TAS groups onto the acenoacene backbone. **TNPS-BP** and **TNPS-BH**, which feature TNPS substituents, were thus synthesized with the goal of achieving a packing motif with more favorable interactions between the aromatic cores. However, the packing motif of **TNPS-BH** shows only edge-to-face interactions. While C-H- π interactions are also observed in the **TNPS-BH** motif, packing was also disrupted by the presence of solvent with the crystals, which can in part be attributed to large intermolecular space due to the sterically hindering phenyl groups. The synthesis of acenoacenes featuring even smaller TIPS groups was also attempted. Both **TIPS-BP** and **TIPS-BH** were isolated and characterized by MALDI-MS, but the solubility of both products was poor and were thus not characterized further. Future attempts at tuning the crystal packing of BP and BH will likely involve functionalization of the phenyl moieties, with the goal of preventing solvent trapping within the crystal structure.

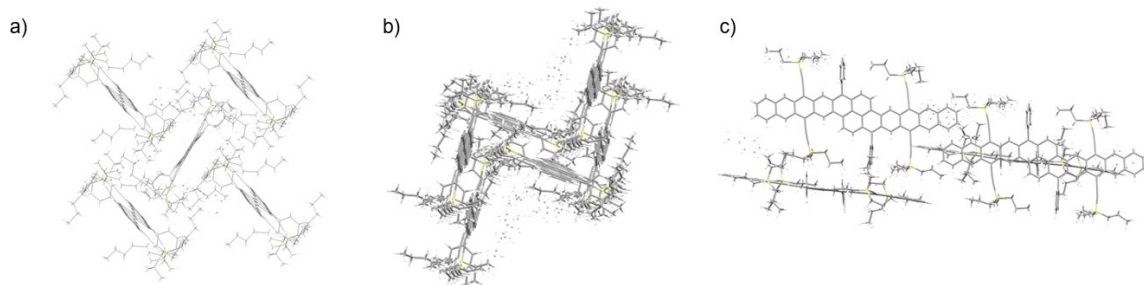


Figure 3:13: Crystal packing structures of a) **NODIPS-BP**, b) **NODIPS-BH**, and c) **TNPS-BH**.

3.6: The Role of Bisacene Functionalization in Preventing Dynamic Disorder

While the phenyl moieties in our class of acenoacenes may present challenges in achieving π -stacking arrangements, it is possible they may play a role in preventing dynamic disorder in the solid-state. As mentioned in section 1.5, the addition of phenyl groups to an acene backbone has been shown to hinder the long-axis sliding motion in materials such as Rubrene, and thus work to mitigate dynamic disorder.⁴² The crystal structures obtained for three of our derivatives confirm that the plane of the phenyl groups lies orthogonal to the acenoacene backbone. To investigate the role of these orthogonal phenyl groups in the long-axis vibrations of acenoacenes, **TNPS-BP** was submitted to collaborators at Oak Ridge National Laboratory to perform inelastic neutron scattering (INS) experiments. INS is well suited to study dynamic disorder in OSCs as it can detect the low-energy vibrations primarily responsible for dynamic disorder, and has been used in the study of a number of high performing OSC materials.^{42,124} **TNPS-BP** was selected for these experiments because the smaller TNPS groups are more ideal substituents for INS than NODIPS, as longer alkyl chains can result in additional vibrational modes and thus more convoluted data.

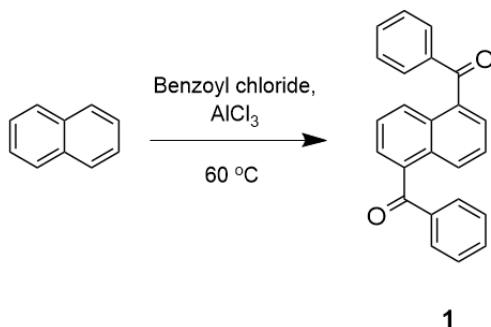
3.7: Summary

This chapter describes the synthesis of a series of acenoacenes utilizing a synthetic route that allows for exquisite control over molecular length. Such a

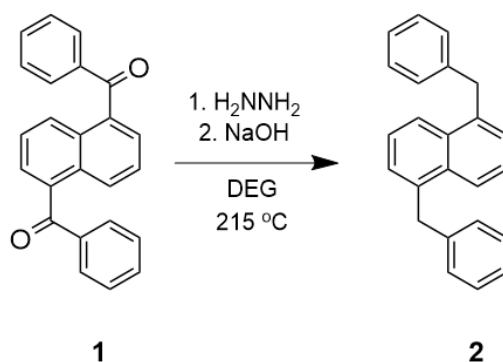
systematic study provides valuable insight into the evolution of electronic properties and stability with increasing molecular length. These acenoacenes also belong to a family of oblique pyrenes, which demonstrate complete conjugation along the aromatic core, in contrast to the disrupted conjugation observed in vertical pyrenes. Absorbance and electrochemical data suggest that linear extension of acenoacenes tunes their electronic structure in a manner similar to that seen in their acene counterparts. While linear acenes become less stable with linear ring extension, **NODIPS-BH** appears slightly more resistant to photooxidation than **NODIPS-BP** upon prolonged light exposure. This counterintuitive trend may be attributed to a low T_1 level in BH that inhibits the generation of 1O_2 via an energy transfer mechanism, and thus substantially slows the rate of photodecomposition. The inability to isolate **NODIPS-BHep** may suggest that acenoacenes of 14-consecutively fused rings or longer do not display the same benefits of stabilization as smaller acenoacenes. More in-depth studies will be necessary to further elucidate the origin of stability observed in acenoacenes. However, the results presented in this chapter prove that the stability of acene-based OSC can be improved while still maintaining valuable acene characteristics.

3.8: Experimental

All reagents and solvents were obtained from Sigma Aldrich, Oakwood Chemicals, Gelest, or VWR and used without further purification. 1H and ^{13}C NMR spectra were measured on a 400 MHz Bruker NMR spectrometer in $CDCl_3$ (7.26 ppm for 1H NMR, 77.16 ppm for ^{13}C NMR). MALDI TOF MS was analyzed on a Bruker Microflex LRF with no matrix. Solution UV-Vis was recorded on an Agilent Carey 60 UV-Vis spectrophotometer. Cyclic voltammetry (CV) measurements were performed in DCM on a BASi Epsilon Potentiostat with a three-electrode cell, using 0.1 M $n-Bu_4NPF_6$ as supporting electrolyte, $AgCl/Ag^+$ as reference electrode, glassy carbon as working electrode, Pt wire as counter electrode, with scan rate at 100 mV/s.

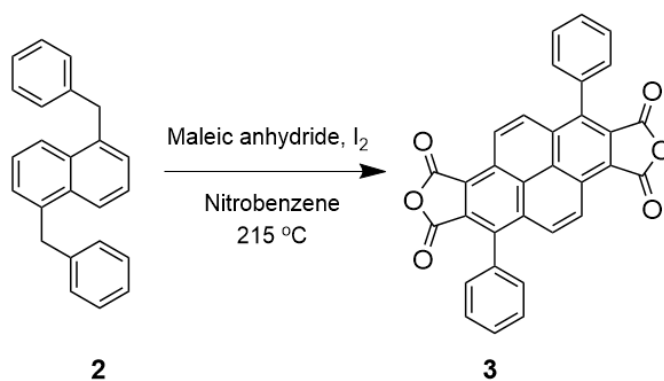


1,5-dibenzoylnaphthalene (1): To a 500 ml RB flask was added aluminum chloride (26.7 g, 200 mmol) and benzoyl chloride (14.5 ml, 120 mmol), and the flask was heated to $80\text{ }^\circ\text{C}$ with stirring until a uniform melt was formed. The flask was allowed to cool to $60\text{ }^\circ\text{C}$, and naphthalene was added in 1.60 g portions every 1 hr (6.40 g, 50.0 mmol total). The melt then seized up, indicating completion of the reaction. The mixture was allowed to cool to room temperature, and was carefully quenched with a saturated solution of ammonium chloride in 10% HCl (100 ml). The mixture was then extracted into DCM (150 ml), and the organic layer was dried with magnesium sulfate, filtered through a thin pad of silica, and flushed with DCM to remove all product. After removal of the solvent, the crude product was triturated with acetone (200 ml), and after vacuum filtration the product was collected as an off-white powder. Yield: 8.44 g, 50%.¹²⁵

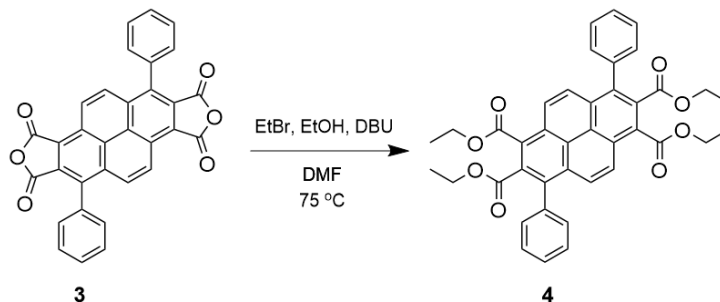


1,5-dibenzyl-naphthalene (2): To a 250 ml RB flask was added diethylene glycol (120 ml), 1,5-dibenzoylnaphthalene (9.00 g, 26.8 mmol), and 80% hydrazine hydrate (7.00 ml). The flask was loosely tented with aluminum foil, and the mixture was stirred at $120\text{ }^\circ\text{C}$ for 1 hour to remove water. The mixture was then

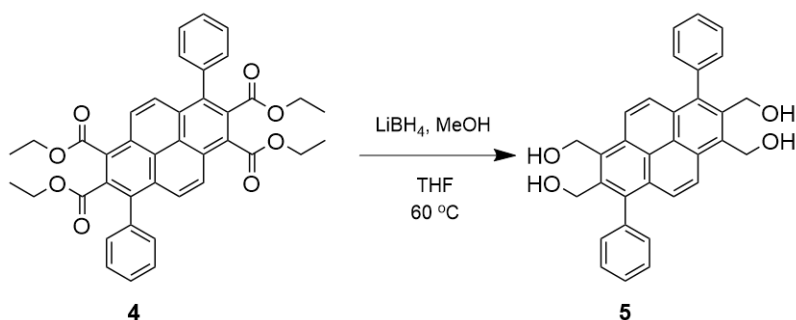
heated to 215 °C and stirred for 3 hours. The flask was then allowed to cool to 100 °C, at which point sodium hydroxide (4.80 g, 120 mmol) was added slowly. The mixture was again stirred at 215 °C for 3 hours. After cooling to room temperature, the mixture was poured into 1 L of water and then filtered to give a light brown solid. The crude product was purified by silica plug in 4:1 hexanes:DCM to give the product as a white solid. Yield: 6.12 g, 74%.¹²⁵



1,6-Diphenylpyrene-2,3,7,8-tetracarboxylic dianhydride (3): To a 100 ml RB flask was added maleic anhydride (24.0 g, 245 mmol) and nitrobenzene (25.0 ml), and the flask was loosely tented with aluminum foil and stirred at 120 °C for 1 hour to remove water. **2** (4.50 g, 14.6 mmol) and iodine (50 mg) were then added, the flask was outfitted with a condenser, and the mixture was heated at 215 °C for 4 hours. After the flask was allowed to cool to room temperature, acetic acid (30 ml) was added to the mixture. The mixture was allowed to stand for 16 hours, at which point a brown crystalline solid was collected by vacuum filtration. The crude solid was triturated with diethyl ether (50 ml) and filtered to yield the product as a light brown solid. Yield: 4.48 g, 62%.¹²⁵

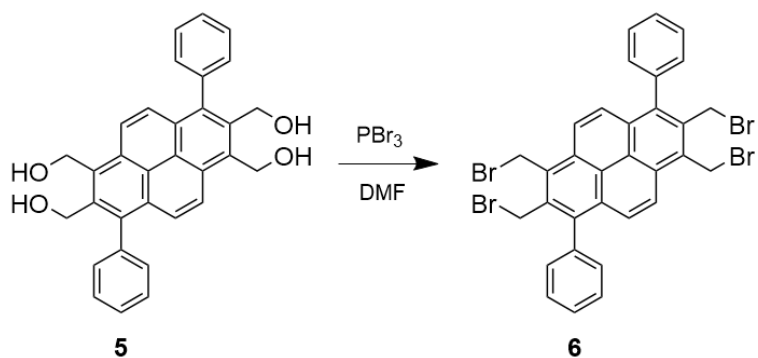


1,6-Diphenylpyrene-2,3,7,8-tetraethylester (4): A 250 ml RB flask was charged with **3** (4.50 g, 9.11 mmol), bromoethane (19.8 g, 182 mmol, 20 eq.), ethanol (15.9 ml, 273 mmol, 30 eq.), DBU (13.6 ml, 91.1 mmol, 10 eq.), and DMF (70 ml). The flask was outfitted with a condenser, and the mixture was stirred at 75 °C for 16 hours. The mixture was poured into water (200 ml), extracted into ethyl acetate, and washed again with water (100 ml). The organic layer was dried with magnesium sulfate, and then flushed through a silica plug (ethyl acetate). The solvent was removed to give the product as a yellow solid. Yield: 5.44 g, 93%. m.p. 295 °C. ¹H NMR (400 MHz, CDCl₃): δ 8.49 (d, *J* = 9.6 Hz, 2H), 8.01 (d, *J* = 9.6 Hz, 2H), 7.55 (m, 6H), 7.49 (m, 4H), 4.52 (q, *J* = 7.2 Hz, 4H), 4.06 (q, *J* = 7.2 Hz, 4H), 1.44 (t, *J* = 7.2 Hz, 6H), 0.98 (t, *J* = 7.2 Hz, 6H). ¹³C NMR (101 MHz, CDCl₃): 168.47, 167.74, 137.66, 136.43, 132.37, 131.07, 130.60, 128.14, 127.51, 126.70, 126.35, 124.47, 62.26, 61.57, 14.10, 13.58. HRMS (TOF MS ESI⁻) for [M]⁻: calc. for C₄₀H₃₄O₈: 642.2254, found: 642.2247.

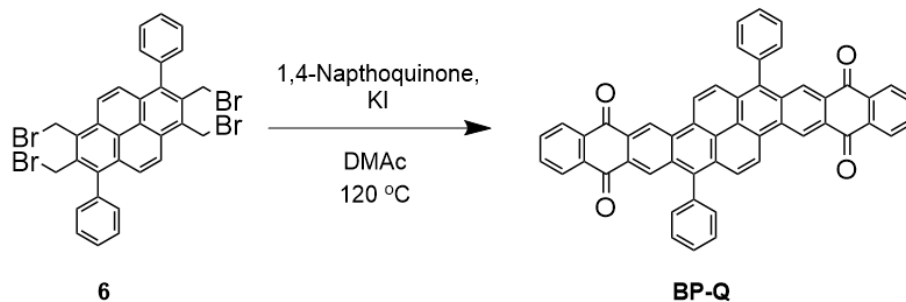


1,6-Diphenylpyrene-2,3,7,8-tetramethanol (5): A flame-dried 250 ml RB flask under N₂ was charged with **4** (4.00 g, 6.23 mmol), anhydrous THF (40 ml), and

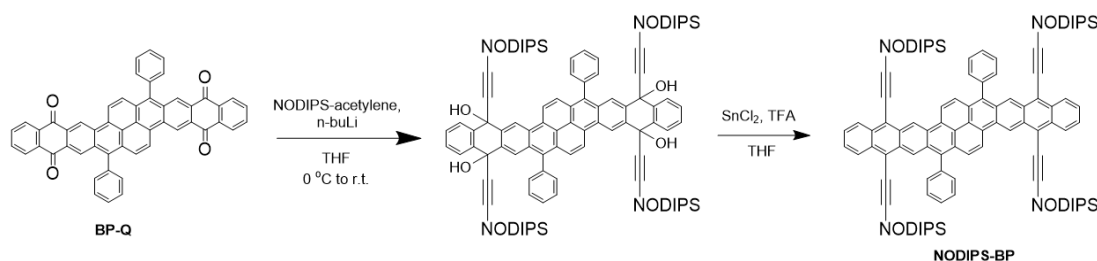
methanol (4.03 ml, 99.8 mmol, 16 eq.). 4M lithium borohydride in THF (24.9 ml, 99.8 mmol, 16 eq.) was added slowly at room temperature, and the mixture was then heated to 60 °C and stirred for 16 hours. The flask was allowed to cool to room temperature, at which point the mixture was quenched with dropwise additions of water (10 ml) and 10% HCl (10 ml) until foaming ceased. The mixture was then poured into 100 ml of water and then filtered. The crude product was taken up in acetone (150 ml), triturated, and then filtered to give the product as a pale-yellow powder. The crude product was taken to the next step without further purification. Yield: 2.40 g, 81%. MS (MALDI TOF) calc. for $C_{32}H_{22}O_4$: 474.183 $[M]^+$, found: 474.264.



1,6-Diphenylpyrene-2,3,7,8-tetramethylbromide (6): To a 250 ml flame-dried RB flask under N_2 was added anhydrous DMF (40 ml) and **5** (2.40 g, 5.05 mmol). 1M PBr_3 (30.3 ml, 30.3 mmol, 6 eq.) in DCM was then added, and the mixture was stirred for 14 hours, during which time a precipitate formed. The reaction was quenched slowly with water (20 ml) and 10% HCl (20 ml), and the mixture was then poured in 100 ml MeOH, triturated, and then filtered. The filtrate was then taken up in acetone, triturated, and then filtered, and the product was recovered as a yellow solid. The crude product was taken to the next step without further purification. Yield: 2.70 g, 77%. MS (MALDI TOF) calc. for $C_{32}H_{22}Br_3^+$: 642.927 $[M-Br]^+$, found: 642.822.

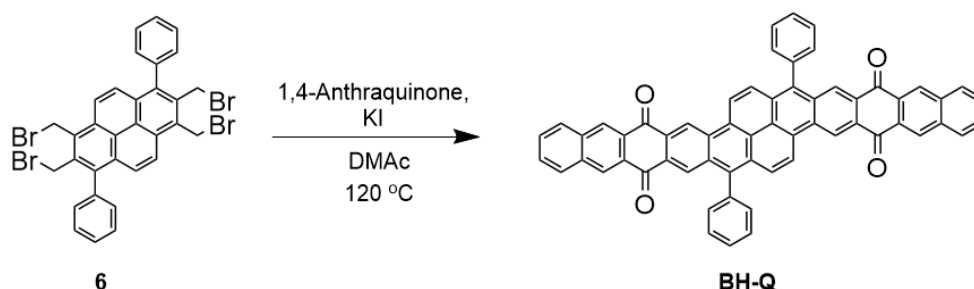


Diphenylbispentacenequinone (BP-Q): A 150 ml sealed tube reactor was charged with N,N-dimethylacetamide (50 ml), **6** (1.00 g, 1.38 mmol), 1,4-naphthoquinone (0.872 g, 5.52 mmol, 4 eq.), and potassium iodide (1.74 g, 10.5 mmol, 8 eq.). The tube was sealed, and the mixture was then stirred at 120 °C for 2 days. The tube was allowed to cool to room temperature, unsealed, and the mixture was stirred open to air for 2 hours. The mixture was then poured into 500 ml of water and filtered. The crude filtrate was taken up in 250 ml acetone, sonicated for 10 minutes, and then filtered. The filtrate was then added to 250 ml THF, sonicated for 10 minutes, and then filtered. The crude product was collected as a black solid and was used without further purification. Yield: 0.611 g, 64%.



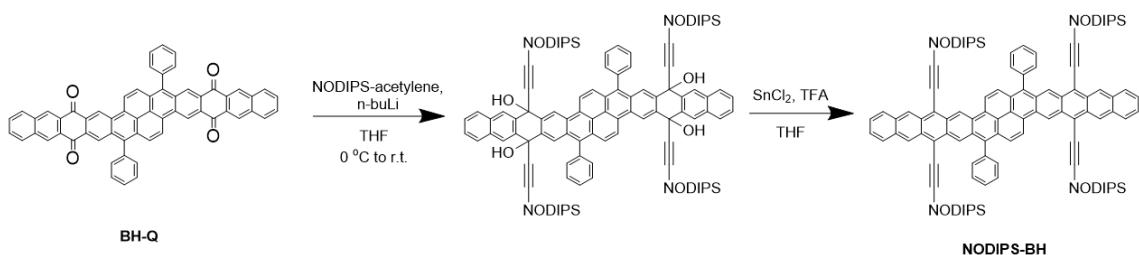
NODIPS-BP: A flame-dried 100 ml RB flask under N₂ was charged with 20 ml anhydrous THF and NODIPS-acetylene (1.37 g, 5.40 mmol, 13 eq.). The flask was cooled to 0 °C, and then 2.5 M n-butyllithium in hexanes (1.99 ml, 4.98 mmol, 12 eq.) was added slowly and the mixture was stirred for 30 minutes. **BP-Q** (0.300 g, 0.415 mmol) was then added, and the mixture was stirred for 16 hours. The reaction was quenched with water (20 ml) and 10% HCl (5 ml), and

the organic layer was extracted into diethyl ether, dried with magnesium sulfate, and the solvent removed. The crude, viscous oil was purified on a silica plug in 5:1 hexanes:ethyl acetate to give a red oil, which was carried directly to the next step. The oil was dissolved in THF (20 ml) and added to a 100 ml RB flask along with 0.750 g tin (II) chloride hydrate and 2 ml trifluoroacetic acid, and the mixture was stirred for 30 minutes. The reaction was quenched with water (20 ml) and the organic layer was extracted into diethyl ether, dried with magnesium sulfate, and the solvent removed. The crude product was purified by column chromatography in 6:1 hexanes:DCM to give the product as a dark green solid. Yield: 0.24 g, 34%. ^1H NMR (400 MHz, CDCl_3): δ 10.94 (s, 2H), 9.39 (s, 2H), 9.05 (d, $J = 10$ Hz, 2H), 8.66 (dd, $J = 10.4, 7.6$ Hz, 4H), 7.90 (d, $J = 9.6$ Hz, 2H), 7.68 (m, 10H), 7.54 (m, 4H), 1.75 (q, $J = 7.6$ Hz, 8H), 1.46 (p, $J = 7.6$ Hz, 8H), 1.36 (m, 48H), 1.29 (m, 8H), 1.23 (m, 8H), 1.16 (m, 16H), 0.98 (t, $J = 7.6$ Hz, 8H), 0.84 (t, $J = 6.8$ Hz, 8H), 0.77 (m, 8H). ^{13}C NMR (101 MHz, CDCl_3): 139.09, 136.64, 133.14, 132.81, 131.62, 130.38, 129.64, 129.55, 128.78, 127.91, 127.66, 127.57, 127.52, 127.29, 126.69, 126.46, 125.04, 123.03, 122.23, 118.66, 118.62, 106.80, 106.59, 104.06, 103.27, 34.01, 31.95, 29.40, 24.69, 22.67, 18.76, 18.43, 14.09, 12.13, 10.20. HRMS (TOF MS ESI $^-$) calc. for $\text{C}_{116}\text{H}_{150}\text{Si}_4$: 1655.0815 [M] $^-$, found: 1655.0704.



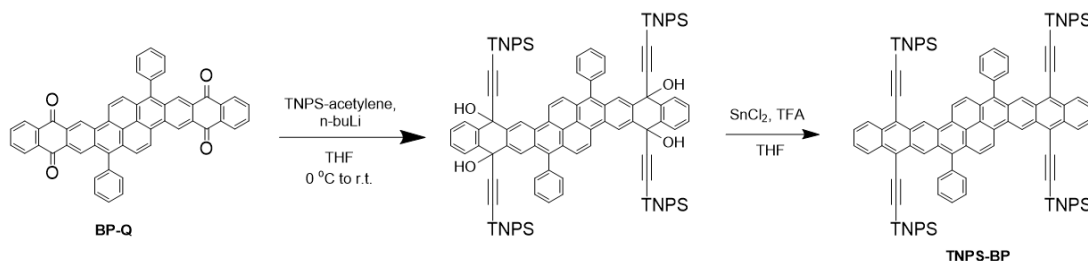
Diphenylbishexacenequinone (BH-Q): A 150 ml sealed tube reactor was charged with **6** (1.00 g, 1.38 mmol), 1,4-anthraquinone (1.14 g, 5.52 mmol), potassium iodide (1.83 g, 11.0 mmol), and N,N-dimethylacetamide (50 ml) and the tube was sealed. The mixture was then stirred at 120 °C for 2 days. The tube was allowed to cool to room temperature, unsealed, and the mixture was allowed

to stir open to air for 2 hours. The mixture was then poured into 500 ml of water and filtered. The crude filtrate was taken up in 250 ml acetone, sonicated for 10 minutes, and then filtered. The filtrate was then added to 250 ml THF, sonicated for 10 minutes, and then filtered. The crude product was collected as a black solid and was used without further purification. Yield: 0.58 g, 51%.

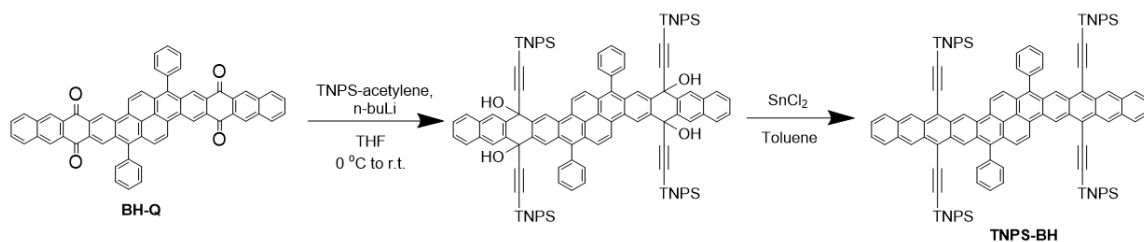


NODIPS-BH: A flame-dried 50 ml RB flask under N₂ was charged with 8 ml anhydrous THF and NODIPS-acetylene (0.612 g, 2.42 mmol, 20 eq.). The flask was cooled to 0 °C, and then 1 M LiHMDS (2.30 ml, 2.30 mmol, 19 eq.) was added slowly and the mixture was stirred for 30 minutes. **BH-Q** (0.100 g, 0.121 mmol) was then added, and the mixture was stirred for 16 hours. The reaction was quenched with water (10 ml) and the organic layer was extracted into diethyl ether (50 ml), dried with magnesium sulfate, and the solvent removed. The crude, viscous oil was purified on a silica plug in 7:1 hexanes:ethyl acetate to give a red oil, which was carried directly to the next step. The oil was dissolved in toluene (25 ml) and added to a 100 ml RB flask along with 0.16 g tin (II) chloride hydrate, and the mixture was stirred for 1 hour. The reaction was quenched with water (50 ml) and the organic layer was extracted into diethyl ether (50 ml), dried with magnesium sulfate, and the solvent removed. The crude product was purified by column chromatography in 6:1 hexanes:DCM to give the product as a dark purple solid. Yield: 23 mg, 15%. ¹H NMR (400 MHz, CDCl₃): δ 10.44 (s, 2H), 9.37 (s, 2H), 9.34 (s, 2H), 8.97 (d, *J* = 10 Hz, 2H), 7.99 (dd, *J* = 6.4, 5.2 Hz, 4H), 7.84 (d, *J* = 10 Hz, 2H), 7.75 (m, 10H), 7.44 (m, 4H), 1.39 (m, 24H), 1.22 (m, 40H), 1.85 (p, *J* = 8 Hz, 8H), 1.63 (m, 8H), 1.51 (m, 16H), 1.04 (m, 8H), 0.83 (m,

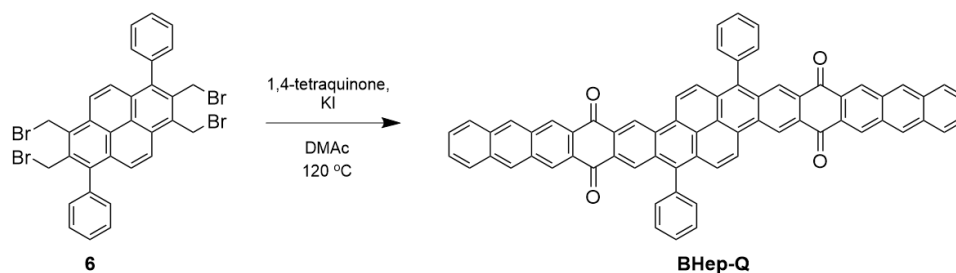
16H). HRMS (TOF MS ESI-) calc. for $C_{124}H_{154}Si_4$: 1755.1128 [M]⁻, found: 1755.1025.



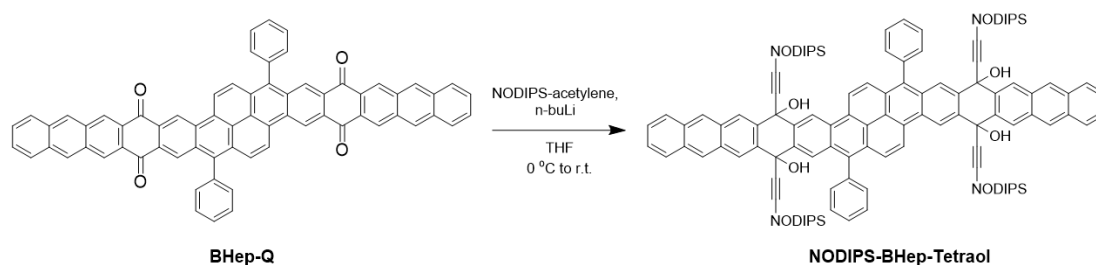
TNPS-BP: A flame-dried 100 ml RB flask under N₂ was charged with 20 ml anhydrous THF and TNPS-acetylene (1.76 g, 9.66 mmol, 14 eq.). The flask was cooled to 0 °C, and then 2.5 M n-butyllithium in hexanes (3.32 ml, 8.30 mmol, 12 eq.) was added slowly and the mixture was stirred for 30 minutes. **BP-Q** (0.500 g, 0.692 mmol) was then added, and the mixture was stirred for 16 hours. The reaction was quenched with water (20 ml) and the organic layer was extracted into diethyl ether (50 ml), dried with magnesium sulfate, and the solvent removed. The crude, viscous oil was purified on a silica plug in 5:1 hexanes:ethyl acetate to give a red oil, which was carried directly to the next step. The oil was dissolved in THF and added to a 100 ml RB flask along with 0.90 g tin (II) chloride hydrate and 2 ml trifluoroacetic acid, and the mixture was stirred for 30 minutes. The reaction was quenched with water (20 ml) and the organic layer was extracted into ether (50 ml), dried with magnesium sulfate, and the solvent removed. The crude product was purified by column chromatography in 6:1 hexanes:DCM to give the product as a dark green solid. Yield: 191 mg, 21%. ¹H NMR (400 MHz, CDCl₃): δ 10.45 (s, 2H), 9.37 (s, 2H), 9.05 (d, *J* = 10 Hz, 2H), 8.60 (dd, *J* = 15.6, 7.2 Hz, 4H), 7.96 (d, *J* = 7.96 Hz, 2H), 7.70 (m, 10H), 7.57 (m, 4H), 1.77 (m, 12H), 1.55 (m, 12H), 1.14, (p, *J* = 7.2 Hz, 36H), 1.02 (m, 12H), 0.78 (m, 12H). MS (MALDI TOF) calc. for $C_{96}H_{110}Si_4$: 1374.768 [M]⁺, found: 1374.458.



TNPS-BH: A flame-dried 100 ml RB flask under N_2 was charged with 12 ml anhydrous THF and TNPS-acetylene (1.85 g, 10.2 mmol, 20 eq.). The flask was cooled to 0 °C, and then 1 M LiHMDS (2.30 ml, 2.30 mmol, 19 eq.) was added slowly and the mixture was stirred for 30 minutes. **BH-Q** (0.420 g, 0.508 mmol) was then added, and the mixture was stirred for 16 hours. The reaction was quenched with water (20 ml) and the organic layer was extracted into diethyl ether (50 ml), dried with magnesium sulfate, and the solvent removed. The crude, viscous oil was purified on a silica plug in 7:1 hexanes:ethyl acetate to give a red oil, which was carried directly to the next step. The oil was dissolved in toluene (50 ml) and added to a 100 ml RB flask along with 0.675 g tin (II) chloride hydrate, and the mixture was stirred for 1 hour. The reaction was quenched with water (50 ml) and the organic layer was extracted into diethyl ether (50 ml), dried with magnesium sulfate, and the solvent removed. The crude product was purified by column chromatography in 6:1 hexanes:DCM to give the product as a dark purple solid. Yield: 42 mg, 5.5%. $^1\text{H NMR}$ (400 MHz, CDCl_3): δ 10.39 (s, 2H), 9.29 (s, 2H), 9.24 (s, 2H), 8.96 (d, $J = 9.6$ Hz, 2H), 7.97 (m, 6H), 7.77 (m, 10H), 7.45 (m, 4H), 1.83 (m, 12H), 1.62 (m, 12H), 1.17 (m, 36H), 1.06 (m, 12H), 0.84 (m, 12H). MS (MALDI TOF) calc. for $\text{C}_{104}\text{H}_{114}\text{Si}_4$: 1474.800 $[\text{M}]^+$, found: 1474.476.



Diphenylbisheptacenequinone (BHep-Q): A 150 ml sealed-tube reactor was charged with **6** (0.600 g, 0.825 mmol), 1,4-tetraquinone (0.639 g, 2.48 mmol, 3 eq.), potassium iodide (1.10 g, 6.6 mmol, 8 eq.), and N,N-dimethylacetamide (30 ml), and the tube was sealed. The mixture was then stirred at 120 °C for 2 days. The tube was allowed to cool to room temperature, unsealed, and allowed to stir open to air for 2 hours. The mixture was then poured into 500 ml of water and filtered. The crude filtrate was taken up in 250 ml acetone, sonicated for 10 minutes, and then filtered. The filtrate was then added to 250 ml THF, sonicated for 10 minutes, and then filtered. The crude product was collected as a black solid and was used without further purification. Yield: 0.55 g, 73%.



NODIPS-BHep-Tetraol: A flame-dried 100 ml RB flask under N₂ was charged with 20 ml anhydrous THF and NODIPS-acetylene (2.20 g, 8.74 mmol, 16 eq.). The flask was cooled to 0 °C, and then 2.5 M n-butyllithium in hexanes (3.28 ml, 8.19 mmol, 15 eq.) was added slowly and the mixture was stirred for 30 minutes. **BHep-Q** (0.500 g, 0.546 mmol) was then added, and the mixture was stirred for 16 hours. The reaction was quenched with water (20 ml) and the organic layer was extracted into diethyl ether (50 ml), dried with magnesium sulfate, and the

solvent removed. The crude product was purified on a silica plug in 5:1 hexanes:ethyl acetate to give a dark-red viscous oil.

Chapter 4: Towards a Functionalized, Stable Cata-Pentacenopentacene

4.1: Introduction to Cata-annulated Acenoacenes

While a number acenoacenes featuring various peri-annulation modes have been reported, cata-annulated acenoacenes fused at the 1,2-positions of the acene moieties are relatively rare. A cata-anthracenoanthracene was first reported in 1929 by Clar,¹²⁶ and not until recently have longer derivatives been the focus of study. Gourdon recently reported a series of non-functionalized cata-acenoacenes, including a pentacenopentacene (**PP**) and hexacenohexacene.¹²⁷ However, poor solubility and high reactivity of the compounds limited their characterization, and absorbance spectra could only be achieved in a frozen matrix. Bunz reported a TIPS-ethynyl-substituted cata-N-pentacenopentacene that was stable enough to undergo some characterization (¹H NMR, mass spectroscopy, infrared spectroscopy) as well as absorbance studies under ambient conditions, but low yields prevented further study.¹²⁸ These cata-condensed **PP** show red-shifted absorption spectra relative to their linear counterparts, though such redshifts (50-60 nm) appear smaller compared to that observed in **NODIPS-BP** compared to **TIPS-Pen** (>100 nm). This suggests that cata-annulated acenoacenes retain electronic structures that more closely resemble linear acenes than peri-annulated acenoacenes. It should be noted that functionalized cata-annulated **PP** derivatives featuring an all-hydrocarbon aromatic core have not been reported, primarily due to the lack of synthetic accessibility for such a framework. Thus, it is not clear how the stability of such a system would differ from N-substituted derivatives and from peri-annulated acenoacenes, such as the oblique pyrenes discussed in chapter 3.

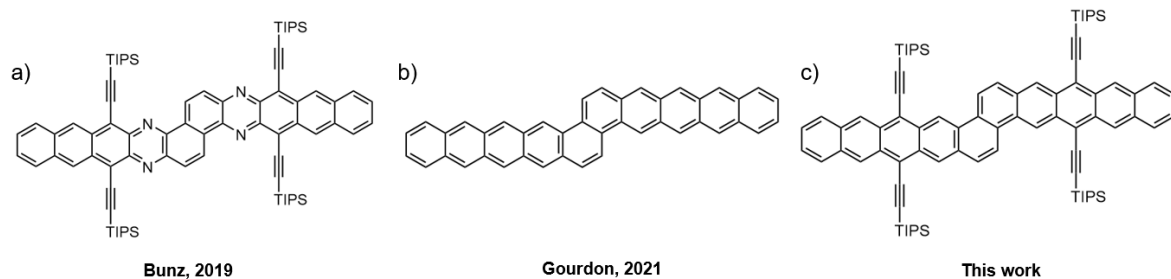


Figure 4:1: Cata-annulated (a) TIPS-substituted N-PP, (b) non-functionalized PP, and (c) TIPS-substituted PP.

This chapter details the synthesis and characterization of a functionalized cata-pentacenopentacene (**c-PP**). Like the fused-acenes discussed in previous chapters, the synthetic route consists of a quinone intermediate that allows for the addition of TAS groups of varying size, which may be used to control solubility as well as solid-state ordering. Considering that silylethynyl groups stabilize acene derivatives, such substituents were hypothesized to stabilize larger cata-acenoacenes so that they may be isolated under ambient conditions. Such stabilization would allow for more in-depth studies to determine how the role of ring annulation impacts its electronic structure relative to peri-annulated acenoacenes. Based on absorption data reported for N-pentacenopentacene and non-substituted **PP** derivatives, it would be expected that the onset absorption of **TIPS-c-PP** would be redshifted relative to **TIPS-Pen**, albeit to a lesser extent than **NODIPS-BP**. Because the decomposition pathways for unsubstituted **c-PP** and cata-hexacenoacene derivatives have not been investigated, photostability studies will also be performed in order to examine how the cata-annulated structure of these derivatives impacts their stability compared to their peri-annulated counterparts.

4.2: Synthesis of TIPS-c-PP

The synthetic route to the **c-PP** backbone involves the synthesis of a di-aryne precursor **2**, which was performed with help from undergraduate researcher Andrew Sturgis. After the bromination of 1,5-dihydroxynaphthalene at the 2 and 6 positions, the next step makes use of a modified 2-step, 1-pot

procedure for the synthesis of ortho-trimethylsilylaryl triflates.¹²⁹ After protection of the alcohols with trimethylsilyl (TMS) groups using hexamethyldisilazane (HMDS), the crude intermediate is then subjected to metal-halogen exchange at low temperature, which results in migration of the TMS group to the 2 and 6 positions in what is known as a Brook rearrangement. Quenching the reaction with triflic anhydride (Tf₂O) yields the naphthdiyne precursor **2**. Treatment of **2** with tetrabutylammonium fluoride (TBAF) causes the generation of the aryne intermediate, which promptly undergoes a Diels-Alder reaction with furan to form naphthalene-diendoxide **3**. The poor solubility of **3** prevented characterization by NMR, however its structure was confirmed by X-ray crystallography. While the crystal structure appears to show only the anti-conformation of the endoxide, TLC of the crude product prior to work-up appears to show spots consistent with both the anti and cis isomers, as both products show the same mass by MALDI-MS. However, the anti-conformation is significantly less soluble than the cis-isomer, and can thus be easily filtered off from the reaction mixture.

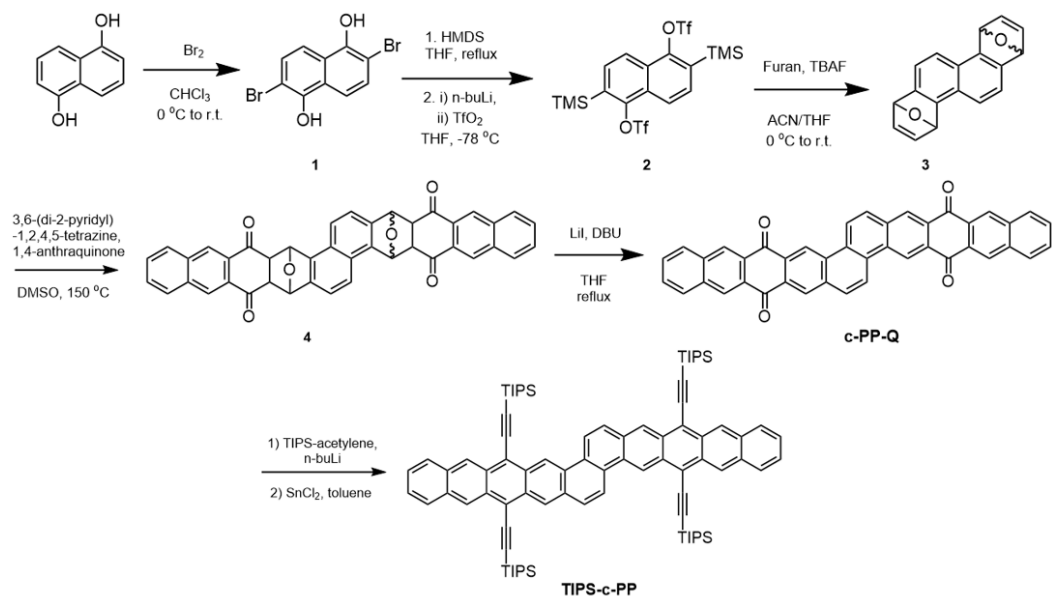


Figure 4:2: Synthetic route to **TIPS-c-PP**.

To extend the length of the fused-acene core, the addition of 1,4-anthraquinone to **3** was facilitated by 3,6-(di-2-pyridyl)-1,2,4,5-tetrazine. The poor

solubility of the starting materials and reaction intermediates impeded early attempts at the synthesis of **4**. The use of chloroform or o-dichlorobenzene as the solvent gave a pink, insoluble precipitate as the product, which could not be characterized. The starting materials could be completely dissolved in a dilute DMF solution, and upon stirring at room temperature the pink precipitate was formed. Heating the mixture at 140 °C resulted in solvation of the intermediate, which promptly turned dark and resulted in a poorly soluble brown solid which could not be characterized. The attempted addition of TIPS-acetylide did not result in change to the starting material by TLC, suggesting that this material was not the desired quinone and could be a decomposition product. The optimal reaction conditions ultimately utilized DMSO as the solvent, with the crude product subjected to lithium iodide at reflux to give **c-PP-Q**.³⁵ While the poor solubility **c-PP-Q** prevented its characterization, the addition of TIPS-acetylide followed by deoxygenation with tin (II) chloride provided **TIPS-c-PP**. The low yields (<5%) of **TIPS-c-PP** are primarily due to the presence of impurities in **c-PP-Q**, which hinders efficient addition of TIPS-acetylide to the quinone. **TIPS-c-PP** was able to be isolated under ambient conditions and could be characterized by ¹H NMR (Figure 4.3), which shows the fully aromatic product without any peaks corresponding to common degradation products such as endoperoxides or dimers.

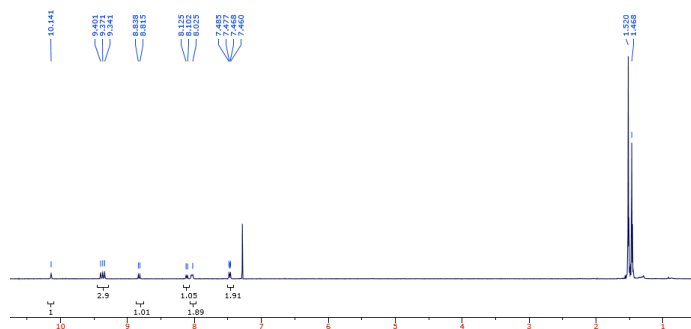


Figure 4.3: ¹H NMR spectrum of **TIPS-c-PP**.

4.3: Absorption Properties and Stability of TIPS-c-PP

The UV-Vis spectrum of **TIPS-c-PP** shows an onset absorbance peak at 685 nm, and features a similar acene-like vibronic progression to that seen in **NODIPS-BP** and **NODIPS-BH**. A second vibronic progression is observed between 425 nm and 500 nm, which may indicate that lower-lying molecular orbitals, such as the HOMO-1, also maintain an acene-like electronic structure. The onset absorbance of **TIPS-c-PP** is redshifted by ~60 nm compared to the unsubstituted pentacenopentacene reported by Gourdon, which is similar to the redshift observed in **TIPS-Pen** relative to pentacene.⁸² Notably, **TIPS-c-PP** displays a relatively small redshift in absorbance compared to **TIPS-Pen** (~35 nm), and is blueshifted by ~80 nm relative to **NODIPS-BP**. Thus, the electronic structure of the **c-PP** framework appears more reminiscent of pentacene than a 2-D fused-pentacene system. Further experimental characterization, as well as computational studies, will be necessary to fully elucidate the electronic properties of **c-PP** derivatives.

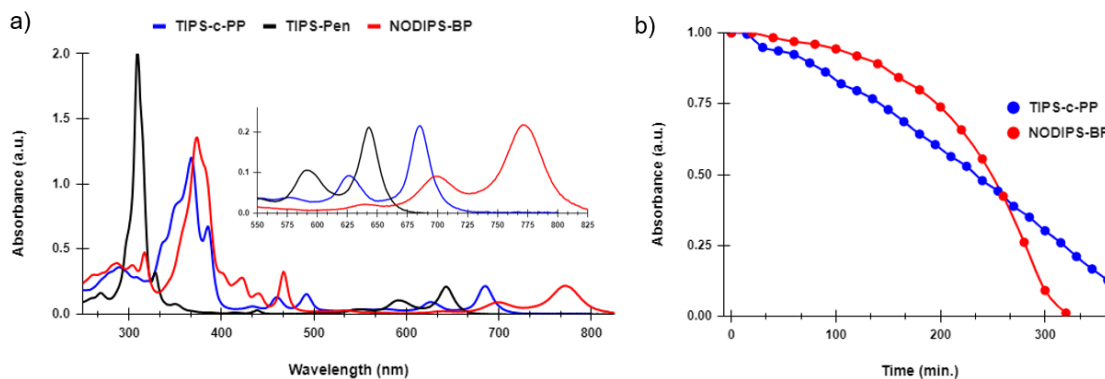


Figure 4:4: (a) UV-Vis spectrum of **TIPS-c-PP**, **NODIPS-BP**, and **TIPS-Pen**, (b) stability studies for **TIPS-c-PP** and **NODIPS-BP** in chloroform under white light exposure.

To gauge the photostability of **TIPS-c-PP**, stability experiments were performed under exposure to an intense white-light source. While the unsubstituted **PP** reported by Gourdon could not be isolated outside of frozen matrices due to insolubility and high reactivity,¹²⁷ **TIPS-c-PP** decomposes only slowly in solution under prolonged light exposure, and remains stable in the dark

indefinitely both in solution and in the solid-state. Such stability can be attributed to the ability of the TIPS-ethynyl substituents to slow the rate of photooxidation and hinder dimerization through steric effects. Additionally, **TIPS-c-PP** displays a half-life similar to that of **NODIPS-BP** under similar conditions. The linear degradation rate for **TIPS-c-PP** shown in Figure 4.4 suggests that the decomposition products generated upon light exposure do not noticeably catalyze the further decay of **TIPS-c-PP**, which may play a role in its photostability. The significantly enhanced photostability of **TIPS-c-PP** compared to **TIPS-Pen** is particularly surprising given the apparent similarities in their electronic structures, and further demonstrates that the 2-D framework of acenoacenes provides a stabilizing effect on acene derivatives.

4.4: Crystal Packing in TIPS-c-PP

The crystal structure for **TIPS-c-PP** is shown in Figure 4.5. In contrast to the peri-annulated acenoacenes discussed in Chapter 3, **TIPS-c-PP** displays strong 1-D π -stacking. **TIPS-c-PP** also displays strong electronic coupling (88 meV) along its strong axis, which can be attributed in part to its large, planar π -surface that allows for significant intermolecular orbital overlap. However, the rather poor solubility of **TIPS-c-PP** could potentially inhibit its ability to form quality thin-films for transistor applications. Therefore, future attempts at tuning c-PP derivatives for OFET applications will involve tuning the size of the TAS-ethyne groups to improve processability while still maintaining π -stacking.

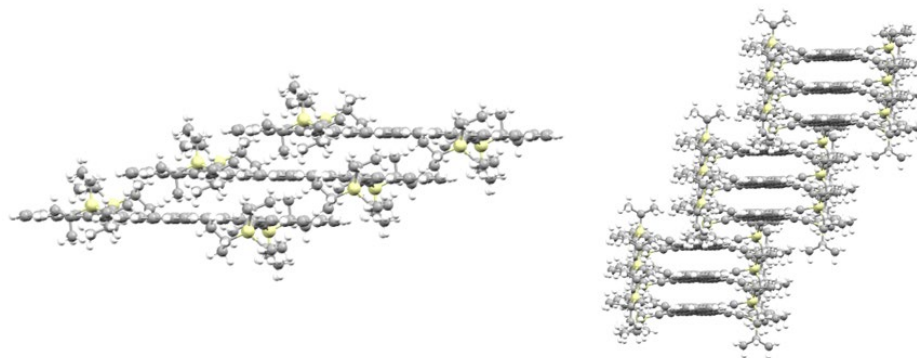


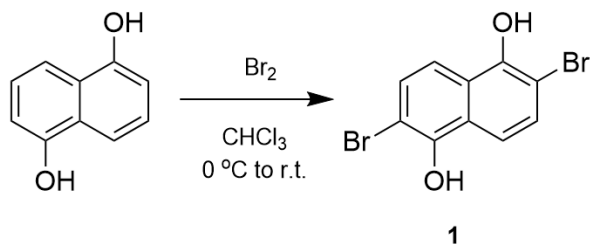
Figure 4:5: Crystal structure of TIPS-c-PP.

4.5: Conclusion

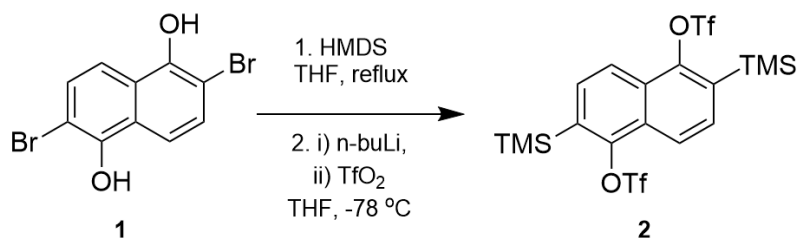
This chapter describes the synthesis of a functionalized pentacenopentacene derivative featuring a cata-condensed aromatic core. The incorporation of TIPS-ethynyl substituents onto the **PP** backbone drastically improves the stability of the acenoacene core compared to previously reported non-functionalized acenoacenes of similar size and annulation mode. UV-Vis studies show that the optical properties of **TIPS-c-PP** are more reminiscent of **TIPS-Pen** than other fused-acene systems such as oblique pyrenes. **TIPS-c-PP** displays enhanced photostability compared to **TIPS-Pen**, providing another unique system with which to study the stability of extended fused-acene derivatives. Similar to the synthetic protocols described in previous chapters, the synthetic route to **TIPS-c-PP** allows for straightforward tuning of molecular length, which will allow for future studies on the stability of larger cata-annulated acenoacenes.

4.6: Experimental

All reagents and solvents were obtained from Sigma Aldrich, Oakwood Chemicals, Gelest, or VWR and used without further purification. Solution UV-vis was recorded on an Agilent Carey 60 UV-Vis spectrophotometer. ^1H and ^{13}C NMR spectra were measured on a 400 MHz Bruker NMR spectrometer in CDCl_3 (7.26 ppm for ^1H NMR, 77.16 ppm for ^{13}C NMR).

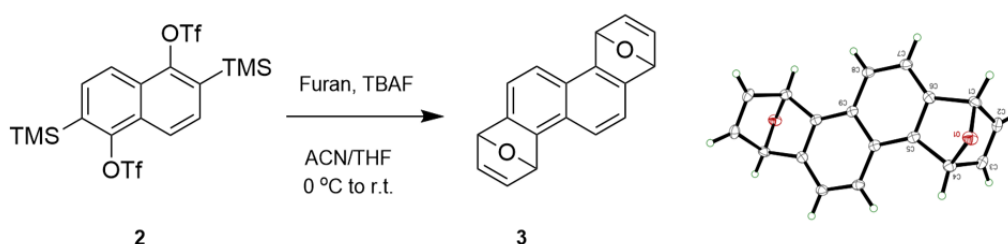


2,6-Dibromo-1,5-dihydroxynaphthalene: A 500 ml RB flask was charged with 1,5-dihydroxynaphthalene (10.0 g, 62.4 mmol) and 200 ml chloroform, and the suspension was cooled to 0 °C. A solution of bromine (20.0 g, 125 mmol, 2 eq.) in 15 ml chloroform was then added dropwise, and the mixture was stirred at room temperature for 18 hours. The solid product was filtered, and the filtrate was washed with 50 ml chloroform and dried under vacuum. The crude solid was purified via silica plug in DCM to give the product as a beige powder. Yield: 13.1 g, 66%.

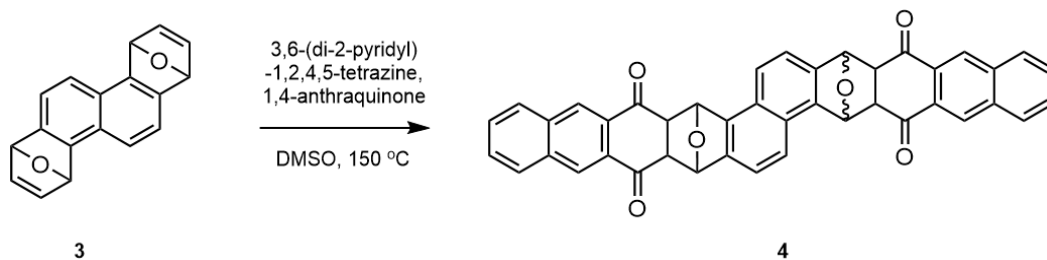


2,6-bis(trimethylsilyl)-1,5-bis(trifluoromethanesulfonyl)naphthalene (2): A 250 ml round-bottom flask was charged with **1** (4.00 g, 12.6 mmol), HMDS (7.90 ml, 37.3 mmol, 3 eq.), and 50 ml THF. The flask was fitted with a condenser, and the mixture was stirred at reflux for 2 hour. The flask was then allowed to cool to room temperature, and the solvent and excess HMDS were removed. The solid was then re-dissolved in anhydrous THF (84 ml), and the solution was cooled to -78 °C. 2.5 M n-butyllithium in hexanes (11.6 ml, 29.0 mmol, 2.3 eq.) was added dropwise, and the mixture was stirred for 30 minutes at -78 °C. Then, trifluoromethanesulfonyl anhydride (5.29 ml, 31.5 mmol, 2.5 eq.) was added slowly, and the solution was allowed to stir for an additional 30 minutes. A

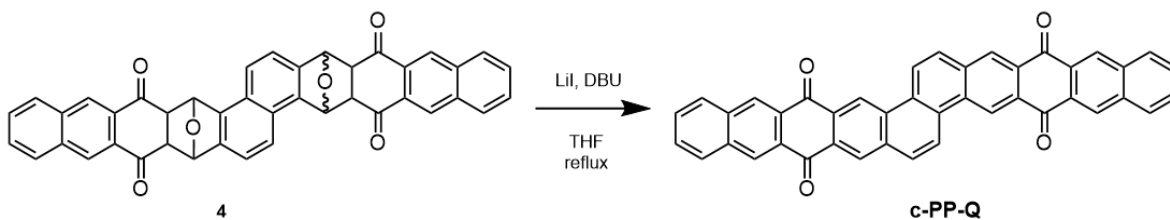
saturated solution of aqueous sodium bicarbonate (50 ml) was added slowly, and the mixture was allowed to warm to room temperature. The mixture was extracted into ether and washed with water, the organic layer was dried with magnesium sulfate, and the solvent was removed. The crude product was purified by silica plug in 6:1 hexanes:DCM to give the product as a white solid.¹²⁹ Yield: 4.21 g, 63%. ¹H NMR (400 MHz, CDCl₃): δ 8.08 (d, *J* = 8.4 Hz, 2H), 7.73 (d, *J* = 8.8 Hz, 2H), 0.50 (s, 18H). ¹³C NMR (101 MHz, CDCl₃): δ 147.85, 133.87, 132.53, 128.98, 123.46, 121.54, 120.28, 117.09, 113.91, 0.12.



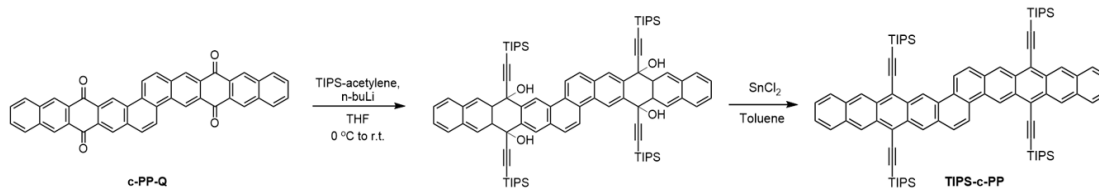
1,4,7,10-tetrahydro-1,4,7,10-diepoxychrysene (3): A flame-dried 100 ml RB flask under N₂ was charged with **2** (1.00 g, 1.87 mmol), furan (1.30 ml, 17.9 mmol, 10 eq.), 12 ml acetonitrile, and 4 ml anhydrous THF. The flask was cooled to 0 °C, a 1M tetrabutylammonium fluoride solution in THF (7.48 ml, 7.48 mmol, 4 eq.), was added, and the mixture was allowed to stir at room temperature for 14 hours, during which time a precipitate formed. Then, 20 ml water was added, and the mixture was filtered. The off-white filtrate was triturated in 100 ml acetone and filtered to give the product as a white solid. The product was recrystallized from DMF. MALDI-MS for [M+1]⁺: calc. For C₁₈H₁₂O₂: 260.084, found: 260.155. Yield: 0.24 g, 50 %.



PP-diendoxidequinone (4): A 100 ml RB flask was charged with 50 ml DMSO, and the solvent was purged with N₂ for 30 minutes. Then, **3** (0.250 g, 0.962 mmol), 3,6-(di-2-pyridyl)-1,2,4,5-tetrazine (0.569 g, 2.41 mmol, 2.5 eq.), and 1,4-anthraquinone (0.801 g, 3.85 mmol, 4 eq.) were all added, and the mixture was stirred at 150 °C for 16 hours. The mixture was allowed to cool to room temperature, and was then poured into 250 ml water and filtered. The filtrate was then taken up in 100 ml acetone, triturated and then filtered. The filtrate was then taken up in 100 ml THF, triturated, and filtered to give the crude product as a brown solid, which was taken to the next step without further purification.³⁵ Yield: 0.423 g, 70%.



c-PP-Q: A 250 ml RB flask was charged with **4** (0.400 g, 0.641 mmol), lithium iodide (0.214 g, 1.60 mmol, 2.5 eq.), DBU (1.95 g, 12.8 mmol, 20 eq.), and 64 ml THF. The mixture was then stirred at reflux for 3 hours. The mixture was allowed to cool to room temperature, and was then poured into 250 ml water and filtered. The filtrate was then taken up in 100 ml acetone, triturated and then filtered. The filtrate was then taken up in 100 ml THF, triturated, and filtered to give the crude product as a brown solid, which was taken to the next step without further purification. Yield: 0.28 g, 74%.



TIPS-c-PP: A flame-dried 100 ml RB flask under N_2 was charged with 15 ml anhydrous THF and TIPS-acetylene (1.63 g, 8.93 mmol, 21 eq.), and the solution was cooled to 0 °C. 2.5 M n-butyllithium in hexanes (3.40 ml, 8.50 mmol, 20 eq.) was added slowly, and the reaction mixture was stirred for 30 min. **c-PP-Q** (0.250 g, 0.425 mmol) was added, and the solution was stirred for 16 hours at room temperature. The reaction was quenched with water (20 ml) and 10% HCl (5 ml), extracted in diethyl ether (50 ml) and washed with water (50 ml), and the organic layer was dried with magnesium sulfate. After removal of solvent, the product was purified on a silica plug (5:1 hexanes: ethyl acetate) to give the tetraol as a dark oil. The oil was then redissolved in toluene (10 ml), and 0.500 g tin (II) chloride hydrate was added to the solution, and the reaction mixture was stirred for 2 hours. The reaction was quenched with water (20 ml), extracted into diethyl ether (50 ml) and washed with water (50 ml), and dried with magnesium sulfate. After removal of solvent, the product was purified via column chromatography in 6:1 hexanes:DCM. Yield: 23 mg, 4.4% $^1\text{H NMR}$ (400 MHz, CDCl_3): δ 10.14 (s, 2H), 9.40 (s, 2H), 9.37 (s, 2H), 9.34 (s, 2H), 8.82 (d, $J = 9.2$ Hz, 2H), 8.10 (d, $J = 9.2$ Hz, 2H), 8.03 (m, 4H), 7.46 (dd, $J = 7.2$ Hz, 4H), 1.47 (m, 42H), 1.52 (m, 42H).

Chapter 5: Functionalized Leuco Dyes for Radiochromic Dosimeters

5.1: Introduction to Triphenylmethane dyes for Radiochromic Dosimeters

With the advent of the Presage dosimeter in the early 2000s, the application of triphenylmethane dyes in radiochromic films has received increased attention. Such dosimeters are cheap and light weight, and their sensitivity to radiation can be tuned by changing various aspects of the device composition to meet the needs of various applications. One such application is the need to alert first responders to the presence of harmful levels of radiation while working under hazardous conditions. The flexible and lightweight nature of this class of dosimeters means that they can be affixed to a uniform, making them a convenient alternative to conventional dosimeters. Reports of dosimeters that display linear changes in optical density proportional to radiation dosage suggest that an easy-to-read color response to varying levels of radiation exposure is possible.⁹⁰ However, ensuring that such a linear optical response occurs within the radiation range that would be relevant to first responders would require careful tuning of numerous material and device parameters. The overall goal of the TATTOO project is to develop a lightweight, wearable colorimetric dosimeter that utilizes functionalized triphenylmethane dyes as the active material. The dosimeter prototype will consist of a dye and a halocarbon initiator entrained within a polymer composite, which in the later steps of the project will be encapsulated within a wearable nylon pouch. The dye/polymer composite should remain colorless under ambient conditions, and gradually change color upon increased radiation exposure in the range of 0-20 grays (Gy), where complete conversion to the colored form of the dye occurs at 20 Gy. The color change should be such that the person wearing the sensor can easily discern the dosage of radiation to which they have been exposed.

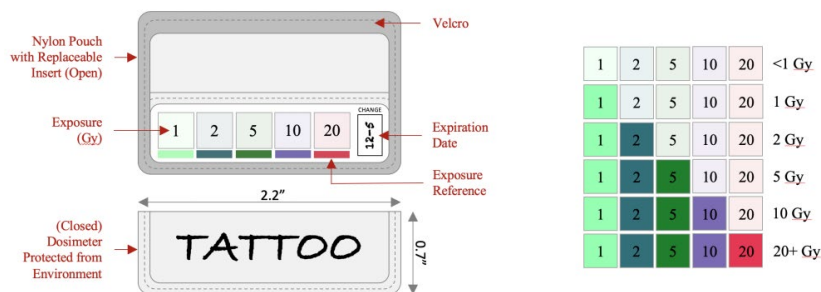


Figure 5:1: Proposed diagram of a TATTOO dosimeter.¹³⁰

As discussed in Chapter 1.9, the addition of functional groups to LMG derivatives is a promising method to impact the reactivity of the dyes upon irradiation. While it has been shown that functionalization of triarylmethanes has little impact on the bond dissociation energy (BDE) of the central methine bond, electron-donating and electron-withdrawing groups do work to stabilize or destabilize, respectively, the resulting cation formed upon oxidation.¹³¹ The stabilizing effect of electron-donating groups is reflected in the increased sensitivity of Presage dosimeters featuring methoxy-substituted LMG dyes.^{95,96} Such studies are sparse however, and thus the exact nature of how functional groups impact the reactivity of LMG green dyes is still unclear. A key aspect of this project will be to systematically alter the reactivity of the dyes through the addition of electron-donating or electron-withdrawing functional groups, which will be substituted at differing positions on the phenyl ring. By utilizing a broader range of functionalities and substitution patterns, we hope to develop molecular design principles for tuning the sensitivity of LMG derivatives to irradiation. The impact of functionalization can be observed qualitatively by the rate of color change and quantitatively by spectroscopic methods such as UV-Vis. While solution studies can provide a baseline for their relative sensitivity, the applicability of the dyes ultimately depends on their reactivity when mixed with the other components of the dosimeter.

The initial stages of the TATTOO project will consist of the screening of several composites, each consisting of a leuco dye, a polymer or resin, and a halocarbon activator. The reactivity of the dyes within these composites can provide feedback on further chemical modifications that may better optimize their

sensitivity within the necessary dosage range. Additionally, the sensitivity of the composites will be tuned by adjusting other parameters, including the structures of the initiator and polymer, the wt% of the formulation components, and the annealing process. The structure of the activator has been shown to impact the sensitivity of Presage films, with the reactivity of halocarbon activators generally increasing in the order $\text{Cl} < \text{Br} < \text{I}$, which can be attributed to decreasing bond dissociation energies (BDE) of the halogen-carbon bond.⁹⁸ The wt% of the components within the films also plays an important role, as Presage films become more sensitive with increased concentration of the initiator.⁹⁸ The nature of the polymer or resin can greatly impact the miscibility of the formulation components, as well as the stability of the radical and cationic species, thus also impacting the sensitivity of the film. Because each of these parameters must be examined in conjunction with the other components of the dosimeters, many composites will need to be formulated. We will thus work with collaborators at Savannah River National Laboratory, who will work primarily on irradiating tiles of various compositions to help establish which dyes, polymers, and initiators should be the focus of future studies.

5.2: Synthesis of Leuco Dyes

The synthesis of the functionalized LMG dyes makes use of a straightforward condensation reaction, and typically consists of only one step. Optimal conditions utilized the functionalized benzaldehyde, an excess of the N,N-dialkylaniline (~4 eq.), and p-toluenesulfonic acid in benzene heated at reflux. It was found that removal of any remaining benzaldehyde in the crude product was quite tedious by chromatography, and so it is important that the reaction consumes all of the benzaldehyde to allow for efficient purification of the crude product. To push the reaction between the N,N-dialkylaniline and the benzaldehyde to completion, the water that is formed as a byproduct was removed via azeotropic distillation using a Dean-Stark apparatus. Because of the simple and versatile nature of the synthesis, several functionalized dyes were made by utilizing different aromatic aldehydes with varying substituents (Figure

5.2). The N,N-alkyl substituents on the dyes could be altered by performing the condensation reaction with either N,N-dimethylaniline (DMA), N,N-diethylaniline (DEA), or N,N-dibutyl substituents (DBA) to yield derivatives with methyl, ethyl, and butyl substituents, respectively.

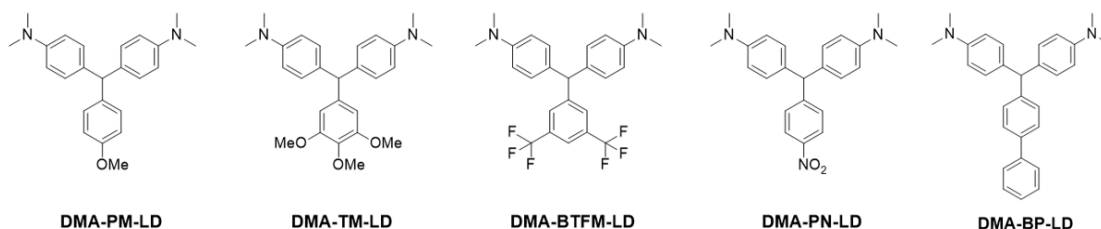


Figure 5:2: Examples of DMA-substituted dyes with various functionalities synthesized in this project.

The reactivity of the dyes can be qualitatively observed by how readily they change from the leuco form to the colored form under ambient conditions, as shown in Figure 5.3. In general, the reactivity of the dyes increases with the addition of the electron-donating methoxy groups, compared to those with electron-withdrawing groups such as nitro or trifluoromethyl substituents. Out of these dyes, DMA-PM-LD showed the fastest and most pronounced change in color upon dissolution in DCM under ambient light. A possible explanation is that the electron-rich methoxy group at the para-position stabilizes the cation formed upon activation of the dyes. This corroborates reports on increased reactivity in ortho-methoxy substituted LMG, as the ortho-para positions can best stabilize the trityl cation due to resonance considerations.⁹⁵ Interestingly, DMA-PM-LD was even more reactive than DMA-TM-LD, despite containing fewer electron-donating methoxy groups. In the case of 3,4,5-trimethoxy-substituted dyes, the meta-methoxy substituents likely cannot contribute to the resonance structure of the cation and may even serve as electron-withdrawing groups, thus slightly hindering the reactivity. DMA-BP-LD shows somewhat slower activation than the methoxy-substituted dyes, which suggests that extending the conjugation length of the aromatic group does not affect the reactivity in the same manner as electron-donating substituents. The dyes featuring electron-withdrawing groups, DMA-BTFM-LD and DMA-PN-LD, appear to show the slowest reactivity of all

these dyes, although the yellow color of the dyes in solution made the change in color difficult to observe. The electron-deficient nature of the TFM and nitro substituents likely destabilize the central cation, and thus make formation of the activated dyes less favorable.

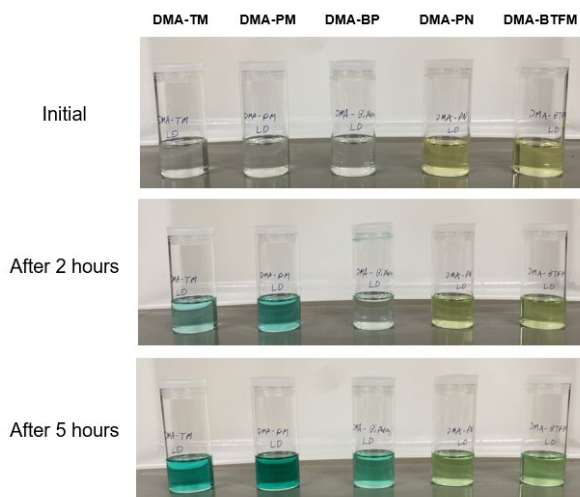


Figure 5:3: Color change of Leuco dyes dissolved in DCM under ambient laboratory conditions.

UV-Vis was employed to gain more quantitative insight into the optical properties of the dyes. All derivatives show onset absorbance peaks between 260-280 nm in their leuco form (Figure 5.4a), with those featuring electron-withdrawing substituents (**DMA-BTFM-LD** and **DMA-PN-LD**) slightly redshifted compared to the more electron rich dyes. Due to the break in conjugation induced by the central methane, the FMOs are primarily localized on the phenyl rings, as evidenced by the high-energy optical gaps that change little upon functionalization. The spectra for the partially activated dyes (Figure 5.4b) display onset absorbance peaks between 600-700 nm, consistent with the cationic form of the dyes.⁹⁵ The impact of functionalization is more pronounced in the activated dyes, as the onset absorbance is incrementally shifted based on the donating or withdrawing strength of the substituents. The cation formed upon activation of the dyes is in part stabilized by the electron-donating methoxy groups, and is destabilized by the electron-withdrawing nitro or trifluoromethyl groups. Overall, increased reactivity of the dyes correlates with incremental blue shifts in the

onset absorption energy of the activated dye, providing further evidence that stabilization/destabilization of the cation is an effective method to tune their sensitivity. Notably, **DMA-TM-LD** is slightly redshifted compared to **DMA-PM-LD** despite a greater number of electron-donating groups, providing evidence that the meta-substituted methoxy groups may slightly destabilize the cation due to resonance considerations.

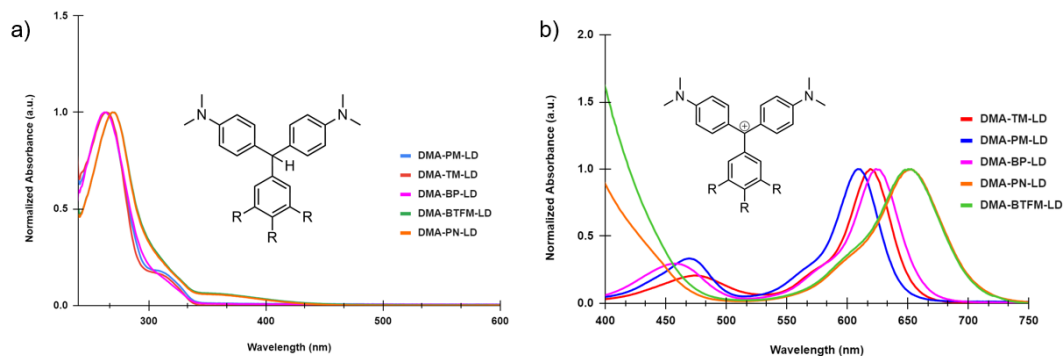


Figure 5:4: UV-Vis spectra for DMA-substituted dyes in chloroform.

5.3: Incorporation of Leuco Dyes into Polymer Composites

The dyes were incorporated into composites utilizing various polymers and initiators. In the case of **DMA-FTFM-LD** and **DMA-PN-LD**, the yellow color of the inactivated dyes prevented easy detection of color change upon activation, and thus were not evaluated further. The poor miscibility of **DMA-BP-LD** inhibited its incorporation into virtually all composites, and was also ruled out from further study. Methoxy-substituted **DMA-PM-LD** and **DMA-TM-LD** were thus the primary dyes considered in the tuning of composite parameters. The reactivity of the composites varied drastically depending on the combination of dye, polymer, and initiator. Epoxy and PMMA blends with **DMA-PM-LD** and **DMA-TM-LD** all showed some coloration between 0-100 Gy when used with initiators such as tetrachloroethane, hexachloroethane, and hexabromoethane (Figure 5.5a). However, similar blends using 1,2-dichloroethane, trichloroethylene, or iodomethane activators showed no color change. The reactivity of the activators can in part be attributed to the BDE of the carbon-halogen bond, where BDE tends to decrease with increased substitution as well as increased size of the

halogen, i.e. going from Cl to Br to I.¹³² Thus, more substituted activators (tetrachloroethane, hexachloroethane, etc.) as well as those featuring multiple Br or I substituents (dibromomethane, diiodomethane, etc.) are generally more likely to undergo homolytic bond cleavage upon irradiation and activate the dye. Another approach is to make use of a halogenated polymer, such as polyvinylchloride (PVC), that can function both as a host material and as an activator. However, **DMA-PM-LD** displayed immediate color change when blended with PVC, suggesting that smaller loading percentages of activator are needed to induce more gradual coloration. The highly substituted nature of the PVC structure can also stabilize the radical generated upon irradiation, which likely makes it more reactive compared to smaller, less substituted initiators. It should be noted that PVC formulations containing 10% triethylamine did not change color, providing evidence that amines inhibit the activation of the dyes.

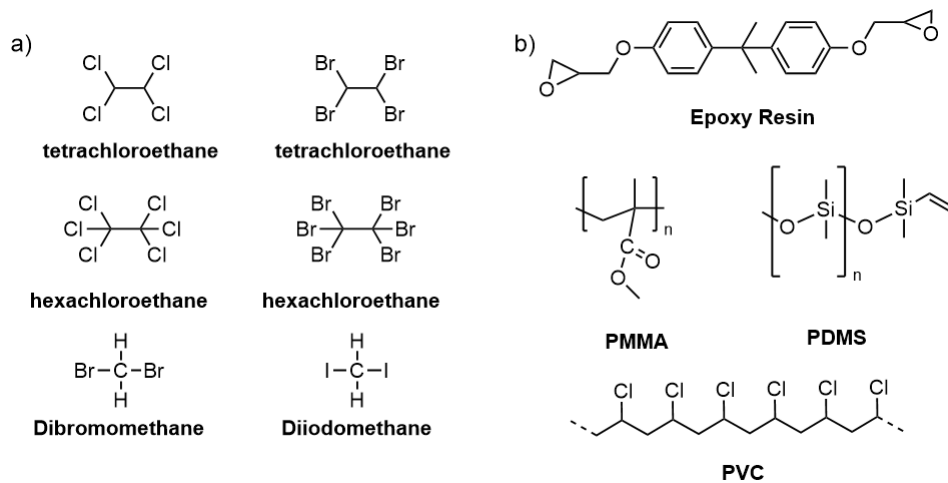


Figure 5:5: Examples of (a) activators and (b) polymers and resins used in the formulations of composites.

Miscibility among the formulation components is necessary to form uniform blends and thus achieve a consistent, linear activation gradient. However, many of these blends suffered from poor miscibility between dye, resin, and activator, which in some instances resulted phase separation of the resin and the dye/activator (Figure 5.6a). The use of diiodomethane as activator aided in miscibility between dye and polymer, and when mixed with **DMA-PM-LD** in

epoxy resin yielded a composite with a steady color gradient in the range 2.5-100 Gy (Figure 5.6b). However, the cross-linkers present in the epoxy resins, which are necessary in the curing process, contain amine groups which cause deactivation of the dye. This issue may be addressed by using a polymer such as PDMS, which can be used with amine-free cross-linkers. Unfortunately, PDMS shows poor miscibility with virtually all dye/initiator combinations tested, including those utilizing diiodomethane (Figure 5.6c). Future studies will attempt to incorporate other polymers and resins that show miscibility with appropriate dyes while also inhibiting reversibility of the resulting composite.

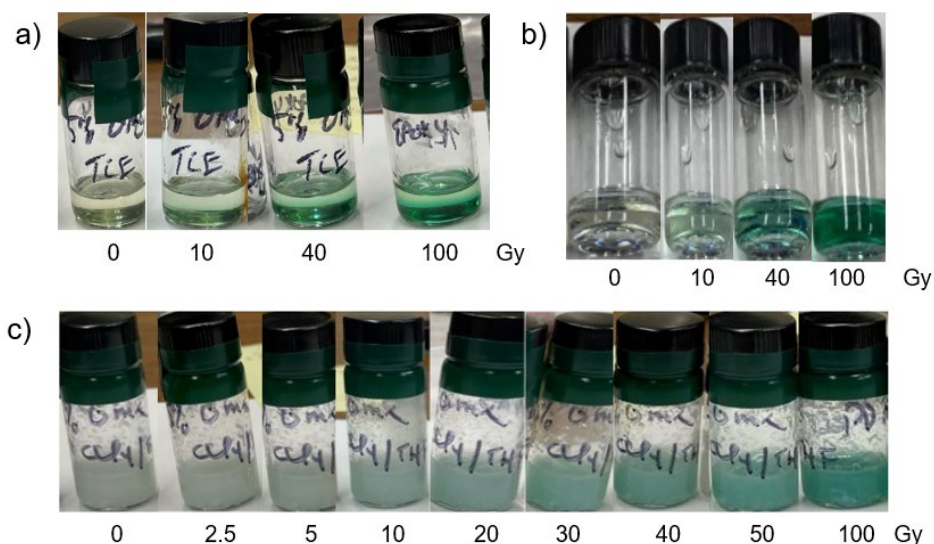


Figure 5:6: (a) **DMA-TM-LD** in epoxy with TCE as activator, (b) **DMA-PM-LD** in epoxy resin with diiodomethane activator, (c) **DMA-PM-LD** in PDMS with CCl_4 activator.

In order to improve the miscibility of the dyes within the composite blends, dyes featuring ethyl or butyl chains on the N,N-dialkylaniline moieties were synthesized to yield liquid dyes with drastically improved solubility. However, these dyes displayed a brownish tint that discolored the resulting composites, which hindered the ability to readily observe color change (Figure 5.7). Other attempts at improving processability including the addition of alkyl chains to the functionalized ring. Much like **DEA-PM-LD** and **DBA-PM-LD**, **DMA-EH-LD** showed excellent solubility in common organic solvents and composites while

remaining colorless in the leuco form. However, **DMA-EH-LD** showed little color change in various composites, even at irradiation >20 Gy. This provides further evidence that electron-donating groups at the meta positions of the functionalized ring do little to contribute to the reactivity of the dye. The reactivity of processable dyes may be addressed by the substitution of alkyloxy groups at the more reactive positions of the phenyl ring, such as the para-position.

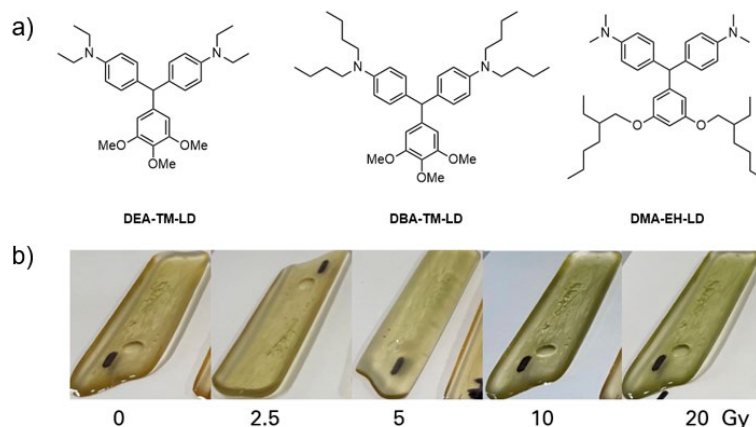


Figure 5:7: (a) structures of dyes with extended alkyl chains, (b) Free-standing epoxy composites utilizing **DEA-TM-LD**.

5.4: Conclusion

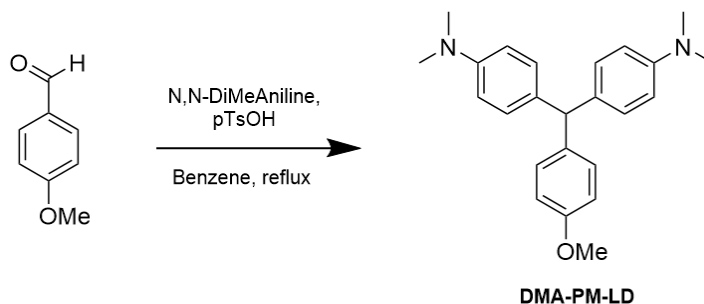
A series of functionalized leucomalachite green dyes were studied for their application in lightweight, flexible dosimeters. The functional groups attached to the phenyl moiety were found to be critical in tuning a dyes sensitivity to radiation. In general, electron-donating groups increased the reactivity of the dyes when substituted at the para-positions, but somewhat hindered reactivity when substituted at the meta-positions. The optical gap was investigated through UV-Vis, with the more reactive dyes displaying slightly blue-shifted absorbance compared to their less reactive counterparts. Due to their combination of sensitivity, solubility, and colorless appearance in non-radiated films, para-methoxy and 3,4,5-trimethoxy substituted dyes were found to be the most optimal of the dyes studied for incorporation into radiochromic formulations. In addition to the nature of the dye, the polymer, initiator, and formulation were all found to significantly impact the reactivity of the composites. Of the formulations

that have been tested so far, those featuring epoxy resins tend to display the best miscibility of the components as well as steady coloration upon radiation exposure. The use of diiodomethane as an activator aids in miscibility, and corresponding formulations display adequate color change within the desired range. Epoxy composites suffer from reversible color change, likely due to the presence of amine-containing cross-linkers within the resin. Future studies will incorporate new resins that inhibit this discoloration while still maintaining adequate miscibility with the formulation components.

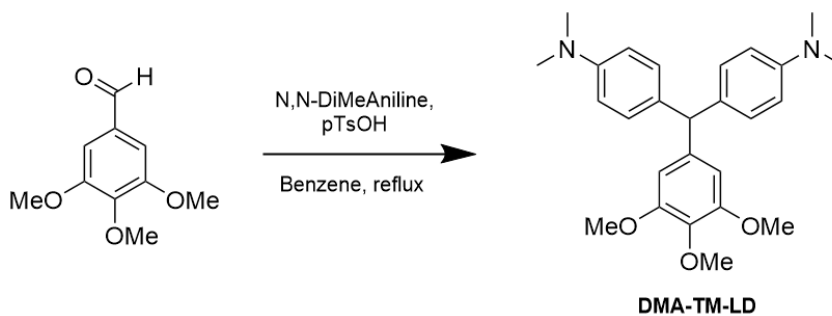
5.5: Experimental

All reagents and solvents were obtained from Sigma Aldrich, Oakwood Chemicals, Gelest, or VWR and used without further purification. ^1H and ^{13}C NMR spectra were measured on a 400 MHz Bruker NMR spectrometer in CDCl_3 (7.26 ppm for ^1H NMR, 77.16 ppm for ^{13}C NMR). Solution UV-vis was recorded on an Agilent Carey 60 UV-Vis spectrophotometer.

General Procedure: A 100 ml RB flask was charged with the appropriate N,N-dialkylaniline (4 eq.), the functionalized benzaldehyde (1 eq.), p-toluenesulfonic acid (2 eq.) and benzene (0.5 M). The flask was outfitted with a dean-stark condenser and the reaction mixture was heated at reflux for ~16 hours. The reaction mixture was allowed to cool to room temperature, and then poured into an aqueous solution of sodium bicarbonate and extracted into ethyl acetate. The organic layer was dried with magnesium sulfate and the solvent was removed. The crude product was purified by chromatography in hexanes:ethyl acetate.

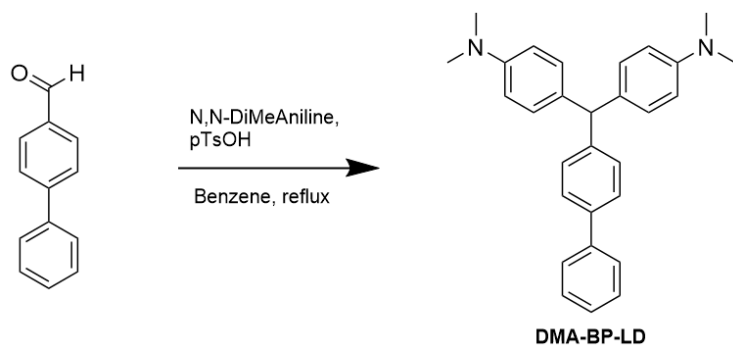


DMA-PM-LD: N,N-dimethylaniline (5.55 ml, 44.0 mmol, 4 eq.), 4-methoxybenzaldehyde (1.50 g, 11.0 mmol, 1 eq.), p-toluenesulfonic acid (4.18 g, 22.0 mmol, 2 eq.) and benzene (22 ml) were reacted by the general procedure. The crude product was purified by silica chromatography in 4:1 hexanes:ethyl acetate to give the product as a white solid. Yield: 2.53 g, 64%. ^1H NMR (400 MHz, CDCl_3): δ 7.08 (d, $J = 8.4$ Hz, 2H), 7.02 (d, $J = 8.8$ Hz, 4H), 6.84 (d, $J = 8.4$ Hz, 2H), 6.70 (d, $J = 8.8$ Hz, 4H), 5.38 (s, 1H), 3.82 (s, 3H), 2.95 (s, 12H). ^{13}C NMR (101 MHz, CDCl_3): 157.69, 148.96, 137.71, 133.27, 130.26, 129.90, 113.48, 112.60, 55.25, 54.19, 40.81.

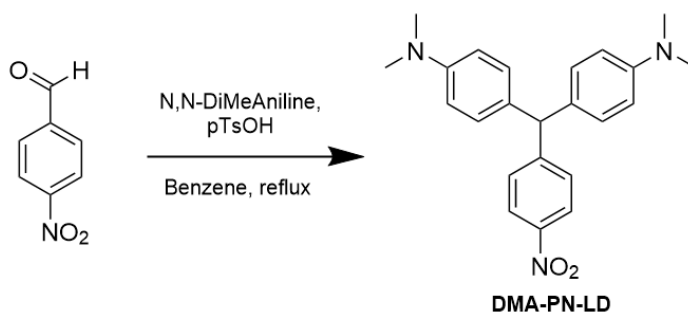


DMA-TM-LD: N,N-dimethylaniline (4.03 ml, 32.0 mmol, 4 eq.), 3,4,5-trimethoxybenzaldehyde (1.57 g, 8.00 mmol, 1 eq.), p-toluenesulfonic acid (2.75 g, 16.0 mmol, 2 eq.) and benzene (16 ml) were reacted by the general procedure. The crude product was purified by silica chromatography in 4:1 hexanes:ethyl acetate to give the product as a white solid. Yield: 1.76 g, 52%. ^1H NMR (400 MHz, CDCl_3): δ 7.02 (d, $J = 8.8$ Hz, 4H), 6.70 (d, $J = 8.8$ Hz, 4H), 6.41 (s, 2H), 5.33 (s, 1H), 3.86 (s, 3H), 3.77 (s, 6H), 2.95 (s, 12H). ^{13}C NMR (101

MHz, CDCl₃): 152.87, 149.00, 141.09, 136.05, 132.76, 129.86, 112.54, 106.55, 60.84, 56.04, 55.28, 40.76.

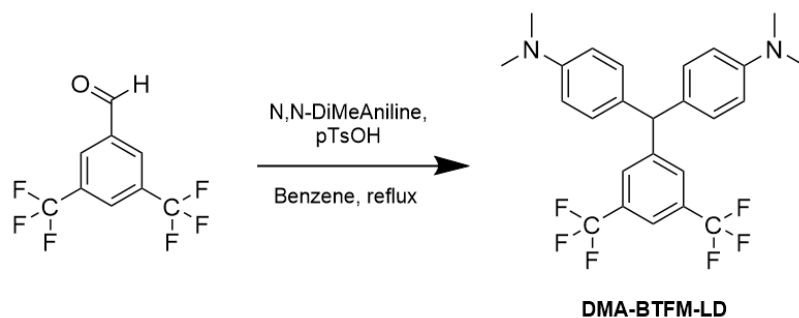


DMA-BP-LD: N,N-dimethylaniline (4.03 ml, 32.0 mmol, 4 eq.), biphenyl-4-carboxaldehyde (1.46 g, 8.00 mmol, 1 eq.), p-toluenesulfonic acid (2.75 g, 16 mmol, 2 eq.) and benzene (16 ml) were reacted by the general procedure. The crude product was purified by silica chromatography in 4:1 hexanes:ethyl acetate to give the product as a white solid. Yield: 0.97 g, 29%. ¹H NMR (400 MHz, DMSO-d₆): δ 7.58 (d, *J* = 7.2 Hz, 2H), 7.50 (d, *J* = 8.4 Hz, 2H), 7.41 (t, *J* = 7.6 Hz, 2H), 7.30 (t, *J* = 7.6 Hz, 1H), 7.16 (d, *J* = 8 Hz, 2H), 6.93 (d, *J* = 8.4 Hz, 4H), 6.63 (d, *J* = 8.8 Hz, 4H), 5.35 (s, 1H), 2.90 (s, 12H). ¹³C NMR (101 MHz, CDCl₃): 149.07, 145.02, 140.71, 138.29, 132.47, 130.01, 129.21, 127.49, 127.04, 126.83, 112.81, 54.69, 40.18.

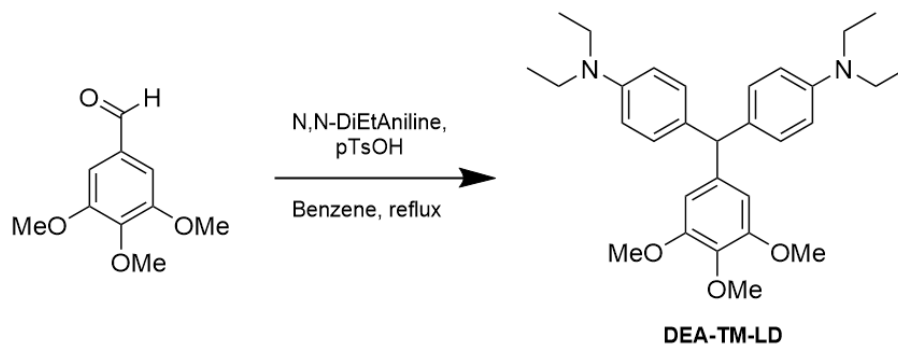


DMA-PN-LD: N,N-dimethylaniline (4.03 ml, 32.0 mmol, 4 eq.), 4-nitrobenzaldehyde (1.21 g, 8.00 mmol, 1 eq.), p-toluenesulfonic acid (2.75 g, 16.0 mmol, 2 eq.) and benzene (16 ml) were reacted by the general procedure.

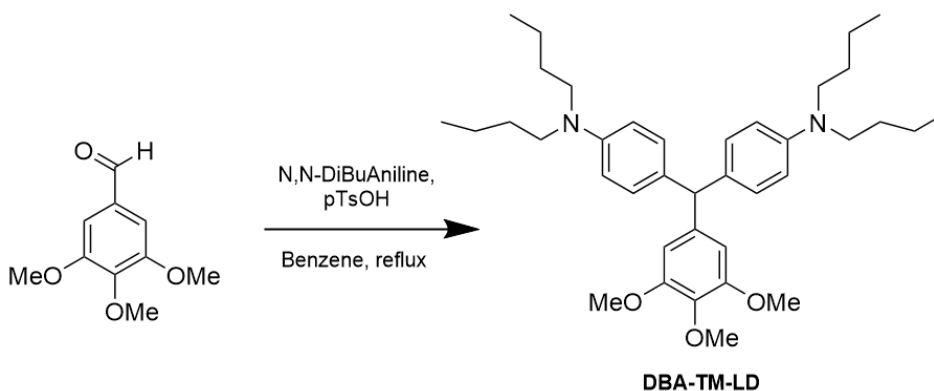
The crude product was purified by silica chromatography in 4:1 hexanes:ethyl acetate to give the product as a yellow solid. Yield: 2.13 g, 71%. ^1H NMR (400 MHz, CDCl_3): δ 8.12 (d, $J = 8$ Hz, 2H), 7.33 (d, $J = 8$ Hz, 2H), 6.90 (d, $J = 8$ Hz, 4H), 6.64 (d, $J = 8$ Hz, 4H), 5.48 (s, 1H), 2.89 (s, 12H). ^{13}C NMR (101 MHz, DMSO-d_6): 153.96, 149.31, 146.09, 131.07, 130.50, 129.96, 123.65, 112.87, 54.62, 40.65.



DMA-BTFM-LD: N,N-dimethylaniline (4.03 ml, 32.0 mmol, 4 eq.), 3,5-bis(trifluoromethyl)benzaldehyde (1.94 g, 8.00 mmol, 1 eq.), p-toluenesulfonic acid (2.75 g, 16.0 mmol, 2 eq.) and benzene (16 ml) were reacted by the general procedure. The crude product was purified by silica chromatography in 4:1 hexanes:ethyl acetate to give the product as a white solid. Yield: 3.35 g, 90%. ^1H NMR (400 MHz, DMSO-d_6): δ 8.12 (d, $J = 8.8$ Hz, 2H), 7.33 (d, $J = 8.4$ Hz, 2H), 6.90 (d, $J = 8.8$ Hz, 4H), 6.64 (d, $J = 8.8$ Hz, 4H), 5.48 (s, 1H), 2.90 (s, 12H). ^{13}C NMR (101 MHz, DMSO-d_6): 153.96, 149.31, 146.09, 131.06, 130.50, 129.60, 123.64, 112.87, 54.63, 40.16.

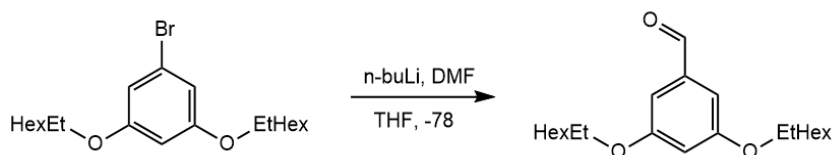


DEA-TM-LD: N,N-diethylaniline (4.85 ml, 30.6 mmol, 4 eq.), 3,4,5-trimethoxybenzaldehyde (1.50 g, 7.65 mmol, 1 eq.), p-toluenesulfonic acid (2.63 g, 15.3 mmol, 2 eq.) and benzene (16 ml) were reacted by the general procedure. The crude product was purified by silica chromatography in 6:1 hexanes:ethyl acetate to give the product as a viscous oil. Yield: 1.73 g, 3.63 mmol, 47%. ¹H NMR (400 MHz, DMSO-d₆): δ 6.89 (d, *J* = 8.8 Hz, 4H), 6.56 (d, *J* = 8.8 Hz, 4H), 5.18 (s, 1H), 3.65 (s, 9H), 3.25 (q, *J* = 7.2 Hz, 8H), 1.04 (t, *J* = 7.2 Hz, 12H). ¹³C NMR (101 MHz, DMSO-d₆): δ 152.98, 146.11, 141.68, 136.13, 131.43, 130.00, 111.79, 106.89, 60.38, 56.19, 54.99, 44.07, 12.89.

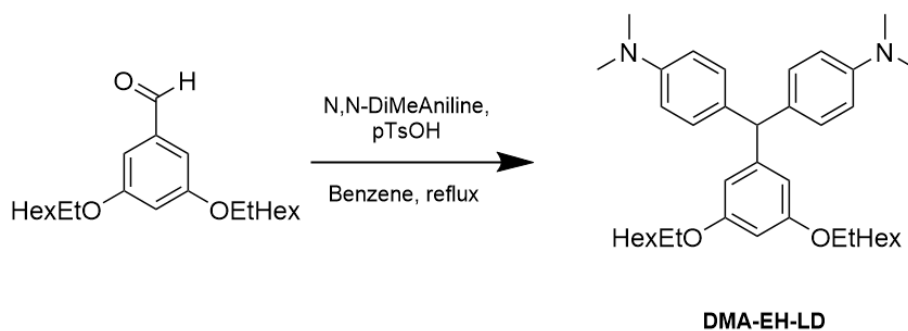


DBA-TM-LD: N,N-dibutylaniline (6.89 ml, 30.6 mmol, 4 eq.), 3,4,5-trimethoxybenzaldehyde (1.50 g, 7.65 mmol, 1 eq.), p-toluenesulfonic acid (2.63 g, 15.3 mmol, 2 eq.) and benzene (16 ml) were reacted by the general procedure. The crude product was purified by silica chromatography in 7:1 hexanes:ethyl acetate to give the product as a viscous oil. Yield: 1.54 g, 2.61

mmol, 34%. $^1\text{H NMR}$ (400 MHz, DMSO-d_6): δ 6.93 (d, $J = 8.8$ Hz, 4H), 6.58 (d, $J = 8.8$ Hz, 4H), 5.22 (s, 1H), 3.72 (s, 9H), 3.29 (t, $J = 7.6$ Hz, 8H), 1.57 (q, $J = 7.6$ Hz, 8H), 1.36 (sept, $J = 7.6$ Hz, 8H), 0.98 (t, $J = 7.6$ Hz, 12H). $^{13}\text{C NMR}$ (101 MHz, DMSO-d_6): δ 153.10, 146.50, 141.39, 136.67, 131.48, 129.96, 111.71, 107.14, 59.72, 55.56, 50.83, 29.68, 20.47, 13.91.



3,5-bis(2-ethylhexyloxy)benzaldehyde: A flame-dried 100-ml flask under N_2 atmosphere was charged with anhydrous THF (30 ml) and 1-bromo-3,5-bis(2-ethylhexyloxy)benzene (4.00 g, 9.71 mmol), and the flask was cooled to -78 $^\circ\text{C}$. Then, 2.5M n-butyllithium in hexanes (4.28 ml, 10.7 mmol) was added dropwise, and the mixture was allowed to stir for 1 hour at -78 $^\circ\text{C}$. N,N-dimethylformamide (1.51 ml, 19.4 mmol) was then added slowly, and the mixture was allowed to warm to room temperature and was stirred for 16 hours. The mixture was quenched with water, and the organic layer was extracted into hexanes, dried with magnesium sulfate, and the solvent removed. The crude product was purified via silica chromatography in 5:1 hexanes:DCM. The solvent was then removed to give the product as a yellow oil. Yield: 3.11 g, 8.59 mmol, 88%.



DMA-EH-LD: N,N-dimethylaniline (4.03 ml, 32.0 mmol, 4 eq.), 3,5-bis(2-ethylhexyloxy)benzaldehyde (2.90 g, 8.00 mmol, 1 eq.), p-toluenesulfonic acid

(2.75 g, 16.0 mmol, 2 eq.) and benzene (16 ml) were reacted by the general procedure. The crude product was purified by silica chromatography in 7:1 hexanes:ethyl acetate to give the product as a colorless oil. Yield: 2.51 g, 4.27 mmol, 51%.

Chapter 6: Summary

The realization of the next generation of organic electronics will require multidisciplinary collaboration, from materials design and synthesis to device optimization and ultimately commercialization. The properties of organic materials relevant to electronic performance are highly dependent on their molecular structure, and thus a firm understanding of molecular design principles is necessary to design new materials with exciting electronic characteristics. The projects detailed throughout this dissertation focus on the development of synthetic protocols that allow for scalable, straightforward synthesis of multiple derivatives within a class of compounds. The ability to systematically tune organic materials is a key aspect of organic electronics research, and each chapter demonstrates the use of careful synthetic strategy to optimize a class of molecules for a given application.

Chapter 2 described the synthesis of a series of pyrene-fused acenes, otherwise known as vertical pyrenes, through a synthetic route that allows for straightforward alteration of the length and functionalities on the acene substituents. Experimental studies on APA confirm that the central pyrene disrupts conjugation between the fused acene moieties, in agreement with computational results. Lengthening the acene moieties from anthracene to tetracene reduces the size of the HOMO-LUMO gap, demonstrating that the electronic properties of vertical pyrenes can be tuned in a similar manner to the corresponding acenes. This trend was further corroborated by replacing silylethyne groups with phenylethyne substituents, which resulted in red-shifted absorbance consistent with that seen in BPEA compared to TIPS-anthracene. Considering that tetracene and BPEA are well-studied SF materials, the vertical pyrenes featuring these chromophores were submitted to collaborators to investigate the SF process in these pyrene-fused dimers. **NODIPS-TPT** displayed efficient formation of a long-lived ^5TT state via a SF process, which was attributed to the planar, rigid structure of the vertical pyrene framework. The rather unique SF properties of this vertical pyrene make them suited for QIS

applications, and further studies will aim to better optimize the SF process through further tuning of the molecular structure.

Chapter 3 detailed the study of a series of extended 2-D acenoacenes. The synthetic route provided straightforward control over molecular length and functionalities, and allowed for the isolation of the longest stable acenoacene reported to date. These compounds belong to a class of “oblique” pyrenes and displayed contiguous conjugation, as evidenced by their small HOMO-LUMO gaps and red-shifted absorbance compared to the vertical pyrenes described in Chapter 2. Our bispentacenes and bishexacenes display significantly greater resistance to photooxidation than their linear acene counterparts, consistent with previous literature reports on smaller acenoacenes. Surprisingly, our bishexacenes show greater stability than bispentacenes upon prolonged light exposure, which runs counter to the trend observed in the linear acene series. The stability in **NODIPS-BH** has thus far been attributed to its low triplet energy, which slows the generation of $^1\text{O}_2$ and thus inhibits endoperoxide formation via an energy transfer mechanism. More detailed studies are necessary to fully elucidate the decomposition mechanisms undergone by acenoacenes. Future studies will also aim to tune the crystal packing of these acenoacenes via functionalization of the molecular backbone, with the goal of achieving brickwork packing structures suitable for OFET applications.

The role of ring annulation in 2-D acene derivatives was explored further in Chapter 4, which described a novel synthetic route to a functionalized cata-annulated pentacenopentacene. In contrast to previously reported non-functionalized derivatives, **TIPS-c-PP** was stable enough to isolate and characterize under ambient conditions, which can be attributed to impact of silylethynyl substituents in hindering decomposition. The enhanced stability brought about through functionalization allows for more thorough study of cata-acenoacenes and for comparison to their peri-annulated counterparts. Absorption data suggests that **c-PP** derivatives maintain electronic properties that are more reminiscent of pentacene than other fused-pentacene derivatives with peri-annulated structures. Despite its pentacene-like electronic structure, **TIPS-c-PP**

displays photostability on-par with oblique pyrenes of similar size, providing further evidence that a 2-D framework helps to stabilize larger acene derivatives.

Chapter 5 focused on the application of functionalized LMG dyes in radiochromic dosimeters. The dyes were synthesized via a simple, scalable one-step synthesis which allowed for the screening of several functionalized dyes for incorporation into radiochromic composites. Alteration of the functional groups attached to the phenyl moiety tunes the sensitivity of the dye to radiation, which are qualitatively observed by the dyes pronounced color change. The impact of functionalization was measured quantitatively by UV-Vis, in which the onset absorbance correlates to the sensitivity of the dyes. Various factors impact the sensitivity of the dyes within the composites, including the functionalities on the dye, the polymer matrix, and the initiator. Composites that utilized methoxy-substituted dyes showed color change within ideal dosage ranges. One obstacle that should be addressed in future studies is poor miscibility of the dyes with the polymer, which negatively impacts the ability of the composite to undergo linear activation. Functionalization of the dyes to improve solubility can also make possible the use of a greater variety of polymers and activators, which in turn allows for greater control over the activation range.

Future work on these projects will involve continued efforts to better optimize these classes of materials for implementation into organic electronic devices. A key aspect of such efforts will include further optimization of synthetic protocols, as production of these materials should be relatively cheap, simple and scalable for them to be viable for in-depth study. Continued interdisciplinary collaborations, such as those detailed in Chapter 2 and Chapter 5, will also be critical for the implementation of these classes of materials into device applications, as well as for the design future materials. The materials in Chapter 3 and Chapter 4 are still in the early stages of development, and further tuning of properties such as solid-state order are still necessary before their potential in electronic devices can be explored further. However, the fundamental electronic properties of each class of materials are highly encouraging for the applications outlined in Chapter 1, and merit further study.

In conclusion, the efficient use of organic synthesis to strategically alter the properties of organic electronic materials was demonstrated throughout this dissertation. The synthetic protocols detailed in each chapter allow for straightforward tuning of molecular size and functionalities, providing strategic control over electronic properties. The systematic tuning of molecular structure is shown to significantly impact the properties of polycyclic aromatic hydrocarbons, providing valuable rational design guidelines for the development of more efficient electronic materials. The work in this dissertation emphasizes how strategic synthetic design is vital for the research and discovery of the next generation of organic electronic materials.

Appendix

Å – Angstrom
AP – Anthracene-pyrene
APA – Anthracene-pyrene-anthracene
BDE – Bond dissociation energy
BH – Bishexacene
BHep – Bisheptacene
BP – Biphenyl
BP – Bispentacene
BPEA – Bis(phenylethynyl)anthracene
BTFM – Bis(trifluoromethyl)
c – Cata
CV – Cyclic voltammetry
DBA – Dibutylaniline
DCM – Dichloromethane
DFT – Density-functional theory
DMA – Diethylaniline
DMA – Dimethylaniline
EH – Ethylhexyloxy
eV – Electron volt
FMO – Frontier molecular orbital
Gy – Gray
HCl – Hydrochloric acid
HOMO – Highest occupied molecular orbital
LD – Leuco dye
LMG – Leucomalachite green
LUMO – Lowest occupied molecular orbital
M – Molar
MALDI – Matrix-assisted laser desorption/ionization
MG – Malachite green
MS – Mass-spectroscopy
NICS – Nucleus-independent chemical shift
nm – nanometer
NMR – Nuclear magnetic resonance
NODIPS – n-octyldiisopropylsilyl
OFET – Organic field-effect transistor
OSC – Organic semiconductor
PAH – Polycyclic aromatic hydrocarbon
PDMS – Polydimethylsiloxane
PE – Phenylethynyl
Pen – Pentacene
PL – Photoluminescent
PM – para-methoxy
PMMA – Polymethyl methacrylate
PN – Para-nitro
PP – Pentacenopentacene
PV – photovoltaic
PVC – Polyvinylchloride

Q – Quinone
QIS – Quantum information science
SF – Singlet fission
SnCl₂ – tin (ii) chloride
TAS – Trialkylsilyl
THF – Tetrahydrofuran
TIPS – Triisopropylsilyl
TM – Trimethoxy
TMS – Trimethylsilyl
TNPS – tri-n-propylsilyl
TP – Tetracene-pyrene
TPT – Tetracene-pyrene-tetracene
TTA – Triplet-triplet annihilation
μ – Charge carrier mobility

References

- (1) Arfin, T.; Ranjan, P.; Bansod, S.; Singh, R.; Ahmad, S.; Neeti, K. Organic Electronics: Introduction. *Eng. Mater.* **2001**, *45* (1), 1–26. -4_1.
- (2) Jester, T. L. Crystalline Silicon Manufacturing Progress. *Prog. Photovoltaics Res. Appl.* **2002**, *10* (2), 99–106.
- (3) Chang, J. S.; Facchetti, A. F.; Reuss, R. A Circuits and Systems Perspective of Organic/Printed Electronics: Review, Challenges, and Contemporary and Emerging Design Approaches. *IEEE J. Emerg. Sel. Top. Circuits Syst.* **2017**, *7* (1), 7–26.
- (4) Luo, Y.; Wang, M.; Wan, C.; Cai, P.; Loh, X. J.; Chen, X. Devising Materials Manufacturing Toward Lab-to-Fab Translation of Flexible Electronics. *Adv. Mater.* **2020**, *32* (37), 1–14.
- (5) Rivnay, J.; Owens, R. M.; Malliaras, G. G. The Rise of Organic Bioelectronics. *Chem. Mater.* **2014**, *26* (1), 679–685.
- (6) Chondroudis, K.; Kagan, C. R. Organic – Inorganic Electronics. **2001**, *45* (1), 29–45.
- (7) Lamport, Z. A.; Haneef, H. F.; Anand, S.; Waldrip, M.; Jurchescu, O. D. Tutorial: Organic Field-Effect Transistors: Materials, Structure and Operation. *J. Appl. Phys.* **2018**, *124* (7).
- (8) Sirringhaus, H. 25th Anniversary Article: Organic Field-Effect Transistors: The Path beyond Amorphous Silicon. *Adv. Mater.* **2014**, *26* (9), 1319–1335.
- (9) Forrest, S. R.; Thompson, M. E. Introduction: Organic Electronics and Optoelectronics. *Chem. Rev.* **2007**, *107* (4), 923–925.
- (10) Malliaras, G.; Friend, R. An Organic Electronics Primer. *Phys. Today* **2005**, No. May, 53–58.
- (11) Torrent, M. M.; Rovira, C. Novel Small Molecules for Organic Field-Effect Transistors: Towards Processability and High Performancens. *Chem. Soc. Rev.* **2008**, *37* (4), 827–838.
- (12) Coropceanu, V.; Cornil, J., Da Silva Filho, D. A., Olivier, Y., Silbey, R., J. L. B. Charge Transport in Organic Semiconductors. *Chem. Rev.* **2007**, *107*, 926–952.
- (13) Wang, C.; Dong, H.; Jiang, L.; Hu, W. Organic Semiconductor Crystals. *Chem. Soc. Rev.* **2018**, *47* (2), 422–500.
- (14) Brédas, J. L.; Calbert, J. P.; Da Silva Filho, D. A.; Cornil, J. Organic Semiconductors: A Theoretical Characterization of the Basic Parameters

- Governing Charge Transport. *Proc. Natl. Acad. Sci. U. S. A.* **2002**, 99 (9), 5804–5809.
- (15) Marcus, R. A. Electron Transfer Reactions in Chemistry: Theory and Experiment (Nobel Lecture). *Angew. Chemie Int. Ed. English* **1993**, 32 (8), 1111–1121.
- (16) Sakanoue, K.; Motoda, M.; Sugimoto, M.; Sakaki, S. A Molecular Orbital Study on the Hole Transport Property of Organic Amine Compounds. *J. Phys. Chem. A* **1999**, 103 (28), 5551–5556.
- (17) Naibi Lakshminarayana, A.; Ong, A.; Chi, C. Modification of Acenes for N-Channel OFET Materials. *J. Mater. Chem. C* **2018**, 6 (14), 3551–3563.
- (18) Zaumseil, J.; Sirringhaus, H. Electron and Ambipolar Transport in Organic Field-Effect Transistors. *Chem. Rev.* **2007**, 107 (4), 1296–1323.
- (19) Narita, A.; Wang, X. Y.; Feng, X.; Müllen, K. New Advances in Nanographene Chemistry. *Chem. Soc. Rev.* **2015**, 44 (18), 6616–6643.
- (20) Liu, Z.; Fu, S.; Liu, X.; Narita, A.; Samorì, P.; Bonn, M.; Wang, H. I. Small Size, Big Impact: Recent Progress in Bottom-Up Synthesized Nanographenes for Optoelectronic and Energy Applications. *Adv. Sci.* **2022**, 9 (19), 1–18.
- (21) Matsuoka, W.; Ito, H.; Sarlah, D.; Itami, K. Diversity-Oriented Synthesis of Nanographenes Enabled by Dearomative Annulative π -Extension. *Nat. Commun.* **2021**, 12 (1), 1–9.
- (22) Portella, G.; Poater, J.; Solà, M. Assessment of Clar's Aromatic π -Sextet Rule by Means of PDI, NICS and HOMA Indicators of Local Aromaticity. *J. Phys. Org. Chem.* **2005**, 18 (8), 785–791.
- (23) Clar, E. *The Aromatic Sextet*; J. Wiley: London, 1972.
- (24) Solà, M. Forty Years of Clar's Aromatic π -Sextet Rule. *Front. Chem.* **2013**, 1 (October), 4–11.
- (25) Balaban, A. T.; Klein, D. J. Claromatic Carbon Nanostructures. *J. Phys. Chem. C* **2009**, 113 (44), 19123–19133.
- (26) Wiberg, K. B. Properties of Some Condensed Aromatic Systems. *J. Org. Chem.* **1997**, 62 (17), 5720–5727.
- (27) Ruiz-Morales, Y. The Agreement between Clar Structures and Nucleus-Independent Chemical Shift Values in Pericondensed Benzenoid Polycyclic Aromatic Hydrocarbons: An Application of the Y-Rule. *J. Phys. Chem. A* **2004**, 108 (49), 10873–10896.
- (28) Portella, G.; Poater, J.; Bofill, J. M.; Alemany, P.; Solà, M. Local Aromaticity of [n]Acenes, [n]Phenacenes, and [n]Helicenes (n = 1-9). *J. Org. Chem.* **2005**, 70 (7), 2509–2521.

- (29) Thorley, K. J.; Anthony, J. E. The Electronic Nature and Reactivity of the Larger Acenes. *Isr. J. Chem.* **2014**, *54* (5–6), 642–649.
- (30) Zhang, J.; Smith, Z. C.; Thomas, S. W. Electronic Effects of Ring Fusion and Alkyne Substitution on Acene Properties and Reactivity. *J. Org. Chem.* **2014**, *79* (21), 10081–10093.
- (31) V, S. U. Correlating Carrier Type with Frontier Molecular Orbital Functionalized Acene Derivatives. **2009**, No. 16, 5264–5273.
- (32) Anthony, J. E. The Larger Acenes: Versatile Organic Semiconductors. *Angew. Chemie - Int. Ed.* **2008**, *47* (3), 452–483.
- (33) Li, J.; Chen, S.; Wang, Z.; Zhang, Q. Pyrene-Fused Acenes and Azaacenes: Synthesis and Applications. *Chem. Rec.* **2016**, No. Scheme 1, 1518–1530.
- (34) Zhang, L.; Cao, Y.; Colella, N. S.; Liang, Y.; Brédas, J. L.; Houk, K. N.; Briseno, A. L. Unconventional, Chemically Stable, and Soluble Two-Dimensional Angular Polycyclic Aromatic Hydrocarbons: From Molecular Design to Device Applications. *Acc. Chem. Res.* **2015**, *48* (3), 500–509.
- (35) Xu, Q.; Wang, C.; Chen, X.; Wang, Y.; Shen, Z.; Jiang, H. Corannulene-Based Acenes. *Org. Chem. Front.* **2022**, *9* (18), 4981–4989.
- (36) Yu, P.; Zhen, Y.; Dong, H.; Hu, W. Crystal Engineering of Organic Optoelectronic Materials. *Chem* **2019**, *5* (11), 2814–2853.
- (37) Liu, S.; Wu, H.; Zhang, X.; Hu, W. Research Progress of Rubrene as an Excellent Multifunctional Organic Semiconductor. *Front. Phys.* **2021**, *16* (1).
- (38) Teixeira da Rocha, C.; Haase, K.; Zheng, Y.; Löffler, M.; Hamsch, M.; Mannsfeld, S. C. B. Solution Coating of Small Molecule/Polymer Blends Enabling Ultralow Voltage and High-Mobility Organic Transistors. *Adv. Electron. Mater.* **2018**, *4* (8), 1–9.
- (39) Sutton, C.; Risko, C.; Brédas, J. L. Noncovalent Intermolecular Interactions in Organic Electronic Materials: Implications for the Molecular Packing vs Electronic Properties of Acenes. *Chem. Mater.* **2016**, *28* (1), 3–16.
- (40) Anthony, J. E.; Brooks, J. S.; Eaton, D. L.; Parkin, S. R. Functionalized Pentacene: Improved Electronic Properties from Control of Solid-State Order [20]. *J. Am. Chem. Soc.* **2001**, *123* (38), 9482–9483.
- (41) Illig, S.; Eggeman, A. S.; Troisi, A.; Jiang, L.; Warwick, C.; Nikolka, M.; Schweicher, G.; Yeates, S. G.; Henri Geerts, Y.; Anthony, J. E.; Sirringhaus, H. Reducing Dynamic Disorder in Small-Molecule Organic Semiconductors by Suppressing Large-Amplitude Thermal Motions. *Nat. Commun.* **2016**, *7*, 1–10.

- (42) Schweicher, G.; D'Avino, G.; Ruggiero, M. T.; Harkin, D. J.; Broch, K.; Venkateshvaran, D.; Liu, G.; Richard, A.; Ruzié, C.; Armstrong, J.; Kennedy, A. R.; Shankland, K.; Takimiya, K.; Geerts, Y. H.; Zeitler, J. A.; Fratini, S.; Sirringhaus, H. Chasing the "Killer" Phonon Mode for the Rational Design of Low-Disorder, High-Mobility Molecular Semiconductors. *Adv. Mater.* **2019**, *31* (43).
- (43) Eggeman, A. S.; Illig, S.; Troisi, A.; Sirringhaus, H.; Midgley, P. A. Measurement of Molecular Motion in Organic Semiconductors by Thermal Diffuse Electron Scattering. *Nat. Mater.* **2013**, *12* (11), 1045–1049.
- (44) Fratini, S.; Mayou, D.; Ciuchi, S. The Transient Localization Scenario for Charge Transport in Crystalline Organic Materials. *Adv. Funct. Mater.* **2016**, *26* (14), 2292–2315.
- (45) Troisi, A. Dynamic Disorder in Molecular Semiconductors : 2011, pp 1–10.
- (46) Hall, R. N. SILICON PHOTOVOLTAIC CELLS. **1981**, *24*, 595–616.
- (47) Sun, Z.; Chen, X.; He, Y.; Li, J.; Wang, J.; Yan, H.; Zhang, Y. Toward Efficiency Limits of Crystalline Silicon Solar Cells: Recent Progress in High-Efficiency Silicon Heterojunction Solar Cells. *Adv. Energy Mater.* **2022**, *12* (23), 1–17.
- (48) Rao, A.; Friend, R. H. Harnessing Singlet Exciton Fission To. **2017**.
- (49) Casillas, R.; Papadopoulos, I.; Ullrich, T.; Thiel, D.; Kunzmann, A.; Guldi, D. M. Molecular Insights and Concepts to Engineer Singlet Fission Energy Conversion Devices. *Energy Environ. Sci.* **2020**, *13* (9), 2741–2804.
- (50) Baldacchino, A. J.; Collins, M. I.; Nielsen, M. P.; Schmidt, T. W.; McCamey, D. R.; Tayebjee, M. J. Y. Singlet Fission Photovoltaics: Progress and Promising Pathways. *Chem. Phys. Rev.* **2022**, *3* (2), 021304.
- (51) Lee, J.; Jadhav, P.; Reuswig, P. D.; Yost, S. R.; Thompson, N. J.; Congreve, D. N.; Hontz, E.; Van Voorhis, T.; Baldo, M. A. Singlet Exciton Fission Photovoltaics. *Acc. Chem. Res.* **2013**, *46* (6), 1300–1311.
- (52) Fataftah, M. S.; Freedman, D. E. Progress towards Creating Optically Addressable Molecular Qubits. *Chem. Commun.* **2018**, *54* (98), 13773–13781.
- (53) Smyser, K. E.; Eaves, J. D. Singlet Fission for Quantum Information and Quantum Computing: The Parallel JDE Model. *Sci. Rep.* **2020**, *10* (1), 1–10.
- (54) Jacobberger, R. M.; Qiu, Y.; Williams, M. L.; Krzyaniak, M. D.; Wasielewski, M. R. Using Molecular Design to Enhance the Coherence Time of Quintet Multiexcitons Generated by Singlet Fission in Single Crystals. *J. Am. Chem. Soc.* **2022**, *144* (5), 2276–2283.

- (55) Nagashima, H.; Kawaoka, S.; Akimoto, S.; Tachikawa, T.; Matsui, Y.; Ikeda, H.; Kobori, Y. Singlet-Fission-Born Quintet State: Sublevel Selections and Trapping by Multiexciton Thermodynamics. *J. Phys. Chem. Lett.* **2018**, *9* (19), 5855–5861.
- (56) Tayebjee, M. J. Y.; Sanders, S. N.; Kumarasamy, E.; Campos, L. M.; Sfeir, M. Y.; McCamey, D. R. Quintet Multiexciton Dynamics in Singlet Fission. *Nat. Phys.* **2017**, *13* (2), 182–188.
- (57) Matsui, Y.; Kawaoka, S.; Nagashima, H.; Nakagawa, T.; Okamura, N.; Ogaki, T.; Ohta, E.; Akimoto, S.; Sato-Tomita, A.; Yagi, S.; Kobori, Y.; Ikeda, H. Exergonic Intramolecular Singlet Fission of an Adamantane-Linked Tetracene Dyad via Twin Quintet Multiexcitons. *J. Phys. Chem. C* **2019**, *123* (31), 18813–18823.
- (58) Smith, M. B.; Michl, J. Recent Advances in Singlet Fission. *Annu. Rev. Phys. Chem.* **2013**, *64*, 361–386.
- (59) Walker, B. J.; Musser, A. J.; Beljonne, D.; Friend, R. H. Singlet Exciton Fission in Solution. *Nat. Chem.* **2013**, *5* (12), 1019–1024.
- (60) Pensack, R. D.; Grieco, C.; Purdum, G. E.; Mazza, S. M.; Tilley, A. J.; Ostroumov, E. E.; Seferos, D. S.; Loo, Y. L.; Asbury, J. B.; Anthony, J. E.; Scholes, G. D. Solution-Processable, Crystalline Material for Quantitative Singlet Fission. *Mater. Horizons* **2017**, *4* (5), 915–923.
- (61) Stern, H. L.; Cheminal, A.; Yost, S. R.; Broch, K.; Bayliss, S. L.; Chen, K.; Tabachnyk, M.; Thorley, K.; Greenham, N.; Hodgkiss, J. M.; Anthony, J.; Head-Gordon, M.; Musser, A. J.; Rao, A.; Friend, R. H. Vibronically Coherent Ultrafast Triplet-Pair Formation and Subsequent Thermally Activated Dissociation Control Efficient Endothermic Singlet Fission. *Nat. Chem.* **2017**, *9* (12), 1205–1212.
- (62) Stern, H. L.; Musser, A. J.; Gelinias, S.; Parkinson, P.; Herz, L. M.; Bruzek, M. J.; Anthony, J.; Friend, R. H.; Walker, B. J. Identification of a Triplet Pair Intermediate in Singlet Exciton Fission in Solution. *Proc. Natl. Acad. Sci. U. S. A.* **2015**, *112* (25), 7656–7661.
- (63) Davis, N. J. L. K.; Allardice, J. R.; Xiao, J.; Petty, A. J.; Greenham, N. C.; Anthony, J. E.; Rao, A. Singlet Fission and Triplet Transfer to PbS Quantum Dots in TIPS-Tetracene Carboxylic Acid Ligands. *J. Phys. Chem. Lett.* **2018**, *9* (6), 1454–1460.
- (64) Manna, B.; Nandi, A.; Ghosh, R. Ultrafast Singlet Exciton Fission Dynamics in 9,10-Bis(Phenylethynyl)Anthracene Nanoaggregates and Thin Films. *J. Phys. Chem. C* **2018**, *122* (36), 21047–21055.
- (65) Bae, Y. J.; Kang, G.; Malliakas, C. D.; Nelson, J. N.; Zhou, J.; Young, R. M.; Wu, Y. L.; Van Duyne, R. P.; Schatz, G. C.; Wasielewski, M. R. Singlet Fission in 9,10-Bis(Phenylethynyl)Anthracene Thin Films. *J. Am. Chem. Soc.* **2018**, *140* (45), 15140–15144.

- (66) Bae, Y. J.; Christensen, J. A.; Kang, G.; Zhou, J.; Young, R. M.; Wu, Y. L.; Van Duyne, R. P.; Schatz, G. C.; Wasielewski, M. R. Substituent Effects on Energetics and Crystal Morphology Modulate Singlet Fission in 9,10-Bis(Phenylethynyl)Anthracenes. *J. Chem. Phys.* **2019**, *151* (4).
- (67) Hetzer, C.; Guldi, D. M.; Tykwinski, R. R. Pentacene Dimers as a Critical Tool for the Investigation of Intramolecular Singlet Fission. *Chem. - A Eur. J.* **2018**, *24* (33), 8245–8257.
- (68) Korovina, N. V.; Pompetti, N. F.; Johnson, J. C. Lessons from Intramolecular Singlet Fission with Covalently Bound Chromophores. *J. Chem. Phys.* **2020**, *152* (4).
- (69) Basel, B. S.; Papadopoulos, I.; Thiel, D.; Casillas, R.; Zirzmeier, J.; Clark, T.; Guldi, D. M.; Tykwinski, R. R. Pentacenes: A Molecular Ruler for Singlet Fission. *Trends Chem.* **2019**, *1* (1), 11–21.
- (70) Gilligan, A. T.; Miller, E. G.; Sammakia, T.; Damrauer, N. H. Using Structurally Well-Defined Norbornyl-Bridged Acene Dimers to Map a Mechanistic Landscape for Correlated Triplet Formation in Singlet Fission. *J. Am. Chem. Soc.* **2019**, *141* (14), 5961–5971.
- (71) Kumarasamy, E.; Sanders, S. N.; Tayebjee, M. J. Y.; Asadpoordarvish, A.; Hele, T. J. H.; Fuemmeler, E. G.; Pun, A. B.; Yablon, L. M.; Low, J. Z.; Paley, D. W.; Dean, J. C.; Choi, B.; Scholes, G. D.; Steigerwald, M. L.; Ananth, N.; McCamey, D. R.; Sfeir, M. Y.; Campos, L. M. Tuning Singlet Fission in π -Bridge- π Chromophores. *J. Am. Chem. Soc.* **2017**, *139* (36), 12488–12494.
- (72) Yamakado, T.; Takahashi, S.; Watanabe, K.; Matsumoto, Y.; Osuka, A.; Saito, S. Conformational Planarization versus Singlet Fission: Distinct Excited-State Dynamics of Cyclooctatetraene-Fused Acene Dimers. *Angew. Chemie* **2018**, *130* (19), 5536–5541.
- (73) Smyser, K. E.; Eaves, J. D. Singlet Fission for Quantum Information and Quantum Computing: The Parallel JDE Model. *Sci. Rep.* **2020**, *10* (1).
- (74) Dill, R. D.; Smyser, K. E.; Rugg, B. K.; Damrauer, N. H.; Eaves, J. D. Entangled Spin-Polarized Excitons from Singlet Fission in a Rigid Dimer. *Nat. Commun.* **2023**, *14* (1), 1–7.
- (75) Chow, T. J.; WATANABE, M.; CHEN, K.; CHANG, Y. Acenes Generated from Precursors and Their Semiconducting Properties. *Acc. Chem. Res.* **2013**, *46* (7).
- (76) Szczepanik, D. W.; Solà, M.; Krygowski, T. M.; Szatyłowicz, H.; Andrzejak, M.; Pawełek, B.; Dominikowska, J.; Kukułka, M.; Dyduch, K. Aromaticity of Acenes: The Model of Migrating π -Circuits. *Phys. Chem. Chem. Phys.* **2018**, *20* (19), 13430–13436.
- (77) Von Ragué Schleyer, P.; Manoharan, M.; Jiao, H.; Stahl, F. The Acenes:

Is There a Relationship between Aromatic Stabilization and Reactivity?
Org. Lett. **2001**, 3 (23), 3643–3646.

- (78) Bendikov, M.; Wudl, F.; Perepichka, D. F. *Tetrathiafulvalenes, Oligoacenes, and Their Buckminsterfullerene Derivatives: The Brick and Mortar of Organic Electronics*; 2004; Vol. 104.
- (79) Zade, S. S.; Bendikov, M. Reactivity of Acenes: Mechanisms and Dependence on Acene Length. *J. Phys. Org. Chem.* **2012**, 25 (6), 452–461.
- (80) Chien, S.; Cheng, M.; Lau, K.; Li, W. Theoretical Study of the Diels-Alder Reactions between Singlet ($1\Delta_g$) Oxygen and Acenes. **2005**, 7509–7518.
- (81) Zade, S. S.; Zamoshchik, N.; Reddy, A. R.; Fridman-Marueli, G.; Sheberla, D.; Bendikov, M. Products and Mechanism of Acene Dimerization. A Computational Study. *J. Am. Chem. Soc.* **2011**, 133 (28), 10803–10816.
- (82) Maliakal, A.; Raghavachari, K.; Katz, H.; Chandross, E.; Siegrist, T. Photochemical Stability of Pentacene and a Substituted Pentacene in Solution and in Thin Films. *Chem. Mater.* **2004**, 16 (24), 4980–4986.
- (83) Northrop, B. H.; Houk, K. N.; Maliakal, A. Photostability of Pentacene and 6,13-Disubstituted Pentacene Derivatives: A Theoretical and Experimental Mechanistic Study. *Photochem. Photobiol. Sci.* **2008**, 7 (12), 1463–1468.
- (84) Fudickar, W.; Linker, T. Why Triple Bonds Protect Acenes from Oxidation and Decomposition. *J. Am. Chem. Soc.* **2012**, 134 (36), 15071–15082.
- (85) Zhang, L.; Fonari, A.; Liu, Y.; Hoyt, A. M.; Lee, H.; Granger, D.; Parkin, S.; Russell, T. P.; Anthony, J. E.; Bre, J.; Coropceanu, V. Bistetracene: An Air-Stable, High-Mobility Organic Semiconductor with Extended Conjugation. *J. Am. Chem. Soc.* **2014**, 136, 9248–9251.
- (86) Jusselin-Oba, T.; Mamada, M.; Marrot, J.; Maignan, A.; Adachi, C.; Yassar, A.; Frigoli, M. Excellent Semiconductors Based on Tetracenotetracene and Pentacenopentacene: From Stable Closed-Shell to Singlet Open-Shell. *J. Am. Chem. Soc.* **2019**, 141 (23), 9373–9381.
- (87) Jusselin-Oba, T.; Mamada, M.; Wright, K.; Marrot, J.; Adachi, C.; Yassar, A.; Frigoli, M. Synthesis, Aromaticity, and Application of Peri-Pentacenopentacene: Localized Representation of Benzenoid Aromatic Compounds. *Angew. Chemie - Int. Ed.* **2022**, 61 (1).
- (88) Thomas, S.; Ly, J.; Zhang, L.; Briseno, A. L.; Bredas, J. L. Improving the Stability of Organic Semiconductors: Distortion Energy versus Aromaticity in Substituted Bistetracene. *Chem. Mater.* **2016**, 28 (23), 8504–8512.
- (89) Butson, M. J.; Yu, P. K. N.; Cheung, T.; Metcalfe, P. Radiochromic Film for Medical Radiation Dosimetry. *Mater. Sci. Eng. R Reports* **2003**, 41 (3–5), 61–120.

- (90) Niroomand-Rad, A.; Blackwell, C. R.; Coursey, B. M.; Gall, K. P.; Galvin, J. M.; McLaughlin, W. L.; Meigooni, A. S.; Nath, R.; Rodgers, J. E.; Soares, C. G. Radiochromic Film Dosimetry: Recommendations of AAPM Radiation Therapy Committee Task Group 55. *Med. Phys.* **1998**, *25* (11), 2093–2115.
- (91) Lan, X.; Muthyala, R. The Chemistry of Leuco Triarylmethanes. In *Chemistry and Applications of Leuco Dyes*; Springer: Boston, MA, 2002; pp 125–154.
- (92) McLaughlin, W. L.; Miller, A.; Fidan, S.; Pejtersen, K.; Batsberg Pedersen, W. Radiochromic Plastic Films for Accurate Measurement of Radiation Absorbed Dose and Dose Distributions. *Radiat. Phys. Chem.* **1977**, *10* (2), 119–127.
- (93) McLaughlin, W. L.; Humphreys, J. C.; Radak, B. B.; Miller, A.; Olejnik, T. A. The Response of Plastic Dosimeters to Gamma Rays and Electrons at High Absorbed Dose Rates. *Radiat. Phys. Chem.* **1979**, *14* (3–6), 535–550.
- (94) W.L. McLaughlin, J.C. Humphreys, H. Levine, A. Miller, B. B. R.; Rativanich, and N. R. THE GAMMA-RAY RESPONSE OF RADIOCHROMIC DYE FILMS AT DIFFERENT ABSORBED DOSE RATES. *Rad/at Phys. Chem* **1981**, *18*, 987–999.
- (95) Alqathami, M.; Adamovics, J.; Benning, R.; Qiao, G.; Geso, M.; Blencowe, A. Evaluation of Ultra-Sensitive Leucomalachite Dye Derivatives for Use in the PRESAGEs Dosimeter. *Radiat. Phys. Chem.* **2013**, *85*, 204–209.
- (96) Juang, T.; Newton, J.; Niebanck, M.; Benning, R.; Adamovics, J.; Oldham, M. Customising PRESAGE® for Diverse Applications. *J. Phys. Conf. Ser.* **2013**, *444* (1).
- (97) Adamovics, J.; Maryanski, M. J. Characterisation of PRESAGE™: A New 3-D Radiochromic Solid Polymer Dosemeter for Ionising Radiation. *Radiat. Prot. Dosimetry* **2006**, *120* (1–4), 107–112.
- (98) Alqathami, M.; Blencowe, A.; Qiao, G.; Butler, D.; Geso, M. Optimization of the Sensitivity and Stability of the PRESAGE™ Dosimeter Using Trihalomethane Radical Initiators. *Radiat. Phys. Chem.* **2012**, *81* (7), 867–873.
- (99) Dumas, M.; Rakowski, J. T. Sensitivity and Variability of Presage Dosimeter Formulations in Sheet Form with Application to SBRT and SRS QA. *Med. Phys.* **2015**, *42* (12), 7138–7143.
- (100) Mateo-Alonso, A. Synthetic Approaches to Pyrene-Fused Twistacenes. *European J. Org. Chem.* **2017**, *2017* (47), 7006–7011.
- (101) Cortizo-Lacalle, D.; Mora-Fuentes, J. P.; Strutyński, K.; Saeki, A.; Melle-Franco, M.; Mateo-Alonso, A. Monodisperse N-Doped Graphene

- Nanoribbons Reaching 7.7 Nanometers in Length. *Angew. Chemie - Int. Ed.* **2018**, *57* (3), 703–708.
- (102) Hernández-Culebras, F.; Melle-Franco, M.; Mateo-Alonso, A. Doubling the Length of the Longest Pyrene-Pyrazinoquinoxaline Molecular Nanoribbons. *Angew. Chemie - Int. Ed.* **2022**, *61* (27).
- (103) Ai, Q.; Jarolimek, K.; Mazza, S.; Anthony, J. E.; Risko, C. Delimited Polyacenes: Edge Topology as a Tool to Modulate Carbon Nanoribbon Structure, Conjugation, and Mobility. *Chem. Mater.* **2018**, *30* (3), 947–957.
- (104) Ai, Q.; Smith, T.; Liyanage, A. D. T.; Mazza, S. M.; Parkin, S. R.; Anthony, J. E.; Risko, C. Nanoribbons or Weakly Connected Acenes? The Influence of Pyrene Insertion on Linearly Extended Ring Systems. *J. Mater. Chem. C* **2021**, *9* (47), 16929–16934.
- (105) Walsh, J. C.; Williams, K. L. M.; Lungerich, D.; Bodwell, G. J. Synthesis of Pyrene-4,5-Dione on a 15 g Scale. *European J. Org. Chem.* **2016**, *2016* (36), 5933–5936.
- (106) Cava, M. P.; Shirley, R. L. Condensed Cyclobutane Aromatic Compounds. X. Naphtho[b]Cyclobutene. *J. Am. Chem. Soc.* **1960**, *82* (3), 654–656.
- (107) Chen, J.; Zhang, Y.; Yang, L.; Zhang, X.; Liu, J.; Li, L.; Zhang, H. A Practical Palladium Catalyzed Dehalogenation of Aryl Halides and α -Haloketones. *Tetrahedron* **2007**, *63* (20), 4266–4270.
- (108) Klevens, H. B.; Platt, J. R. Spectral Resemblances of Cata-Condensed Hydrocarbons. *J. Chem. Phys.* **1949**, *17* (5), 470–481.
- (109) Tanaka, J. The Electronic Spectra of Pyrene, Chrysene, Azulene, Coronene and Tetracene Crystals. *Bull. Chem. Soc. Jpn.* **1965**, *38* (1), 86–102.
- (110) Odom, S. A.; Parkin, S. R.; Anthony, J. E. Tetracene Derivatives as Potential Red Emitters for Organic LEDs. *Org. Lett.* **2003**, *5* (23), 4245–4248.
- (111) Pun, J. K. H.; Gallaher, J. K.; Frazer, L.; Prasad, S. K. K.; Dover, C. B.; MacQueen, R. W.; Schmidt, T. W. TIPS-Anthracene: A Singlet Fission or Triplet Fusion Material? *J. Photonics Energy* **2018**, *8* (02), 1.
- (112) Nishimura, N.; Gray, V.; Allardice, J. R.; Zhang, Z.; Pershin, A.; Beljonne, D.; Rao, A. Photon Upconversion from Near-Infrared to Blue Light with TIPS-Anthracene as an Efficient Triplet-Triplet Annihilator. *ACS Mater. Lett.* **2019**, *1* (6), 660–664.
- (113) Olesund, A.; Gray, V.; Mårtensson, J.; Albinsson, B. Diphenylanthracene Dimers for Triplet-Triplet Annihilation Photon Upconversion: Mechanistic Insights for Intramolecular Pathways and the Importance of Molecular Geometry. *J. Am. Chem. Soc.* **2021**, *143* (15), 5745–5754.

- (114) Zeng, L.; Huang, L.; Han, J.; Han, G. Enhancing Triplet-Triplet Annihilation Upconversion: From Molecular Design to Present Applications. *Acc. Chem. Res.* **2022**, *55* (18), 2604–2615.
- (115) Levitus, M.; Garcia-Garibay, M. A. Polarized Electronic Spectroscopy and Photophysical Properties of 9,10-Bis(Phenylethynyl)Anthracene. *J. Phys. Chem. A* **2000**, *104* (38), 8632–8637.
- (116) Lin, L.-C.; Smith, T.; Ai, Q.; Rugg, B. K.; Risko, C.; Anthony, J. E.; Johnson, Justin C. Damrauer, N. H. Multiexciton Quintet State Populations in a Rigid Pyrene - Bridged Parallel Tetracene Dimer. *Under Review*.
- (117) Sakaguchi, T.; Shiotsuki, M.; Sanda, F.; Freeman, B. D.; Masuda, T. Synthesis and Properties of F-Containing Poly (Diphenylacetylene) Membranes. **2005**, 8327–8332.
- (118) Wang, Z.; Li, R.; Chen, Y.; Tan, Y. Z.; Tu, Z.; Gao, X. J.; Dong, H.; Yi, Y.; Zhang, Y.; Hu, W.; Müllen, K.; Chen, L. A Novel Angularly Fused Bistetracene: Facile Synthesis, Crystal Packing and Single-Crystal Field Effect Transistors. *J. Mater. Chem. C* **2017**, *5* (6), 1308–1312.
- (119) Harish K. Patney. Synthesis of 2,3-Norbornadienonaphthacene. **1988**, No. 53, 6106–6109.
- (120) Palilis, L. C.; Lane, P. A.; Kushto, G. P.; Purushothaman, B.; Anthony, J. E.; Kafafi, Z. H. Organic Photovoltaic Cells with High Open Circuit Voltages Based on Pentacene Derivatives. *Org. Electron.* **2008**, *9* (5), 747–752.
- (121) Liberko, C. A.; Miller, L. L.; Katz, T. J.; Liu, L. The Electronic Structure of Helicene-Bisquinone Anion Radicals. *J. Am. Chem. Soc.* **1993**, *115* (6), 2478–2482.
- (122) Stahl, D.; Maquin, F. Charge-Stripping Mass Spectrometry of Molecular Ions from Polyacenes and Molecular Orbital Theory. *Chem. Phys. Lett.* **1984**, *108* (6), 613–617.
- (123) Abu-Sen, L.; Morrison, J. J.; Horn, A. B.; Yeates, S. G. Concentration- and Solvent-Dependent Photochemical Instability of 6,13-Bis(Triisopropylsilylethynyl)Pentacene. *Adv. Opt. Mater.* **2014**, *2* (7), 636–640.
- (124) Harrelson, T. F.; Dantanarayana, V.; Xie, X.; Koshnick, C.; Nai, D.; Fair, R.; Nuñez, S. A.; Thomas, A. K.; Murrey, T. L.; Hickner, M. A.; Grey, J. K.; Anthony, J. E.; Gomez, E. D.; Troisi, A.; Faller, R.; Moulé, A. J. Direct Probe of the Nuclear Modes Limiting Charge Mobility in Molecular Semiconductors. *Mater. Horizons* **2019**, *6* (1), 182–191.
- (125) Clar, E.; Lovat, M. M.; Simpson, W. New Benzenogenic Diene Syntheses. *Tetrahedron* **1974**, *30* (18), 3293–3298.
- (126) Clar, E.; Wallenstein, H.; Avenarius, R. Zur Kenntnis Mehrkerniger

Aromatischer Kohlenwasserstoffe Und Ihrer Abkommlinge, 111. Mitteil. : Anthraceno-Anthracene Und Ihre Chinone. **1929**, No. 62, 950–955.

- (127) Jančařík, A.; Mildner, D.; Nagata, Y.; Banasiewicz, M.; Olas, J.; Kozankiewicz, B.; Holec, J.; Gourdon, A. Synthesis and Absorption Properties of Long Acenoacenes. *Chem. - A Eur. J.* **2021**, 27 (48), 12388–12394.
- (128) Ahrens, L.; Hahn, S.; Rominger, F.; Freudenberg, J.; Bunz, U. H. F. N-Acenoacenes. *Chem. - A Eur. J.* **2019**, 25 (64), 14522–14526.
- (129) Peña, D.; Cobas, A.; Pérez, D.; Guitián, E. An Efficient Procedure for the Synthesis of Ortho-Trialkylsilylaryl Triflates: Easy Access to Precursors of Functionalized Arynes. *Synthesis (Stuttg)*. **2002**, No. 10, 1454–1458.
- (130) Burcham, A. *TATTOO: LEUCO DYE COMBAT DOSIMETER FOR CASUALTY ANALYSIS*; 2020.
- (131) Arnett, E. M.; Flowers, R. A.; Ludwig, R. T.; Meekhof, A. E.; Walek, S. A. Triarylmethanes and 9-Arylxanthenes as Prototypes Amphihydric Compounds for Relating the Stabilities of Cations, Anions and Radicals by C-H Bond Cleavage and Electron Transfer. *J. Phys. Org. Chem.* **1997**, 10 (7), 499–513.
- (132) Egger, K. W.; Cocks, A. T. Homopolar and Heteropolar Bond Dissociation Energies and Heats of Formation of Radicals and Ions in the Gas Phase II. The Relationship between Structure and Bond Dissociation in Organic Molecules. *Helv. Chim. Acta* **1973**, 56 (5), 1537–1552.

Vita
Tanner Lanier Smith
Born in Decatur, IL

Education:

B.S. in Chemistry, Southern Illinois University, Carbondale, IL, 2018

Honors and Awards:

Research-Enriched Academic Challenge Award, Southern Illinois University,
2017

Publications:

Liang-Chun Lin, Tanner Smith, Qianxiang Ai, Brandon K. Rugg, Chad Risko, John E. Anthony, Niels H. Damrauer, Justin C. Johnson, Multiexciton Quintet State Populations in a Rigid Pyrene -Bridged Parallel Tetracene Dimer. *Under Review*.

Ai, Q.; Smith, T.; Liyanage, A. D. T.; Mazza, S. M.; Parkin, S. R.; Anthony, J. E.; Risko, C. Nanoribbons or Weakly Connected Acenes? The Influence of Pyrene Insertion on Linearly Extended Ring Systems. *J. Mater. Chem. C*, **2021**, *9* (47), 16929–16934.

Van Wyk, A., Smith T., Park, J., Deria, P., Charge-Transfer within Zr-Based Metal–Organic Framework: The Role of Polar Node. *J. Am. Chem. Soc.* 2018, *140*, *8*, 2756–2760.

Deria, P., Yu, J., Smith, T., Balaraman, R., Ground-State versus Excited-State Interchromophoric Interaction: Topology Dependent Excimer Contribution in Metal–Organic Framework Photophysics. *J. Am. Chem. Soc.*, 2017, *139*, *16*, 5973–5983.